4.10 Assessment of Semiconductors by Scanning Electron Microscopy Techniques

G Salviati and L Lazzarini, CNR-IMEM Institute, Parma, Italy

T Sekiguch and B Chen, National Institute for Materials Science (NIMS), Ibaraki, Japan

4.10.1	**Introduction**	309
4.10.2	**Scenario**	310
4.10.2.1	Magnetic Contrast Imaging	310
4.10.2.1.1	Type-1 magnetic contrast	310
4.10.2.1.2	Type-2 magnetic contrast	310
4.10.2.2	Scanning Electron Acoustic Microscopy	310
4.10.2.3	Doping-Related SEM Image Contrast	311
4.10.2.4	Near-Field CL	312
4.10.2.5	Voltage Contrast	312
4.10.2.6	Scanning Deep-Level Transient Spectroscopy	313
4.10.3	**Short Introduction to CL Spectroscopy and Imaging**	313
4.10.3.1	The CL Experimental Setup in the SEM	315
4.10.3.2	Lateral, In-Depth, and Analytical Resolution	317
4.10.3.3	Role of Excitation Conditions	317
4.10.3.3.1	CL Emission Efficiency, Energy Peak Position, and Line Shape Broadening	318
4.10.4	**Short Introduction to EBIC Theory**	319
4.10.4.1	Principle	319
4.10.4.2	Experimental Setup	320
4.10.4.3	Operating Condition	320
4.10.5	**Reviewing CL Emblematic Examples from the Literature**	321
4.10.5.1	CL Spectroscopy and Imaging of Unpredicted Cubic Phase in ZnO Tetrapods	322
4.10.5.2	Impuritiy Contamination and Nonhomogeneous Elemental Distribution in Low-Dimensional Structures	324
4.10.5.3	CL of Rare-Earth-Doped Oxynitrides for Field Emission Displays	329
4.10.5.4	Power and Depth-Resolved CL	331
4.10.5.4.1	Power-dependent CL screening of internal fields in low indium content InGaN/GaN multi-quantum wells	332
4.10.5.4.2	Depth-resolved CL study of interface chemical interactions at metal–ZnO interfaces	334
4.10.5.5	Time-Resolved CL	336
4.10.6	**EBIC Characterization of Extended Defects**	339
4.10.6.1	Extended Defects in Si	339
4.10.6.2	Extended Defects in SiC	342
4.10.6.3	Extended Defects in Other Semicondutors	345
4.10.6.4	EBIC Characterization of Devices	348
4.10.6.4.1	p–n junctions	348
4.10.6.4.2	Diffusion length	350
4.10.6.4.3	Leakage detection in MOSFETs	350
4.10.7	**Future Advancement of CL and EBIC**	351
4.10.8	**Conclusions**	353
References		354

Glossary

AFM Atomic force microscopy.
BPD Basal plane dislocation.
BSE Back scattered electron.
BSF Basal stacking fault.
CBM Conduction band minimum.
CL Cathodoluminescence.
DAP Donor-to-acceptor pair.
DLTS Deep-level transient spectroscopy.
DRCL Depth-resolved cathodoluminescence spectroscopy.
EBIC Electron beam-induced current.
EBSD Electron backscattering diffraction.
ELO Epitaxial lateral overgrowth.
ELOG Epitaxial lateral overgrown.
FED Field emission display.
FWHM Full width at half maximum.
GB Grain boundary.
LA Large-angle.
LED Light-emitting diode.
MD Misfit dislocations.
MOCVD Metal-organic chemical vapor deposition.
MOSFET Metal-oxide semiconductor field-effect transistor.
NBE Near band edge.
PDL Partial dislocation loop.
QWR Quantum wire.
SDLTS Scanning deep-level transient spectroscopy.
SEAM Scanning electron acoustic microscopy.
SEM Scanning electron microscope.
SNCLM Scanning near-field cathodoluminescence microscopy.
SNOM Scanning near-field optical microscopy.
SPM Scanning probe microscope.
STEM Scanning transmission electron microscopy.
TD Threading dislocation.
TEM Transmission electron microscope.
TRLS Time-resolved luminescence spectroscopy.

4.10.1 Introduction

Since the early 1980s, the scanning electron microscope (SEM) is one of the most widespread instruments both for basic and industrial research. The reasons for such a popularity have to be looked into the great flexibility the SEM offers in term of the characterization techniques that can be attached to it for carrying on peculiar investigations at the micro- and nanoscale on almost any kind of inorganic and organic compounds. In particular, the observation of organic materials has been made possible after the development of field emission gun environmental SEM (ESEM) working at low acceleration voltages in a chamber kept at lower vacuum than that of the electro-optical column. Positively charged ions are then generated by the interactions between the electron beam and a gas so quasi-neutralizing the negative charge on the specimen surface. The gas pressure in the chamber can be controlled and the type of gas used can be varied according to the user's needs.

As for the qualitative and quantitative characterization of semiconductor materials and devices from the micro- to the nanoscale, SEM-based techniques have been extensively and successfully used in the last decades. The main reasons are due to the fact that these techniques allow the concurrent investigation of different physical and chemical properties of the specimens studied. Finally, the advent of SEMs with field emission guns (FE-SEM) has further speeded up the use of the aforementioned techniques for nanoscale research and nanotechnology. In addition to energy and/or wavelength dispersive X-ray microanalysis for chemical composition assessment, the main experimental systems attached to an SEM will be briefly reviewed in the following.

The principle of the SEM is very well known and has been described in a variety of excellent books (see, e.g., Reimer, 1998), so here only a few words will be spent to summarize the SEM fundamentals. As for a short history of the SEM discovery and development, the reader is referred to, for example, Breton (2009).

The SEM uses a focused beam of electrons carrying significant amounts of kinetic energy, to generate a variety of signals at the surface of solid specimens. The signals that derive from electron–sample interactions due to the deceleration inside the solid sample reveal peculiar information about the specimen.

These signals include secondary electrons (SEs), backscattered electrons (BSEs), diffracted backscattered electrons (electron backscattering diffraction, EBSD) that are used to determine crystal structures and orientations of crystals, photons (as characteristic X-rays that are used for elemental analysis and continuum X-rays), infrared, visible, or ultraviolet light cathodoluminescence (CL), electron beam-induced current (EBIC), acoustic waves, heat, etc. SEs and BSEs are commonly used for imaging samples: SEs are most valuable for showing morphology and topography on samples and BSEs are most valuable for illustrating contrasts in composition in multi-phase samples (i.e., for rapid phase discrimination). SEM analyses, under appropriate experimental conditions, are considered nondestructive so it is possible to analyze the same materials repeatedly also with other techniques.

In this chapter we limit ourselves to the application of CL and EBIC techniques to the study of optical and electrical properties of semiconductor heterostructures and devices. The basic principles of the techniques as well as their experimental setup will be briefly described in Sections 4.10.3 and 4.10.4 and some emblematic examples will presented and discussed in Sections 4.10.5 and 4.10.6.

4.10.2 Scenario

Various techniques taking advantage of the SEM versatility have been developed in the last three decades so, before focusing on CL and EBIC, it is worth noting to briefly describe the most important ones in characterizing semiconductor materials.

4.10.2.1 Magnetic Contrast Imaging

A detailed knowledge and complete understanding of the magnetic microstructure is of great interest from both fundamental and technological points of view. On the fundamental side, it is important to get information on the saturation magnetization (i.e., the maximum induced magnetic moment that can be obtained in a magnetic field beyond that no further increase in magnetization occurs), the exchange constant and the domain wall energy (the difference between the magnetic moments before and after the domain wall was created) as well as of the macroscopic properties such as the magnetization curves and hysteresis loops, the various susceptibilities or magnetoresistance, permeabilities, losses, etc. From the technological point of view, the observation of the domain structure plays a relevant role in the development of high-density magnetic and magneto-optic recording media, modern recording heads, permanent magnets, and magnetic sensors.

There are two types of magnetic contrast.

4.10.2.1.1 Type-1 magnetic contrast

In brief, if the trajectories of SEs are considered, which have an exit angular distribution and an energy spectrum of a few electronvolts, they can be easily deflected by external strain fields of ferromagnetic domains in materials with uniaxial anisotropy. The extent of the strain field is of the order of the domain width. As a consequence, the field is highly inhomogeneous and the SEs emitted normal to the sample surface do not feel the same magnetic field as those leaving the surface with an inclined direction to the normal. It is that angular selection that creates the so-called type-1 magnetic contrast.

4.10.2.1.2 Type-2 magnetic contrast

If BSEs are considered, the so-called type-2 magnetic contrast occurs due to the action of the Lorentz force of the spontaneous induction $\underline{B}$ in ferromagnetic domains on the BSE trajectories. So, if the bending radius of the BSE trajectories between scattering events is much smaller than in reality, the backscattering coefficient will be different for opposite directions of $\underline{B}$. This obviously depends on whether the trajectories are bent away from or toward the specimen surface.

For a more exhaustive description of the magnetic contrast in the SEM (see, e.g., Reimer, 1998: ch. 6, Pt 6.3). A nice example of the achievements of the technique for extracting the position of domain walls from BSE images recorded in an SEM as well as the static and dynamic magnetic domain contrast images in $Fe_{79}Si_6B_{14}Cu_1$ metallic glass can be found in a recent paper from Varga *et al.* (2006).

4.10.2.2 Scanning Electron Acoustic Microscopy

Scanning electron acoustic microscopy (SEAM), also referred to as thermal wave microscopy, is a technique that uses a focused and modulated electron beam in an SEM to generate ultrasonic waves

at the front surface of a specimen. A piezoelectric transducer detects these waves at the rear surface and its output is used to form a scanned, magnified image of the specimen. The image contrast comes primarily from spatial variations in thermal and elastic properties of the samples studied. SEAM images subsurface defects and doping information in semiconductors as well as residual stress field distribution in ceramics and domain structures in ferroelectric materials.

After the pioneering work of Cargill (1980) and Brandis and Rosencwaig (1980), the SEAM has been proved to be successfully applied in a variety of material science problems (see, e.g. Urchulutegui and Piqueras, 1991; Li *et al.*, 1996). However, the interpretation of the SEAM contrast in semiconductors is not as simple as in metals (Balk and Kultsher, 1987) where the thermal wave theory fulfills the requirements for the image interpretation (Rosencwaig and Gersho, 1976; Rosencwaig, 1982). A comprehensive review of the limits and possibilities offered by the SEAM in the study of semiconductors, ceramics, and polymers has been done by Balk (1988).

Due to an achievable lateral resolution not better than 1000 nm, the SEAM technique was not that much extensively used in the characterization of semiconductors, for which after the late 1990s, information at the nanoscale was needed. In this respect, when failure analysis and reliability of materials and devices by means of acoustic waves is needed at the nanoscale, near-field detection is necessary, because the achievable resolution in far field is limited by the Abbe criterion. In this case an SEM/scanning probe microscope (SPM) hybrid system can be used with the SPM built inside the chamber of an SEM (Thomas *et al.*, 2007).

Obviously, the same approach can be followed outside an SEM by means of a scanning probe microscope (Balk *et al.*, 2007).

4.10.2.3 Doping-Related SEM Image Contrast

The electrical activation of dopant atoms has traditionally been important in semiconductor science and technology. Usually, the concentration of free carriers does not coincide with the total number of dopant atoms, since not all dopant atoms may reside in substitutional sites within the host crystal lattice. Investigations concerning electrical activation are usually carried out by comparing the total concentration of doping atoms measured by a nonelectrical technique such as secondary-ion mass spectroscopy, and the free-carrier concentration obtained by electrical techniques such as spreading resistance, Hall effect, or capacitance-voltage profiling. However, such techniques present some limitations such as poor depth or lateral resolutions and the need of etching procedures.

Thanks to the introduction of field-emission electron guns coupled with new detectors that made it possible to obtain high-resolution images over a wide range of acceleration voltages in the SEM, a new technique has been developed in the late 1990s aimed to nondestructively map electrically active doping profiles by field-emission SEM. A sensitivity in two dimensions as low as $10^{16}\,\mathrm{cm}^{-3}$ and a spatial resolution limited by the Debye length were achieved.

In this field, pioneering work has been done by Perovic *et al.* (1995) on Si and III–Vs compounds. The contrast mechanism has been explained in terms of electronic effects associated with surface-induced band-bending differences between n- and p-doped layers which accounted for the enhanced or retarded SE emission from a semiconductor surface within p-type versus n-type doped regions, respectively. The effect was purely electronic and not connected to atomic number differences.

Recently, El-Gomati *et al.* (2004) have developed a new model that considers variations in the patch fields above the sample surface, balancing variations in the inner potentials, or surface coatings, and/or surface states as responsible for the contrast between differently doped regions. The results showed that the subsurface electric fields, instead of the patch fields above the surface, are responsible for the SE contrast of doped semiconductors imaged in low-voltage SEMs under standard vacuum conditions.

An alternative method has been proposed by Morandi *et al.* (2006). They have shown that it is possible to use BSEs, or SEs produced by BSEs in an SEM, to obtain two-dimensional information about the doping spatial distribution in Sb-implanted Silicon.

An overview of the existing two-dimensional carrier profiling tools using experimental tools alternative to the SEM, that is, scanning probe microscopy, including several scanning tunneling microscopy modes, scanning capacitance microscopy, Kelvin probe microscopy, scanning spreading

resistance microscopy, and dopant-selective etching, are extensively reviewed by De Wolf *et al.* (2000).

4.10.2.4 Near-Field CL

The basic idea to overcome the diffraction limit in microscopy was discussed by Synge (1928, 1932). To understand Synge's proposal we have to introduce two notions that are not applicable to conventional optics: the far field and the near field. With respect to a light source, the observer stays in the far field when the distance between him and the light source is more than the wavelength λ of the emitted light ($d > \lambda$). The near field, consequently, describes the range within the wavelength of the light ($d < \lambda$).

When the observer stays in the near field, the Abbe's theory on the diffraction limit (Abbe, 1873) also known as Rayleigh criterion is no longer applicable and the resolution is only determined by the size of the light source and its separation from the surface. Therefore, if a thin sample is illuminated by an incoming plane wave through an aperture smaller than the wavelength, a resolution beyond the diffraction limit is possible. No diffraction-limited lens is needed for the image formation at a resolution functionally dependent only on the probe size and the probe-to-sample separation, each of which can be made much smaller than the wavelength of light.

A scanning near-field microscope generally consists of a probe that can induce or detect near-field interactions with the sample. Depending on which property should be analyzed, the near-field interactions can be caused by different fields or waves, such as optic, magnetic, electric, thermal, acoustic, or mechanical. The applications and the papers published are so many that it is impossible to quote them here. So, in the following, we briefly focus only on the application to semiconductors of a modified scanning near-field optical microscopy (SNOM): namely the scanning near-field electron microscopy, with a particular attention to the scanning near-field cathodoluminescence microscopy (SNCLM) (also called near-field cathodoluminescence).

Pioneering work in this field has been done by Cramer *et al.* (1998) and by Troyon *et al.* (1998).

In brief, to get SNCLM investigations at the nanometer scale, a hybrid system made by an SNOM implemented in the chamber of an SEM has been developed. The system allows us to image a sample in a conventional SEM mode, to investigate the local topography, and to simultaneously perform near-field CL imaging.

In practice, the vicinity of the tip-sample contact area is irradiated homogeneously with primary electrons and the resulting luminescence is picked up directly above the recombination centers by the SNOM probe with a probe–sample distance of a few nanometers. The AFM tip is used to diffract the evanescent waves at the surface, while the light collection is done by means of an optical fiber. The CL excitation is performed just below the tip by a conventional SEM focused electron beam. An improvement in spatial resolution of at least one order of magnitude with respect to the classical far-field CL has been proved. This is possible because the SNCLM lateral resolution is not energy-transfer dependent, but it is mainly determined by the tip dimensions.

4.10.2.5 Voltage Contrast

Every semiconductor device has a unique distribution of potential and charge. This unique signature of potential characterizes completely the successful operation or failure of the device. The device design and testing require a quantitative measurement of a field profile with a lateral resolution on a submicron scale. Voltage contrast is a contactless analysis technique performed using an SEM for the study of potentials and potential distributions in devices. It is used to detect open conductor lines, open junctions, or reverse-biased junctions. It operates on the basic principle that the emission of SEs by a sample bombarded with the primary electron beam of an SEM is restricted or enhanced by the presence of local electric fields within the circuit.

Since these SE emissions are the basis for forming the SEM images, localized fields can result in image contrast differences, darker or brighter areas than normal, depending on the voltage polarity that visualize circuit anomalies. For instance, assuming a Maxwellian energy distribution of the SE, applying a small positive voltage to a metal line will make it to be visualized as darker during SEM inspection than when it is grounded. Thus, if there is a discontinuity or a nonconducting junction along that line, one section of the line will appear dark (the one connected to the voltage) while the other section will appear bright. The collector system is assumed to act as a simple energy filter accepting only SE; all the SEs with an energy higher than that at the full width

at half maximum (FWHM) value of the SE emission curve will be collected (see, e.g., the pioneering work of Lin and Everhart (1979)).

When dynamic voltage contrast is needed, the electron beam is blanked in synchronism with the device clock rate. The SEM is used to image a semiconductor device powered up as it would be normally and clocked at its design frequency. Working in a stroboscopic mode (with operating frequencies ranging from 50 MHz to 100 GHz), it is possible to determine whether the device is operating at its design specifications. Pioneering work in this field was done between the early 1970s and the late 1980s by Thong *et al.* (1987).

From the aforementioned reasons, it is clear that this technique is mainly employed for industrial needs rather than for pure or applied research.

4.10.2.6 Scanning Deep-Level Transient Spectroscopy

Scanning deep-level transient spectroscopy (SDLTS) is a technique to detect the distribution of deep-level centers in semiconductors. SDLTS was first proposed by Petroff and Lang (1977) and was developed by Breitenstein and Heydenreich (1985). In this technique, the local area is excited by a pulsed electron beam and the resulting transient of capacitance or current is detected by a deep-level transient spectroscopy (DLTS) system. Similar to the EBIC technique, a semiconductor specimen with Schottky or p–n junction is used for DLTS. A pulsed electron beam is placed on a certain position, generating electrons and holes in a generation volume. Some of such carriers may be trapped at a deep-level state in the depletion region of the junction. Once the electron beam is off, these trapped carriers are thermally activated from this level after a certain time and the transient current or transient capacitance of this thermal emission is detected by DLTS system.

For the SDLTS measurement, however, it is necessary to prepare special equipments that are normally composed of (1) SEM with beam blanking system, (2) sample stage with cooling system for temperature sweeping, and (3) DLTS system with high sensitivity.

1. As for excitation, the electron beam should be on during the filling of traps, typically a few milliseconds. Then, the electron beam is off and the transient signal is recorded along few tens of milliseconds. Such pulsed electron beam is realized by blanking the SEM beam.
2. For DLTS spectroscopy, the specimen temperature should be varied in a certain range according to the trap levels. Typically, the specimen cooling system can vary the temperature from 50 to 300 K. Not only variation but also stabilization of temperature is necessary for SDLTS imaging.
3. Since the SDLTS signal is faint due to the small number of electrically active traps in the excited volume, the DLTS system should have high sensitivity. For capacitance DLTS measurement, the sensitivity of capacitance meter should be high, on the order of 10 fF. Such a high sensitivity is realized by adopting new techniques, such as correlator instead of Box-Car integrator.

Due to these difficulties of the detection and amplification of SDLTS signal, only a few groups have been succeeded in studying deep levels in actual semiconductors. Among them, seminal work in the SDLTS study of defects in Si, GaAs, and other semiconductors has been done, for example, by Breitenstein (1989).

4.10.3 Short Introduction to CL Spectroscopy and Imaging

Before we begin with this section, due to the huge number of references that should be quoted, the reader is referred to Yacobi and Holt (1990) as for the complete explanation of the physical processes involved in the CL technique and for its use in materials science. Concerning the references related to the specific content of the section, the reader is referred to Salviati *et al.* (2008). Therefore, in the following only the references strictly necessary will be quoted.

The CL is a widely used technique for spectral and imaging studies of the optical properties of solid-state materials. Since 1975 to date, more than 6250 papers on CL have been published in international journals, as can be found from the ISI Web of Science citation reports. The number of papers published testifies the interest of the scientific community in the CL and the main reasons will become clear in the following.

CL is the emission of photons as the result of the interaction between energetic electrons and matter. In semiconductors, the excitation by a highly energetic electron beam generates electron–hole (e–h)

pairs within a specimen volume. The excess carriers then thermalize and diffuse inside the material and finally recombine, either by nonradiative processes or by photon emission.

CL spectroscopy is a powerful method which allows one to study local variations in composition, impurity concentration and doping, the influence of different phases and crystal defects on the optical emissions, etc. A spectral acquisition of the intensity as a function of wavelength as well as a mapping of the intensity and wavelength distributions can be performed. Time-resolved CL spectroscopy with a time resolution on the picosecond scale can also be carried out. All the aforementioned modes are conducted by combining optical spectroscopy and electron microscopy with submicrometric lateral (in-plane) and in-depth resolutions. A wide range of applications is possible for different classes of materials, from semiconductor bulk, hetero- and nanostructures to rare earth compounds, and from diamond to geological specimens.

CL investigations can be performed by means of different types of electron beam sources, like high-energy electrons (100–400 keV) inside a transmission electron microscope (TEM), low-energy electrons (1–40 keV) inside an SEM, or very low energy electrons (tenths of volts) in the case of a scanning tunnel microscope equipment. The lateral resolution of the technique is strongly influenced by the beam/sample interaction volume, which is mainly determined by the electron energy. For example, in the case of TEM-CL, the reduced thickness of the typical TEM foil combined to the high energy of the electrons and the very small diameter of the beam allow one to increase the lateral resolution of about one order of magnitude with respect to the SEM mode.

The intrinsic limitation of the CL lateral resolution due to the generation/recombination volume is overcome by combining the peculiarity of atomic force microscopy (AFM) and SEM techniques. The experimental setup developed for this new technique, scanning near-field cathodoluminescence (SNCLM), is described in Section 4.10.1.

Compared to other luminescence techniques such as photoluminescence (PL) and electroluminescence (EL), there are some peculiar aspects associated to the nature of the excitation processes which mark the CL, for example, the generation and recombination volumes and rates. However, the basic luminescence mechanisms responsible for the radiative transitions, both in bulk materials and quantum confined structures, are the same for the different forms of excitation (**Figure 1**; Salviati *et al.*, 2008). We can distinguish between two types of transitions:

1. Intrinsic emissions which are due to recombination of electrons and holes across the fundamental energy gap, by interband transitions from the bottom of the conduction band to the top of the valence band. In the spectral region close to the energy gap, we can detect free excitons or bound excitons, with one of the carriers localized at an impurity center.
2. Extrinsic luminescence which is due to radiative transitions involving states in the band gap, shallow or deep, mainly due to native defects and impurities complexes acting as donor or acceptor centers. Different processes of recombination between free carriers and trapped carriers can take place, basically indicated as free-to-bound transitions (e.g., donor-to-free-hole (D°h), free-electron-to-acceptor (eA°), and donor-to-acceptor pair (DAP)).

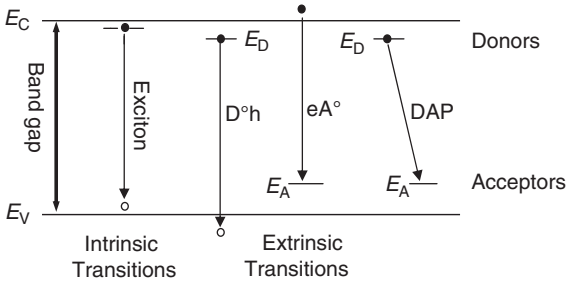

Figure 1 Schematic diagram of radiative transitions in a direct-band-gap semiconductor. From Salviati G, Rossi F, Armani N, Grillo V, and Lazzarini L (2008) Power dependent cathodoluminescence in III-nitrides heterostructures: From internal field screening to controlled band gap modulation. In: Lamberti C (ed.) *Characterization of Semiconductor Heterostructures and Nanostructures*, ch. 7, pp. 209–248. Amsterdam: Elsevier.

A detailed analysis of the nature, transition probability, and behavior under varying experimental conditions (temperature, excitation power, etc.) of the aforementioned optical transitions is a wide and more general subject which is beyond the purpose of this short treatment. For a complete and deep discussion, the reader is referred to, for instance, Pankove (1971), Pavesi and Guzzi (1994), and Yacobi and Holt (1990).

In CL analysis performed under steady-state conditions, once radiative carrier recombination occurs, the emitted photons propagate inside the material and the fraction coming out from the sample is finally collected and detected. The intensity of the recorded CL signal (L_{CL}) can be expressed as

$$L_{CL} = \int_V F(z)\frac{\Delta n(r)}{\tau_{rr}}\mathrm{d}V \qquad (1)$$

where $\Delta n(r)$ is the stationary excess carrier density at the position r, τ_{rr} is the radiative recombination lifetime, and F is a function defining the amount of photons actually leaving the surface as a function of the generation coordinate: in this expression a translation invariance of the optical response in the x–y direction has been supposed; therefore, F is just a function of the z-coordinate.

Equation (1) states that, given the number of photons emitted by radiative carrier recombination inside the material, the intensity of the recorded CL signal depends through F (Grillo *et al.*, 2007) on factors accounting for:

1. processes of self-absorption of photons by the material along their path;
2. internal losses due to scattering/reflection of the light at interfaces, and finally at the surface; and
3. CL collection/detection system response.

The latter must consider experimental setup parameters such as the overall collection efficiency of the light detection system, including also the fraction of solid angle covered above the specimen, the losses due to all the optical elements, the transmissive efficiency of the monochromator, the signal amplification factor, and the detector quantum efficiency, and yield which is a function of the frequency.

4.10.3.1 The CL Experimental Setup in the SEM

The most diffuse CL setup uses an SEM beam as a probe. In a typical CL experimental setup, the only peculiarity to be taken into account, since it influences to a different extent the integrated intensities of deep and band-to-band type CL emissions, is that the electron beam dwells on each single point of the sample for a time t, which depends on the scan rate (typical conditions $t = 67j$ ns at a TV/j scan rate, $j = 1, 2, 4, 8, 16, \ldots$). Comparing the electron beam dwell time with average carrier lifetimes of near band edge (NBE) transitions, for instance, in III–V(N), we can assume to be in stationary conditions. A steady-state emission spectroscopy is so performed.

The CL signal coming out from the sample can be collected in two main ways: placing an optical fiber close to the analyzed sample or using a mirror, of ellipsoidal or parabolic shape, positioned exactly above the sample surface. A light guide is used for signal transport to the detection system, outside the microscope: a monochromator for light dispersion (**Figure 2**) and a set of detectors, for the visible or infrared light, with related signal processing systems. The intensity of the cathode ray tube is modulated by one of the signals recorded, coming from the

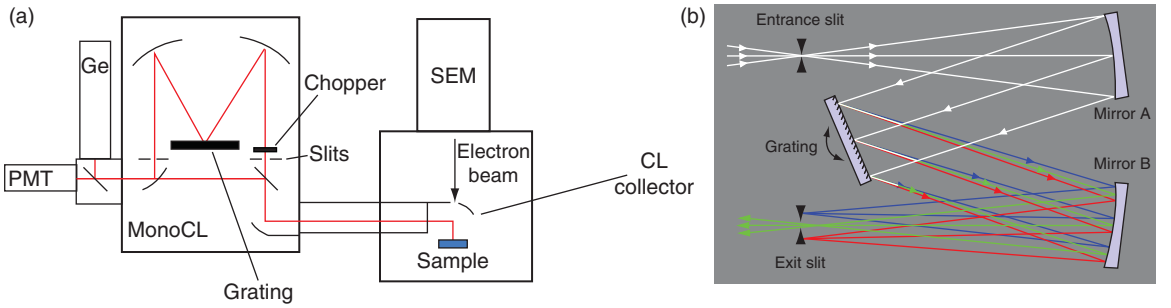

Figure 2 (a) Schematic path of the light from sample to the detectors. (b) Diagram of the light paths inside a typical Czerny–Turner monochromator using a dispersion grating. From Salviati G, Rossi F, Armani N, Grillo V, and Lazzarini L (2008) Power dependent cathodoluminescence in III-nitrides heterostructures: From internal field screening to controlled band gap modulation. In: Lamberti C (ed.) *Characterization of Semiconductor Heterostructures and Nanostructures*, ch. 7, pp. 209–248. Amsterdam: Elsevier.

detectors of secondary and BSEs or from the CL detection system to form an image. The specimen temperature can be controlled by a cryostat between 6 and 300 K, flux of liquid helium or liquid nitrogen being employed to reach 6 or 77 K. The entire SEM column is kept in vacuum at $10^{-6} - 10^{-7}$ torr by mechanical and turbomolecular pumps.

A recent improvement of the dispersion/detection system is the parallel detection mode, which uses a photodiode or array of diodes in spite of the standard photomultiplier as detector (**Figure 3**). This configuration has given a strong impulse to the use of the CL technique as a suitable characterization technique, since it allows very fast acquisition times (typically from 0.5 to 40 s) so minimizing the damage effects induced by electron beam irradiation. This is particularly valuable for the study of emission properties and emission decay rates in beam-sensitive materials such as organic crystals. In addition, an *ad hoc* software able to control the electron beam movements and the CL signal acquisition permits to work in the so-called spectral imaging mode. This CL mode enables one to acquire up to four analog and four pulse inputs simultaneously, to choose pixel image size in X and Y dimensions with a pixel dwell time from 400 ns to 400 ms per pixel. Alternatively, n-spectra $(1 \leq n \leq 256)$ may be acquired by dividing the array via software into vertical tracks.

The spectral resolution of a CL system is determined by the luminescence efficiency of the material and by the monochromator parameters. In particular, its focal length, the density of the dispersion grating, and the width of the entry and exit slits, improving for longer focal length, higher density of the grating and narrower slits.

As a general trend, accurate CL studies require a low specimen temperature to separate contiguous emission peaks, due to the line width narrowing and the increase in intensity usually obtained by lowering the temperature.

The examples shown here were carried out using different SEMs and commercial or home-made CL systems. Therefore, the reader is referred to the original papers for technical details.

Three types of CL analyses can be performed with this standard setup:

1. Spectral analysis, with a spectral resolution dependent on the working parameters but typically far under 1 nm (min 0.05 nm).
2. Analysis of the spatial distribution of the luminescence by pan-chromatic and monochromatic CL maps, allowing one to carry out correlated spectral and spatial studies. Complementary morphologic SEM information from submicroscopic regions allows, for example, one to spatially localize non-radiative centers.
3. A time-dependent analysis on a timescale of tens of seconds. The time evolution of a given transition intensity and the dynamic change of the relative integrated intensities of different emissions are indicative of point defect migration, breaking of complexes, and/or other damage effects, intentionally induced in a controlled way by *ex situ* thermal treatments or by the *in situ* electron beam irradiation.

It has to be noted that, in dedicated CL systems, time-resolved analyses are possible. Differently to the more standard time-resolved PL studies employing a pulsed laser, the major difficulty in performing

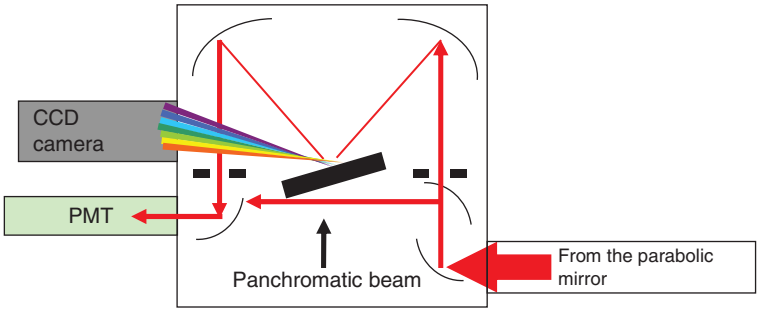

Figure 3 Scheme of the CL setup for parallel detection system using a modified Czerny–Turner monochromator and a CCD camera as visible light detector. From Salviati G, Rossi F, Armani N, Grillo V, and Lazzarini L (2008) Power dependent cathodoluminescence in III-nitrides heterostructures: From internal field screening to controlled band gap modulation. In: Lamberti C (ed.) *Characterization of Semiconductor Heterostructures and Nanostructures*, ch. 7, pp. 209–248. Amsterdam: Elsevier.

time-resolved CL analyses is the difficulty to have a short pulsed electron beam, with a subnanosecond period. This is achieved in two different ways:

- by blanking the electron beam of the SEM by means of a short pulsed electric field (up to 1 GHz); the time resolution of this kind of analysis is around tenths of nanoseconds and
- by employing an alternative intriguing method to achieve a time resolution in the picosecond range is obtained by redesigning the electron beam source and by generating the primary electrons from a gold target hitted by a excimer picosecond pulsed laser (see the following example on time-resolved CL).

In the first case a conventional detecting system synchronized to the electron beam is enough to have good results, while in the case of the picoseconds system, the use of a highly sensitive streak camera, typical for time-resolved PL analyses, is necessary. For picosecond time-resolved analysis, a modified system is required, while for studies on the nanosecond scale a commercial beam blanking system is usually suitable.

4.10.3.2 Lateral, In-Depth, and Analytical Resolution

The lateral resolution in CL imaging can be roughly defined as the minimum detectable distance between two regions presenting different CL intensity. In the SEM-CL the spatial imaging resolution depends mainly on the size of the recombination volume (generation volume broadened by the diffusion length) of e–h pairs inside the material, entailing also a dependence on the diffusion length of minority carriers. A second factor affecting the resolution is the electron probe diameter on the specimen surface, which depends on the beam current following a power law. A typical value of the lateral resolution of about 100 nm in far-field conditions can be reached as a lower limit in suitable working conditions, for instance, on III–V semiconducting quantum confined heterostructures. A topic apart is represented by free-standing nanoribbons, wires or belts etc., since single nanowire spectroscopy can be achieved by CL. In this case, the lateral resolution is only determined by the width and thickness of the nanoribbon. CL spectroscopy and imaging of nanobelts of 50 nm in diameter can be easily performed (see, e.g., Sekiguchi *et al.*, 2004; Salviati *et al.*, 2005).

The in-depth analysis is a CL peculiarity which permits to vary, in a single experiment, the electron penetration range through a controlled beam energy variation.

A proper value of the beam current at each voltage must be calculated in order to balance the variation of the explored volume by an adequate dose change (Grillo *et al.*, 2003). This procedure also allows one to avoid artifacts in detecting in-depth inhomogeneities, which could affect the shape, the energy position, and the intensity of the emission bands, in summary the analytical resolution (see below).

By properly comparing depth-resolved CL spectroscopy and HRTEM studies (see, e.g., Salviati *et al.*, 1999), this experimental procedure can also allow for a correlation of defect-related states and excitonic transitions with stacking faults in epitaxial GaN. The experimental evidence has been explained for the first time on the basis of a model based on the concept of excitons bound to SFs that form a quantum well of cubic material in the wurtzite (WZ) lattice of the layer.

The achievable resolution, Δt, related to the depth-dose function, is of the order of 100 nm, or lower, in controlled conditions (Gustafsson *et al.*, 1998), in particular for low-dimensional structures where a quantum confinement of the carriers is achieved.

As for the CL analytical resolution, let us introduce it as the "local sensitivity as a function of lateral or in-depth resolutions," being the sensitivity the minimum detectable variation of chemical and physical properties, such as dopants, impurities, point and extended defects, compositional variations, internal fields, etc. As an example of the outer sensitivity limit in a conventional experimental setup, it has been reported how adding 1 monolayer of GaN in GaN/AlN stacked self-assembled QDs resulted in an average energy shift of the CL emission energy of about 150 meV (Salviati *et al.*, 2004).

4.10.3.3 Role of Excitation Conditions

The dependence of CL on excitation conditions and materials properties is a wide field whose detailed discussion is beyond the scope of this chapter. Here only two points affecting the CL signals will be shortly treated. A wider description of that dependence can be found in Yacobi and Holt (1990: ch. 4).

4.10.3.3.1 CL Emission Efficiency, Energy Peak Position, and Line Shape Broadening

The possibility of varying in a single experiment and in a controlled way the injection power for any given generation–recombination volume is the main peculiarity of the SEM-CL technique. Beam current, beam voltage, and focusing conditions, during prolonged electron beam irradiations at high beam currents, can determine significant changes in peak intensity, energy values, and line shape of the CL spectra, with respect to low injection conditions.

The CL emission efficiency, L_{CL}, generally depends on both beam current and voltage and, according to Yacobi and Holt (1990) and references therein, can be written as

$$L_{CL} = f(I_b)(V - V_0)^n \qquad (2)$$

where V_0 is a dead voltage, accounting for surface nonradiative recombinations (Section 4.10.1.2.2), and $1 \leq n \leq 2$. The value of V_0 is affected mainly by materials properties and primary beam brilliance; in the specific case of very efficient GaN layers, with the experimental setup previously sketched and using a conventional SEM, V_0 was found to be around 0.25 keV (Salviati *et al.*, 2001). $f(I_b)$ is a power function of the beam current ($f(I_b) \propto {I_b}^m$), which assumes values partly dependent on the type of transition but strongly influenced by a large number of variable parameters. In general (Dean, 1982), a sublinear ($m < 1$) dependence of $f(I_b)$ has been reported for extrinsic DAP and deep-level related emissions, whereas a linear ($m = 1$) or superlinear dependence ($m > 1$ and, in particular, $m = 2$ in GaN layers) has been observed for the near-band-edge emission intensity (Phillips *et al.*, 2003). In addition to defect concentration, e–h pair density, and injection rates, there is evidence of beam size and focusing-related effects on absolute and relative intensities and energy position of the CL bands (Castaldini *et al.*, 2002). Roughly, defocusing the electron beam on the sample surface without changing the e-beam energy results in a broadening of the beam size and in a modified carrier distribution inside the generation volume which can be quantitatively determined only using complicated experimental procedures (Jahn *et al.*, 2003). However, since the influence of materials on defocusing effects has also to be considered, results of general validity are not yet provided.

To get reliable CL analyses, self-absorption effects should also be taken into consideration since they cause noticeable modifications of the relative intensity and of the energy peak baricenter in the outcoming CL spectra (Knobloch *et al.*, 1998).

As regards the band emission energy values, for specific transitions, they depend on the carrier density, hence on the excitation conditions. A typical example is the DAP recombination that shifts to higher energies as the excitation intensity increases independently on the excitation source. This follows from the reciprocal dependence of the peak energy on the pair separation, r, and on the reduction of the transition probability with increasing r (Pavesi and Guzzi, 1994). Concerning CL, the aforesaid effect is much stronger due to the wider excitation range achievable. An outstanding case of the advantages offered by CL spectroscopy in nitrides is the carrier recombination in nanostructures, where an inverse quantum confined Stark effect is obtained by e–h pair generation. This subject is reviewed in Section 4.10.4.4 on power-dependent CL.

As already mentioned, CL is particularly useful for in-depth studies, provided the electron generation and recombination volumes can be properly simulated. However, since primary electrons accelerated at keV energies in general activate all the luminescence mechanisms of the material, whereas PL emission is limited by the laser frequency, the main point is the different role of thermalization processes in PL and CL experiments and the different energy level population. In fact, the electron beam excitation entails stronger energy transfer to the lattice and phonon emission, and the temperature of the excess carriers remains usually higher. All these factors produce a line width broadening of the CL bands compared to PL transitions.

Furthermore, for most of the generation conditions, the e–h pair density is higher in CL than in PL and carriers populate more energetic levels of the semiconductor. This causes also a strong dependence on the scan rate of the transitions involving levels with longer carrier lifetime, because the kinetics of the filling or emptying of traps can be commensurate with the raster of the electron beam. If the scan rate is reduced or even the spot mode is used (in this configuration the e-beam is spatially steady in a defined surface specimen position), the electron beam dwells on the same area and these levels are saturated earlier. For example, this is observed for the yellow band in GaN, whose integrated intensity relative to the near band edge peak is minimum in the spot mode and maximum in

standard TV scan, and strongly exceeds that detected in PL experiments.

Finally, the influence of electron irradiation on the specimen temperature has to be considered. The electron beam-induced sample heating has been estimated by Myhajlenko *et al.* (1983) on the basis of the Vine–Einstein model (Vine and Einstein, 1964), predicting a maximum temperature rise under steady-state conditions from

$$\left(\frac{P}{a}\right)_{\text{eff}} = 4.27 \int_{Tsub}^{T} k(T)\mathrm{d}(T) \qquad (3)$$

Where P is the beam power (in W), a the beam radius (in cm), $k(T)$ the thermal conductivity (in $\mathrm{W\,cm^{-1}\,K^{-1}}$) and $(P/a)_{\text{eff}}$ the effective beam power corrected for the penetration. Typical temperature rises of about 150 K were achieved for ZnSe with substrate temperature of 300 K, E_b=30 keV, $I_b = 10\,\mu\text{A}$, and beam diameter of 3 μm. Reducing the substrate temperature to 100 K, a temperature rise of 30 K was estimated. It has to be noted that by increasing the temperature, the shape of both intrinsic (edge emission) and extrinsic emission bands cannot be entirely described by a Gaussian function of symmetrical shape. Actually, the shape around the peak is asymmetric with high- and low-energy exponential tails.

As a further notice, artifacts on the CL contrast from extended defects can also be induced by local specimen heating. For instance, contrast inversion at a dislocation in GaAs:Se substrate has been evidenced by increasing the electron beam current from 10^{-6} to 10^{-5} A. The effect has been explained in terms of localized heating leading to enhanced nonradiative recombination at the dislocation line and to a decrease of the CL signal.

4.10.4 Short Introduction to EBIC Theory

EBIC is another well-established technique for characterizing semiconductors. As known, e–h pairs are generated during electron beam (e-beam) irradiation of semiconductors. Different from CL that detects the luminescence out of specimen, EBIC collects the carriers (electrons or holes) inside the specimen. EBIC method is widely used for the identification of extended defects as well as carrier lifetime measurement in semiconductor materials and devices. Here, we introduce the EBIC principle and instrumentation, and then we mainly focus on its recent applications to semiconductors.

4.10.4.1 Principle

EBIC system is usually integrated in an SEM, which provides an e-beam for the bombardment of semiconductor samples. EBIC can be performed in planar or cross-sectional mode, as schematically shown in **Figure 4**. In the planar mode (**Figure 4(a)** or **4(c)**), a Schottky barrier or p–n junction is perpendicular to the e-beam, whereas in the cross-sectional mode (**Figure 4(b)** or **4(d)**), it is parallel to the e-beam. During the e-beam irradiation, a number of e–h pairs are generated in an excitation volume (pear-shape). The local rate of carrier pair generation is simply expressed as (Leamy, 1982)

$$g = \langle g \rangle \frac{EI(1-f)}{qE_{\text{eh}}} (\text{carrier pairs/sec}) \qquad (4)$$

where $\langle g \rangle$ is the normalized distribution, E the energy of e-beam, I the beam current, f the fraction of e-beam that is reflected by the sample, q the electron charge, and E_{eh} the energy cost for the formation of a single e–h pair. Using this equation, for example, a 20 kV e-beam of 1 nA creates roughly $\sim 3 \times 10^{13}$ carrier pairs per second in Si.

The generated electrons and holes diffuse in the specimen and are separated by an internal electric filed (in the depletion region) supplied by a Schottky barrier (**Figure 4(a)** or **4(b)**) or a p–n junction (**Figure 4(c)** or **4(d)**). The field drifts electrons and holes to the opposite directions. If an external circuit is connected, those separated carriers flow through this circuit, producing the EBIC signal. For analyzing EBIC current, it is enough to consider minority carriers in the specimen. Normally, EBIC signal is in the order of μA, and an amplifier is needed to magnify the current for the EBIC imaging.

Planar EBIC is mostly used to image the distribution of electrically active defects in semiconductors. The defects generally act as recombination centers for carriers. Therefore, when the e-beam scans across the sample, the EBIC signal is weak in areas around defects and strong in areas free of defects. In this way, the defects are seen as dark features in contrast to the background regions.

In cross-sectional EBIC, when the e-beam is placed near the depletion region, EBIC signal becomes strong due to the carrier collection by the

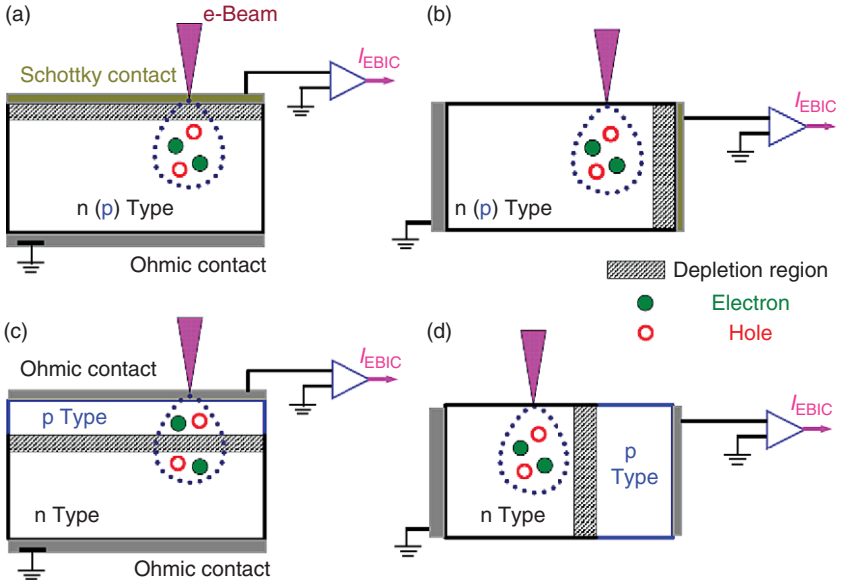

Figure 4 Schematic diagrams showing the geometries for charge collection. (a, b) Planar and cross-sectional EBIC in Schottky barrier case. (c, d) Planar and cross-sectional EBIC in *p–n* junction case.

internal electric field. When the e-beam scans away from the depletion region, few minority carriers can diffuse there, resulting in the weak EBIC signal. Thus, contrast in cross-sectional EBIC is strongly related to the diffusion length of minority carriers in semiconductors (Donolato, 1982; Gonzalez *et al.*, 2001). Cross-sectional EBIC is usually applied to identify the location of p–n junctions (corresponding to the peak EBIC signal) and to measure the minority carrier diffusion length.

4.10.4.2 Experimental Setup

Figure 5 shows a block diagram of an SEM used for EBIC measurement (Sekiguchi and Sumino, 1995). This system is composed of four components, that is, an electron gun, an electrical signal detecting unit for EBIC, a cooling stage, and a PC controller. EBIC is normally performed at several to several tens of kilovolts with a beam current in the order of 10^{-11}–10^{-9} A. EBIC signal is amplified through a current amplifier, with the output signal in the form of an analog voltage. Then, this analog voltage is converted through an A/D converter to record the absolute EBIC current. Finally, an EBIC mapping image will appear on the computer screen.

4.10.4.3 Operating Condition

Generally, EBIC can be operated in four types of conditions, namely, (1) normal; (2) temperature dependent; (3) depth dependent, and (4) bias dependent.

Normal: It means that EBIC is performed at a suitable accelerating voltage (e.g., 20 kV) at a room temperature (RT). In this normal condition, the distribution of electrically active defects can be recorded in EBIC images.

Temperature dependent: By using a cooling stage, temperature-dependent analysis is applicable within the range from several tens K to RT. The energy levels of the defects can be estimated from their temperature-dependent behavior in terms of Shockley–Read–Hall (SRH) statistics (Shockley and Read, 1952; Kusanagi *et al.*, 1995).

Depth dependent: A schematic of this technique is shown in **Figure 6(a)**. The electron range R_e (penetration depth) varies according to the accelerating voltage, which can be simply calculated from the equation proposed by (Kanaya and Okayama, 1972)

$$R_e = \frac{2.76 \times 10^{-11} A E_0^{\,5/3}}{\rho \times Z^{8/9}} \qquad (5)$$

where E_0 is the beam energy (keV), A the atomic weight (g mol^{-1}), ρ the density (g cm^{-3}), and Z the

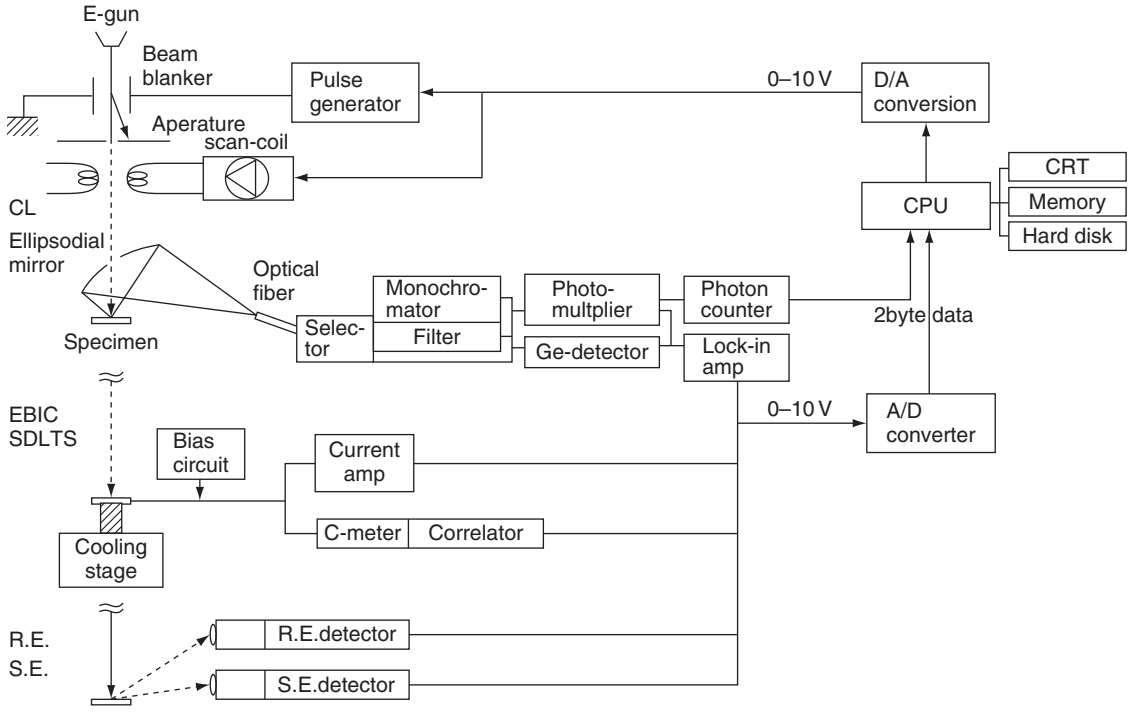

Figure 5 Block diagram of an EBIC testing system. From Sekiguchi T and Sumino K (1995) Quantitative electron-beam tester for defects in semiconductors (CL/EBIC/SDLTS system). *Review of Scientific Instruments* 66: 4277–4282.

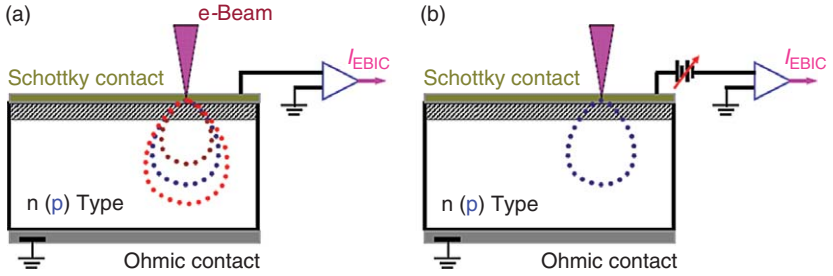

Figure 6 (a) Schematic of depth-dependent EBIC and (b) schematic of bias-dependent EBIC.

atomic number of the analyzed material. The electron ranges of e-beam in typical semiconductors, such as Si, SiC, GaN, and ZnO, are shown in Figure 7. Using this technique, the defects at different depths in a specimen can be resolved.

Bias dependent: If a forward or reverse bias is applied, as schematically shown in Figure 6(b), the barrier height of Schottky diodes or p–n junctions will be altered. Following this alteration, the charge collection at defect regions may be saturated and leakage current may occur. This technique is effective and widely used to find out the leakage sites in semiconductor devices.

4.10.5 Reviewing CL Emblematic Examples from the Literature

In the following, a few examples of the potentiality and limits of SEM-CL in the characterization of the optical and electro-optical properties of semiconductors are given.

Due to the specific topics of this chapter and to the restricted number of words allowed, for all the examples reviewed in the following, only CL spectroscopy and imaging will be reported, leaving the reader to refer to the original papers for deeper insights, for results given by complementary

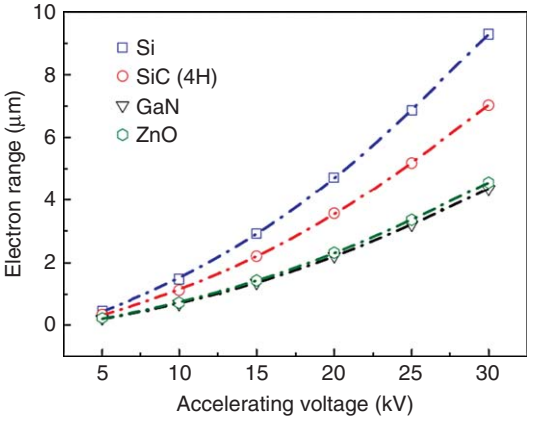

Figure 7 Electron ranges of e-beam in Si, SiC, GaN, and ZnO semiconductors.

techniques, for the experimental details, and for a complete bibliography.

4.10.5.1 CL Spectroscopy and Imaging of Unpredicted Cubic Phase in ZnO Tetrapods

The paper reviewed in the following (Lazzarini *et al.*, 2009) is representative of the corners of ultimate analytical sensitivity and spatial resolution of the CL technique. It reports for the first time on the comparison between SEM-CL and HRTEM studies on the concurrent presence of cubic and hexagonal phases inside the arms of ZnO nanotetrapods.

Tailoring the structural and electronic properties of 3D nanostructures via bottom-up techniques would pave the way for novel low-cost applications. One of such possibilities is offered by ZnO branched nanostructures such as tetrapods (TPs) that have recently attracted attention for nanodevice applications from nanoelectronics to drug delivery. ZnO is a direct-band-gap (exp ~ 3.3. eV) semiconductor crystallizing in the WZ structure; the zincblende (ZB) structure, which differs from WZ at the third neighbor only, is not observed in nature since it is thermodynamically metastable. ZnO TPs, which are normally grown by strongly nonadiabatic techniques, can however present polytypism due to the presence of a common polar axis and of the similarity of the nonpolar facets containing the full stacking sequence. However, until now, there was no evidence in the literature of a WZ structure in TP arms. On the other hand, till now, the conventional picture was that ZnO arms are thermodynamically stable only in the WZ phase.

In this example, the authors provide the first experimental evidence of unpredicted extended ZB phases (50–60 nm long) embedded in the arms of ZnO WZ tetrapods by correlating high lateral resolution CL spectroscopy, monochromatic contrast maps, and atomic resolution transmission electron microscopy images of ZnO single TPs.

In addition to the obvious interest for a new result of basic research, the growth of WZ ZnO branched nanostructures containing the ZB phase allows in principle one to interface different crystallographic structures exhibiting different band gaps, electronic and elastic properties. This offers novel routes in the design of nanodevices made by a single nanostructure.

Figure 8 shows a typical CL spectrum of a TP of micrometric dimensions collected from the high-temperature reactor zone (~650 °C). Accurate Gaussian multi-peak deconvolution procedures gave the main peak centered at 3.36 eV due to four bands. The first one at 3.373 eV is assigned to the WZ ZnO free exciton (FX) emission and the remaining ones at 3.363, 3.354, and 3.352 eV are assigned to bound exciton to neutral donor transitions (D^0X). Furthermore, the peaks at 3.308 and 3.314 eV are found to be due to WZ exciton-to-neutral acceptor (A^0X) or the first LO phonon replica of the WZ phase and free electron-to-neutral acceptor (A^0e) transitions with the acceptor states confined to basal SFs, respectively.

As for the band at 3.29 eV, on the basis of recent works, the authors can unambiguously state that it arises from the ZB NBE emission. The 3.236 and 3.213 eV transitions are due to WZ and ZB LO phonon replicas, respectively.

Figure 9 reports the monochromatic images of the spatial distribution of WZ and ZB emissions from a single tetrapod of micrometric dimensions. **Figure 9(a)** shows the conventional SEM image of the specific tetrapod studied. In **Figure 9(b)** the spatial distribution of the NBE emission of the WZ phase obtained collecting a monochromatic CL image at 3.36 eV is shown. It is apparent that the CL emission from the hexagonal phase is homogeneously distributed all across the TP arms except for the presence of triangular-shaped nonradiative recombination lines (marked with yellow arrows) at the interface between the TP core and the protruding arms. An additional fainter dark line can also be seen along one of the arms (red arrow). The authors ascribe the dark lines to basal-plane SFs at the boundaries between the arms (WZ/WZ interface with a twin relationship) or between the arms and the core (WZ/WZ or possibly ZB/WZ interface) and/or to twin boundaries. Accurate HRTEM

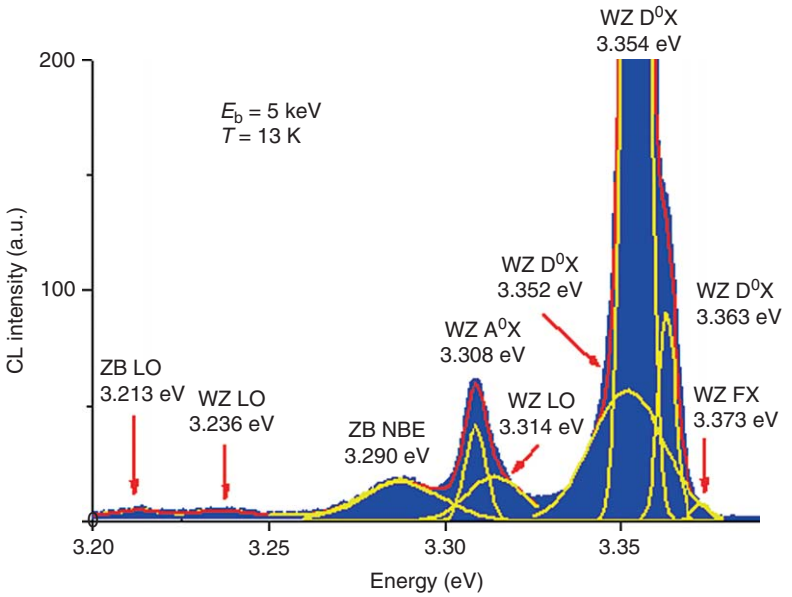

Figure 8 Experimental CL spectrum of the micrometric ZnO TP collected from a high-temperature zone of the reactor. $T = 13$ K, beam energy $E_b = 5$ keV. From Lazzarini L, Salviati G, Fabbri F, *et al*. (2009) Unpredicted nucleation of extended zinc blende phases in wurtzite ZnO nanotetrapod arms. *ACS Nano* 9: doi:10.1021/nn900558q.

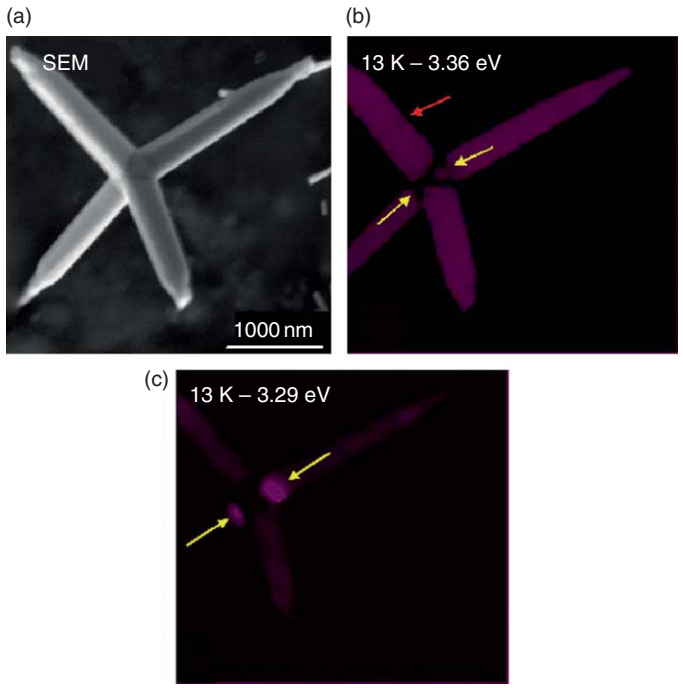

Figure 9 Comparison among the secondary electron (SE) (**Figure 10(a)**) and low-temperature monochromatic CL images in false colors (**Figures 10(b)–10(c)**) taken at the NBE energy values of WZ (3.36 eV) and ZB (3.29 eV) phases, respectively. The ZB related emission in **Figure 3(c)** comes from SFs located at the TP interface between core and legs. The TP has been collected from the high-temperature zone of the reactor ($T = 650\,^{\circ}$C). From Lazzarini L, Salviati G, Fabbri F, *et al*. (2009) Unpredicted nucleation of extended zinc blende phases in wurtzite ZnO nanotetrapod arms. *ACS Nano* 9: doi:10.1021/nn900558q.

studies of the core structure of the TPs with variable dimensions confirmed that assignation.

The micrograph in **Figure 9(c)** is taken by collecting and imaging only the CL emissions of the ZB phase at 3.29 eV. The presence of a cubic phase on the basis of the protruding arm is apparent. It is known from the literature that the TPs nucleate from a hexagonal core; as a consequence, there is a serious possibility that the CL monochromatic imaging at 3.29 eV cannot be due to a massive cubic phase inside the TP cores. HRTEM studies, contrary to what was expected from previous results, showed that the TPs investigated, independently on the leg dimensions, did not present any extended portions of cubic symmetry at the TP cores. Therefore, the emission at 3.29 eV must be ascribed to the nucleation of SFs and/or TBs , which is in agreement with the structural results that consider the formation of basal-plane stacking faults at the leg/core interfaces as the driving force for the nucleation of the WZ phase onto a ZB one.

The reason of the strong localization of the CL cubic emission at the SFs is that the WZ/ZB interface exhibits a type-II line-up. The SFs induce a downward shift of the conduction band minimum (CBM); they have a direct band gap at Γ and act as quantum well-like structures for electrons and holes. However, the SFs are not supposed to induce any quantum confinement since the CBM states are not to be found very localized.

It is also worth noting that TPs with arms longer than 500 nm (collected from the higher-temperature zones of the reactor) did not show any massive cubic phases, being the width of SFs and/or twins only of a few atomic layers. Note that the lateral dimension of the CL emission contrast from the ZB areas is larger than the size of the SFs because of the influence of the experimental parameters on the lateral resolution of the CL technique (Salviati *et al.*, 2008).

When TPs with arms shorter than 200–300 nm in length are investigated, a different scenario appears. **Figures 10(a)** and **10(b)** show the SEM images of a TP with arms shorter than 200 nm and the low-temperature CL spectra from the core and one tip, respectively. In this case, the presence of cubic phase emission also at the TP tip is found, as confirmed by accurate Gaussian deconvolution reported in the inset of **Figure 10(b)**. In some cases, it has been possible to image the monochromatic CL emission from the cubic phase along the arm as shown in **Figures 10(c)** and **10(d)**. Also in this case, HRTEM studies reveal extended cubic phases at the TP arm tips (50–80 nm long and wide and thick as the TP arm). A possible explanation of the difference between micrometric and nanometric TPs concerning the formation of massive ZB phases along the arms could be ascribed to the fact that the TPs directly nucleate while floating in the vapor phase at very high Zn and O supersaturation conditions, that is, far from the thermodynamic equilibrium. The nanometric-sized TPs nucleate in a oven area at $200\,^{\circ}C < T < 415\,^{\circ}C$, so the influence of the temperature gradient and Zn and O supersaturation conditions inside the reactor has been considered responsible for alternating bulk ZB/WZ phases inside the arms of the smallest tetrapods.

4.10.5.2 Impuritiy Contamination and Nonhomogeneous Elemental Distribution in Low-Dimensional Structures

The problem of impurity contamination and of the alloy chemical homogeneity control in semiconductor heterostructures is still debated in the specialized literature since it is well known that they can affect both optical and transport properties of materials and corresponding devices. In many semiconductors, the introduction of impurities at dilute concentrations leads to dramatic changes in the electronic, optical, and magnetic properties. For example, the introduction of a few percent of nitrogen into GaAs leads to a band gap red shift of hundreds of meV. Furthermore, the incorporation of a few percent of manganese into GaAs enables a combination of semiconducting and ferromagnetic behavior.

In most cases, the density of impurities is so high that there is no possibility of distinguishing the effects of the individual impurities. Individual impurities are of interest when dealing with low-dimensional structures that, having reduced volume, can contain only a few of them. Fluctuation of this number, together with the low dimensionality, influences the optical and electrical properties of the nanostructures and, in turn, the performance of the devices based on them. Seminal work on the use of SEM-CL in that field has been done by Samuelson and Gustafsson (1995) who demonstrated that single impurities can be accessed by CL, using special sample designs. In the following, first, the spectroscopy study and optical imaging of single C impurities in GaAs quantum wire (QWR) and QW stripes (Gustafsson *et al.*, 1998) are presented. Then, it is shown (Hidalgo *et al.*, 2009) that CL can give a

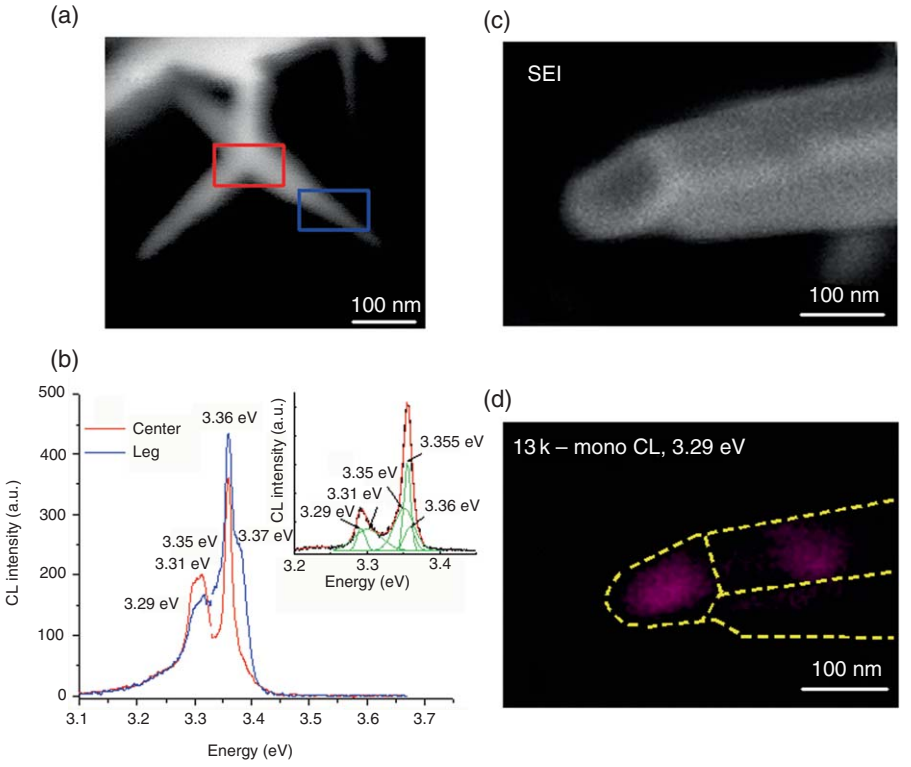

Figure 10 (a) SEM micrograph of a nanometric TP, (b) The blue and red CL spectra have been collected from the blue and red rectangular areas in (a). The inset represents the CL spectrum from the whole TP. Gaussian deconvolution procedures gave the usual WZ and ZB energy values. The CL spectra have been acquired at a beam energy $E_b = 5$ kV, $T = 10$ K and 500 000 times of magnification. For that reason the spectra are slightly noisy. (c) SEM picture of a portion of a TP arm of about 500 nm in length, (d) False color monochromatic CL image of the same area as in (c). The emission from the ZB phase (3.29 eV) at the arm tip and from an intermediate zone is shown. From Lazzarini L, Salviati G, Fabbri F, *et al*. (2009) Unpredicted nucleation of extended zinc blende phases in wurtzite ZnO nanotetrapod arms. *ACS Nano* 9: doi:10.1021/nn900558q.

reliable insight on the presence of impurities and native defects in GeO_2 NWs doped with different ions.

The QWR structures grown on V-grooved substrates, described in **Figure 11**, are ideal for studying the effect of single impurities, either in the GaAs QWR themselves or in the GaAs QW stripes between them (Gustafsson *et al*., 1998). This sample design is such that, with a doping level of $\sim 10^{15}$ cm^{-3} typical of residual carbon in MOVPE-grown GaAs, the inter-impurity distance is around 1 µm in the QW stripe and more in the QWR that makes it possible for the CL to resolve emissions from single impurity.

The spectrum taken at 10 pA, reported in **Figure 12**, presents three main features: the QWR emission at 1.54 eV, the planar QW at 1.61 eV, and a peak at 1.59 eV that is attributed to recombination via carbon acceptors (C_{As}) in the planar QW.

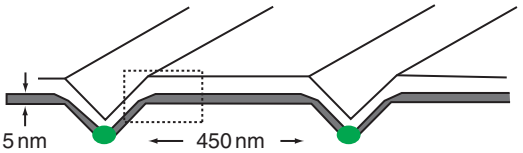

Figure 11 Sketch of a stacked geometry where 5-nm-thick (001) QWs are separated by a periodic array of V grooves with a 765 nm period. The QW on the sidewall of the V groove (significantly thinner than the (001) QW) acts as a lateral barrier that prevents the diffusion between different (001) QW areas. This effect is enhanced by a thick QWR at the groove bottom (roughly not-in-scale sketched as green areas). The dotted area marks the thinner QW region where its orientation goes from (001) to (111) via (311). From Samuelson L and Gustafsson A (1995) Imaging and spectroscopic studies of individual impurities in quantum structures. *Physical Review Letters* 74(12): 2395–2398.

Monochromatic images of the C_{As} peak show bright spots, corresponding to single C_{As}. These bright spots show a reversed contrast compared

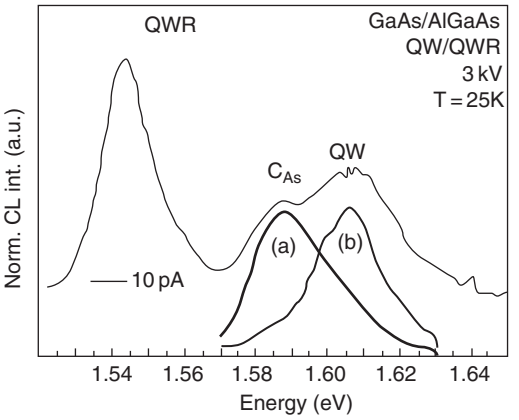

Figure 12 At a CL probe current of 10 pA and a sample temperature of 25 K, the spectrum of a V-groove QWR structure exhibited three peaks: one from the QWR, one from the QW, and a third on the low-energy side of the QW peak, which was identified as the emission via carbon acceptors in the QW. In the spot mode spectra, the two features were isolated: (a) a spectrum with almost only C_{As} emission and (b) only intrinsic QW emission. Courtesy of A. Gustafsson.

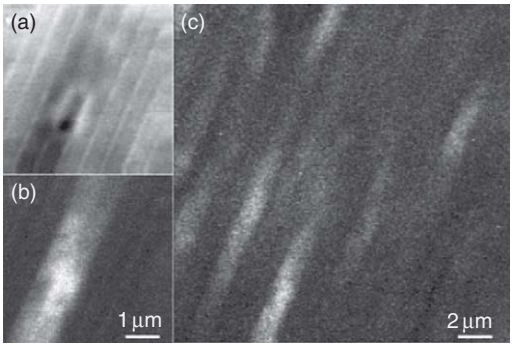

Figure 13 (a) Low magnification monochromatic CL at 1.54 eV detecting the intrinsic QWR emission, where the individual QWRs are shown, (b) In the image of the C_{As} emission, a single C_{As} can be observed, (c) The bright spots corresponding to the single C_{As} in the QWR are separated by several μm along the QWR. The images were recorded at 25 K. From Gustafsson A, Pistol ME, Montelius L, and Samuelson L (1998) Local probe techniques for luminescence studies of low-dimensional semiconductor structures. *Journal of Applied Physics* 84(4): 1715–1775.

with the image obtained using the main QW peak. In fact, the spectra acquired in spot mode on a bright area and on a dark area, denoted in **Figure 12** as (a) and (b) respectively, are dominated by a single peak. This made it possible to demonstrate the access to single impurities in 5-nm-thick GaAs QW 450-nm wide, where the C_{As} density measured in CL images well agrees with the expected concentration of residual carbon (Samuelson and Gustafsson, 1995). The effect of impurities can be observed in the QWRs of the same sample. Due to the smaller volume of the QWR, the separation between the impurities is much larger.

Figure 13(a) shows a monochromatic top-view image of an area, containing several QWRs appearing as bright lines. **Figure 13(b)** shows the monochromatic CL micrograph of the same area, but obtained at a 25-meV lower energy. Here, one bright spot can be observed. The spot is centered at one of the QWRs and is caused by one single C_{As} in the QWR. The shape of the bright spot illustrates the collection area for this part of the QWR, limited by the two adjacent QWRs (physically limited by the VQWs of the adjacent grooves). Along the groove, the size of the bright spot is determined by carrier diffusion along the QWR, several millimeters in this case. **Figure 13(c)** shows a larger area of the sample, illustrating the positions of several impurities. In the QWR the spacing is several tens of micrometers. As a final comment, in our opinion, the imaging of individual carbon acceptors in QWRs is one of the corners of ultimate sensitivity for CL.

The second example reviewed in Hidalgo *et al.* (2009) shows the spectral potentiality of the SEM-CL in investigating complex light emission spectra from GeO_2 NWs doped with optically active rare earth ions (Er and Eu) and metal impurities (Sn and Mn).

Doping of self-assembled semiconductor oxide nanostructures is an expanding field with challenging unresolved problems, such as interplay between native defects and impurities and/or efficient solubility of the impurities inside the crystal lattice. As for the luminescence properties of such NWs, they are affected by the incorporation of metal ions that introduce localized states in the band gap bonded to oxygen vacancies.

Concerning the experimental details of the growth procedures and characterization techniques, r the reader is referred to the original paper. The NWs investigated were 200–400 nm wide and several micrometer long.

Figure 14(a) shows a typical CL spectrum of an undoped GeO_2 NW. Previous literature data suggest that the complex luminescence band is due to vacancy defects occurring in several configurations and/or forming complex defects. Moreover, due to the large surface/volume ratio, surface states must

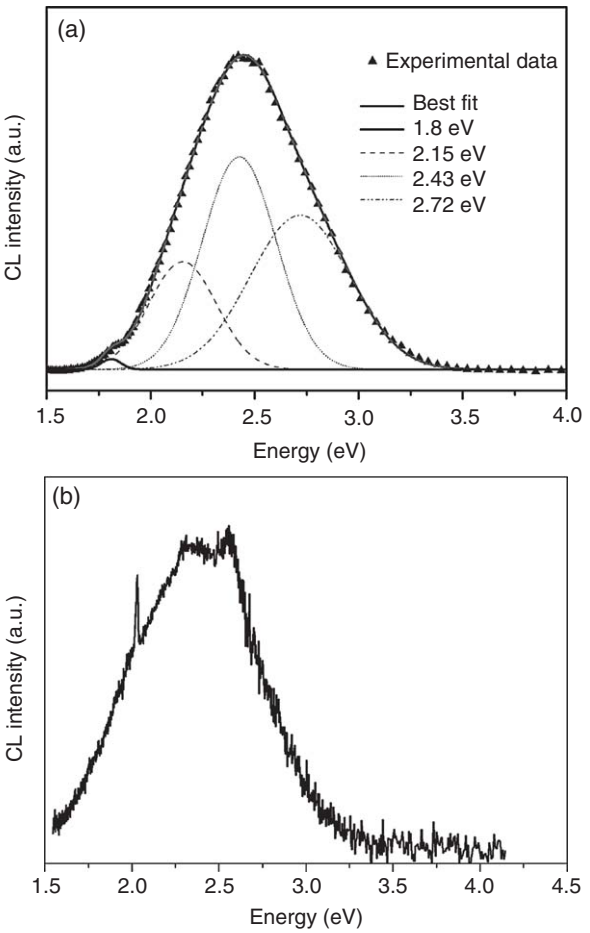

Figure 14 (a) CL spectrum of undoped GeO_2 NWs. Gaussian deconvolution of the band shows the four components (1.9, 2.17, 2.42, and 2.70 eV) that best fit the experiemental data. Similar CL spectrum is obtained in the case of S-doped GeO_2 nanowires. CL studies of GeO_2 crystals have reported a green band in GeO_2 quartz-like and glassy crystals, attributed to oxygen deficient centers. (b) CL spectra of Eu-doped GeO_2 nanowires. From Hidalgo P, Liberti E, Rodriguez-Lazcano Y, Mendez B, and Piqueras J (2009) GeO_2 nanowires doped with optically active ions. *Journal of Physics and Chemistry C* 113: 17200–17205.

also be considered to affect the luminescence properties of the NWs. **Figure 15(a)** reports the CL spectrum of Eu-doped NWs. A sharp Eu^{3+} line at 2.03 eV is observed on the lower energy side in the spectrum (the main visible Eu^{3+} emission lines are in the red region at about 2.03 eV).

When Er-doped GeO_2 NW are investigated, the CL bands reported in **Figure 15** are found. Visible CL spectrum from Er-doped wires exhibits an intense broad green band as shown in **Figure 15(a)**. Deconvolution of the spectrum shows that a proper fit to the experimental curve is obtained when the 2.42 eV band is present in the spectra of the green emission related to Er^{3+} ions. Hence, erbium doping leads to an increase of green emission of GeO_2 nanowires. The luminescence mechanism in rare earth-doped semiconductors is usually due to an energy-transfer process between the host lattice and the rare earth ion. In this case, since the main luminescence band of the GeO_2 NWs lies in the green region, a resonant excitation of the Er emission could take place leading to an increase of the total CL signal.

A near-infrared CL emission has also been found (**Figure 15(b)**) with the 0.8 eV (1.54 μm) peak characteristic of Er^{3+} ions.

The other dopant of GeO_2 nanowires investigated was Mn, which is an impurity of interest in the field of diluted magnetic semiconductors. Visible CL spectra from Mn-doped GeO_2 NWs show a broadband in the visible range composed by four peaks at 1.75, 2.15, 2.41, and 2.75 eV, as shown in **Figure 15(c)** (solid line). The last three peaks are present in undoped and Sn-doped GeO_2 wires and are associated with oxygen vacancy defects, whereas the 1.75 eV band was only observed in Mn-doped samples. A red shift of the emitted light, in doped nanowires, due to the increase of the 2.15 eV component is observed. The CL spectrum of undoped nanowires (dashed line) is also shown in **Figure 15(c)**, for comparison. Therefore, a modification of luminescence, with changes in the CL spectrum, has been detected by Mn doping of GeO_2 nanowires, probably due to electron–phonon interaction between the electronic levels of Mn atoms and the host crystal.

The authors have then performed X-ray photoelectron spectroscopy (XPS) investigations in order to confirm the CL data. No Er and Mn surface signals were detected in Er- and Mn-doped GeO_2 NWs, while Ge(3d) and O(1d) core levels were measured. Briefly, in Mn-doped GeO_2 nanowires XPS revealed that the wires were not completely homogeneous and certain mixture of oxides is present in the surface. This effect is limited to the surface, while the crystal structure of the wires is that of GeO_2 as measured by XRD. This observation could account for the complex visible luminescence bands observed in doped GeO_2 NWs. The authors ascribed the final oxidation state of germanium oxide to the thermal oxidation of an initial Ge-metal oxide mixture and the presence of several species during the growth process and concluded that the addition of impurities may slightly influence the Ge(3d) and O(1s) core energy

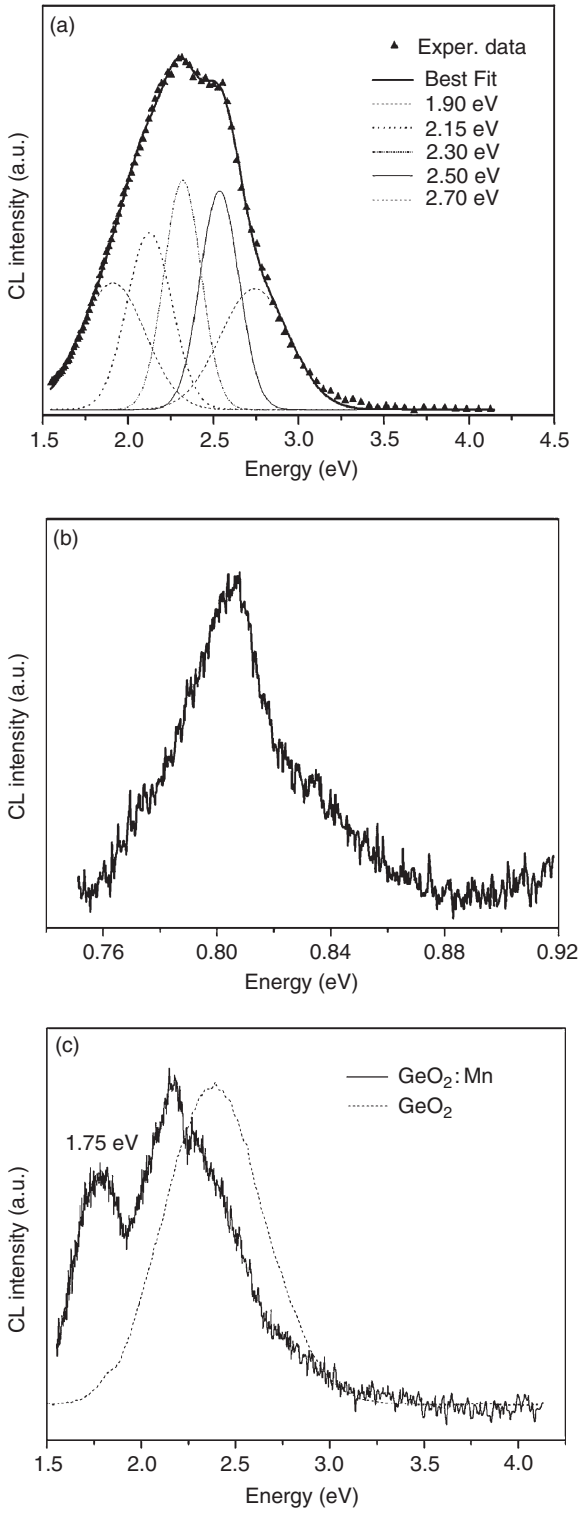

Figure 15 (a) Visible CL spectrum from Er-doped GeO_2 nanowires, showing the deconvoluted bands to fit the experimental results. (b) Infrared CL emission from the GeO_2 nanowires, showing the 0.80 eV erbium line. (c) CL spectra from undoped (dashed line) and Mn-doped (solid line) GeO_2 nanowires. A new peak at 1.75 eV appears in Mn-doped samples. From Hidalgo P, Liberti E, Rodriguez-Lazcano Y, Mendez B, and Piqueras J (2009) GeO_2 nanowires doped with optically active ions. *Journal of Physics and Chemistry C* 113: 17200–17205.

levels so leading to a different contribution of the luminescence bands in the CL spectra.

4.10.5.3 CL of Rare-Earth-Doped Oxynitrides for Field Emission Displays

III–V group nitrides such as AlN, GaN, InGaN, and AlInGaN have been intensively investigated because of their potential applications in blue-UV optoelectronic devices (see, e.g., Xie and Hirosaki (2007) and references therein enclosed). On the contrary, less attention has been paid to the luminescence of silicon-based oxynitride and nitride compound phosphors despite they are considered excellent candidates for white light-emitting diodes (LEDs) and field emission displays (FEDs).

FEDs have attracted much attention as replacement for liquid crystal displays and plasma displays because of their high-contrast, wide-view angle and low power consumption. FEDs consist of an array of addressable cold cathode field emitters that will emit electrons. These electrons will excite phosphors, which will finally emit the light. Consequently, for the development of FEDs, it is mandatory to develop new phosphors with high luminescence efficiency and a good stability under electron beam irradiation.

Rare-earth-doped phosphors have been intensively investigated due to amazing optical properties. The luminescence properties of rare-earth ions are influenced by their valence, their concentration in the host lattice, and their position in the host lattice. In general, the luminescence of rare-earth ions in the divalent state comes from 5d–4f electronic transitions. The emission spectrum consists of a broadband with peak position varying with the host lattice due to the strong interaction between 5d orbitals and the crystal field. Indeed, the 5d-excited state is not strongly shielded from the crystal field of the $5s^2$ and $5p^6$ electrons. While in the trivalent state, the luminescence is ascribed to the inner 4f–4f transitions. Their emission is a sharp band at fixed peak position since it is weakly influenced by the host lattice. Thus, a wide range of wavelength, from the ultraviolet to the infrared, can be easily achieved.

Until now, the most commonly utilized phosphors are sulfide- ($SrGa_2S_4$:Ce, Y_2O_2S:Eu, etc.) and oxide-based (Y_2SiO_5:Ce, Y_3AlO_{12}:Ce, etc.) phosphors. However, sulfide-based phosphors are thermally unstable and very sensitive to moisture, inducing a serious degradation of their luminescence during operation. On the other hand, most of the oxide-based phosphors have low efficiency and low color purity. Consequently, to solve these problems and develop high-performance phosphors, it is essential to explore new kinds of host crystals.

One promising host-lattice family is (oxy)nitride phosphors, in reason of their good luminescence properties, wide band gap, and high chemical and physical stability. Thus, III–V group nitrides such as AlN, GaN, InGaN, and AlInGaN have been intensively investigated because of their potential applications in blue-UV optoelectronic devices. However, the binary covalent nitrides cannot be easily considered as host lattices due to the lack of suitable sites for rare-earth ions. Such limitation has been removed by the development of multinary covalent nitrides, such as SiAlON phosphors.

To illustrate this point, we give the example of Eu doping in AlN. In the case of AlN thin films doped with Eu, red line emission related to the electron transition of 4f–4f of Eu^{3+} is usually observed, due to the occupation of Al site by Eu. Then, Hara *et al.* (2004) found by PL studies that Eu:AlN powders had a broadband emission in the green region (530 nm), which they attributed to the 5d–4f transition of Eu^{2+}. However, trying to co-doped AlN with Eu and Si, Hirosaki *et al.* (2007) achieved a different interpretation of the results of Hara *et al.* through CL analysis. Indeed, while the spectra give information about the luminescence centers present in the materials, they only give an average of the luminescence. It is necessary to detect their distribution in order to determine correctly their origins, which may successfully be accomplished by CL.

The example we review in the following deals with the luminescence properties of Si,Eu-co-doped AlN phosphors (Dierre *et al.*, 2009) in view of they use in FEDs.

Figure 16(a) shows the CL spectrum of Eu-doped AlN at 5 kV and 1 nA. The luminescence consists of a strong peak at 360 nm, which is attributed to defects in AlN, and a weak band at 550 nm, similar to that of Hara *et al.* (2004). This band does not exist for undoped AlN, which suggests that it is well related to Eu^{2+}. **Figures 16(b)** and **16(d)** show the CL images of 360 and 550 nm emissions of Eu:AlN. The 360 nm emission is uniformly distributed on the particles, while the 550 nm emission is distributed between the particles, namely at their boundaries. Thus, contrary to an initial attribution, the 550 nm emission is not related to Eu^{2+} in AlN, and is in reality related to a secondary phase, probably a Eu-related compound, such Eu–Al–O–N. To confirm this result, SEM–EDS measurements (EDS, energy dispersive X-ray

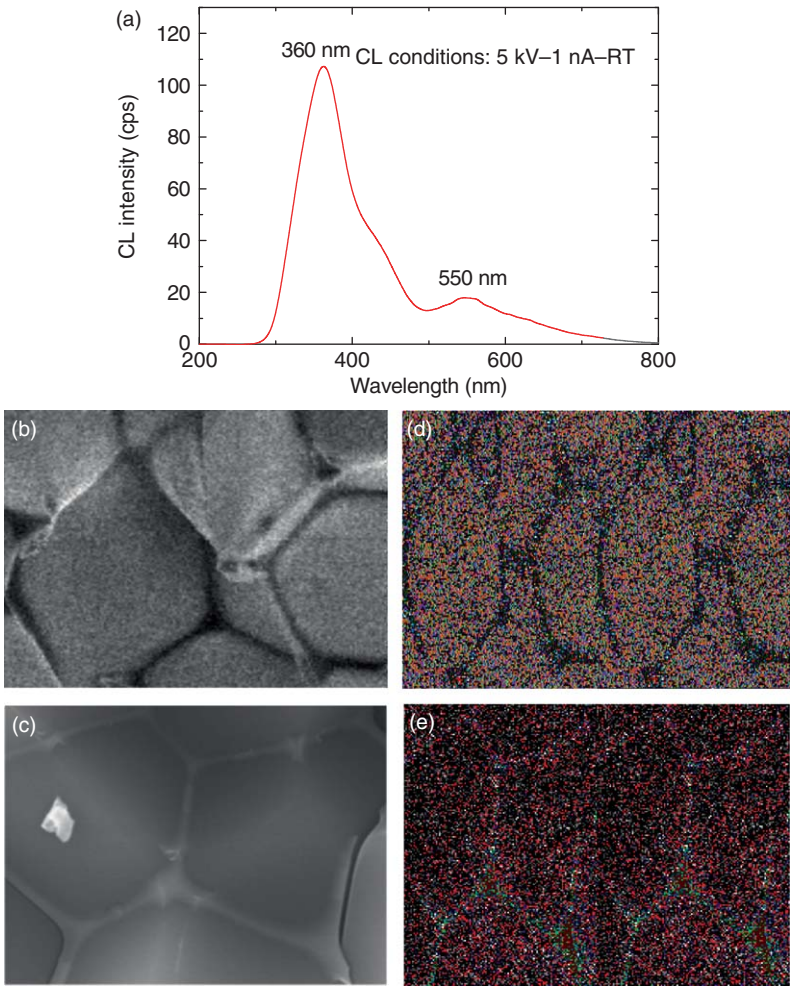

Figure 16 (a) CL spectrum of the Eu–AlN sample imaged in part (c); (b) CL image – 360 nm; (c) secondary electron image; (d) CL image – 550 nm; and (e) EDS distribution map of Eu. From Dierre B, Yuan XL, Inoue K, Hirosaki N, Xie R-J, and Sekiguchi T (2009) Role of Si in the luminescence of AlN:Eu,Si phosphors. *Journal of the American Ceramic Society* 92(6): 1272–1275.

spectroscopy) were performed. **Figures 16(c)** and **16(e)** show the SE image and the corresponding Eu distribution for Eu:AlN. Eu is clearly more abundant at the boundary and shows a similar distribution to the CL image of 550 nm.

When Eu:AlN is co-doped with Si, the 550 nm emission is suppressed, whereas an emission at 470 nm clearly appears, as shown in **Figure 17(a)**. This peak increases with increase of Eu concentration to 2 at.%, which suggests that it is also related to Eu^{2+}. **Figures 17(b)** and **17(d)** show the CL images of 360 and 460 nm emissions of Eu:AlN. In this case, both 360 and 460 nm emissions are uniformly distributed on the particles.

This result is confirmed by SEM–EDS (**Figure 17(e)**), which reveals homogenous distribution of Eu. The results suggest that the 460 nm is well related to Eu^{2+} in AlN and that Si is necessary for the incorporation of Eu in AlN. We may suppose that Si will favor the incorporation of Eu by creating some defects (as Al vacancies), and that, in order to keep the charge balance in the material, the incorporation of Si^{4+} in AlN induces the existence of Eu in the divalent state.

This example shows how CL was crucial for the understanding of the doping of rare-earth ions in (oxy)nitride host lattice. Such results were obtained by using the unique advantages CL versus PL, which are basically:

- the stronger excitation that allows one to detect the AlN and Eu luminescence;
- the local excitation that permits to image the luminescence spatial distribution; and

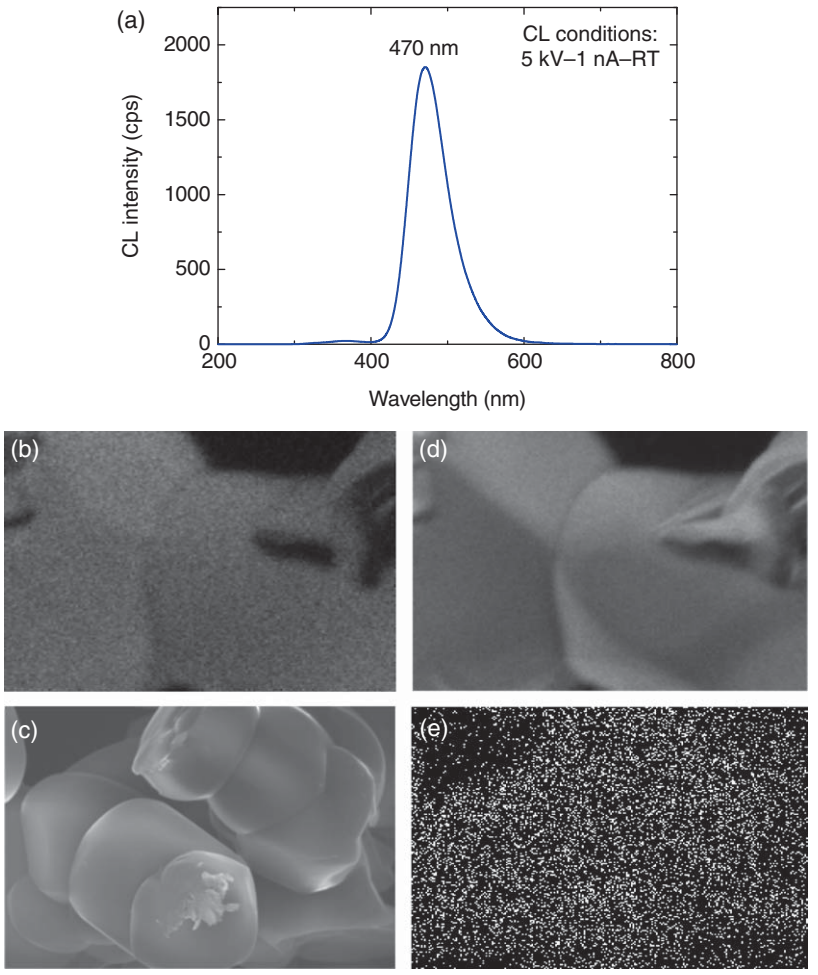

Figure 17 (a) CL spectrum of a Eu:AlN sample codoped with Si; the 550 nm emissions is almost totally suppressed, whereas a strong emission at 470 nm due to Eu^{2+} clearly appears. (b, d) CL images of the spatial distribution of 360 and 470 nm emissions of Eu:AlN. (c) Low magnification SE image of the sample doped with 6% atomic of Si. (e) EDS distribution of Eu. Courtesy of B. Dierre.

- the use of electron to excite luminescence that allows a direct comparison with other electron-based techniques such as EDS.

4.10.5.4 Power and Depth-Resolved CL

Along with the obvious possibility of detecting the spatial inhomogeneities of the optical signal, a further peculiarity of SEM-CL is given by the possibility of varying the electron beam penetration depth, that is, the specimen interaction volume by changing the accelerating voltage in the SEM under constant power injection conditions (depth-resolved CL). Keeping the injected power constant is an important constraint when quantitative CL has to be carried out in samples where the integrated intensities of the CL bands depend on the excitation conditions. This makes it possible to selectively collect CL spectra whose optical transitions come from different zones of multilayers and devices both along and perpendicularly to the growth axis without artifacts (Schäfer *et al.*, 1998). Suitable computer programs have to be used to simulate the carrier diffusion inside the heterostructure (see Grillo *et al.*, 2003). The last and less explored feature offered by SEM-CL concerns the possibility of changing the injection power in a controlled way (from 10^8 to 10^{12} cm^{-2} injected carriers) in order to simulate and detect *in situ* degradation mechanisms (Pavesi *et al.*, 2004), or to counterbalance, for example, in nitride-based semiconductors, internal electric fields to restore flat band conditions (Armani *et al.*, 2004), or even to achieve in-plane band-gap modulation (Felici *et al.*, 2006).

In the following, an example of the aforementioned experimental CL modes will be reviewed.

4.10.5.4.1 Power-dependent CL screening of internal fields in low indium content InGaN/GaN multi-quantum wells

The InGaN multi-quantum wells (MQWs) have been widely used in the production of solid-state lighting devices, such as blue, green, and violet LEDs and ultraviolet laser diodes. Nevertheless, the presence of some unsolved problems such as large lattice mismatches between the epilayers and the substrates, high density of native defects, dislocation and domain boundaries, internal fields, compositional fluctuations, and even packaging procedures cause shortening of the lifetime of devices (e.g., InGaN-based green LEDs used as traffic lights). Therefore, the goal of 100 000 h of operation, as for red LEDs, is still far from being achieved.

The quantum energy levels and the carrier dynamics in InGaN/GaN QWs are mainly controlled by the built-in electrostatic field, induced either by the different spontaneous polarizations in the layers of the nanostructure or by the piezoelectric polarization in the strained heterolayers that depend on many structural parameters: growth design, doping, surface/interface states, and, last but not least, alloy composition (Zoroddu *et al.*, 2001).

The interplay between localization- and internal field-induced effects and their interaction with the carriers generated by an external excitation source is still a matter of study. The free carrier screening of the polarization fields (Della Sala *et al.*, 1999) has been typically analyzed by means of optical generation in PL experiments. However, these conventional studies, providing only a limited maximum sheet density (10^{10} carriers cm^{-2}), do not allow a wider investigation extending to the high-power regimes. This requires different excitation sources such as injection through an electron beam probe in CL studies (Salviati *et al.*, 2004).

The example reported in Armani *et al.* (2004) shows the interplay of polarization fields and free carrier screening in $In_xGa_{1-x}N/GaN$ ($0.03 < x < 0.07$) multiple quantum wells. The study combines PL (time-integrated and time-resolved) and CL, in an excitation density range from 10^8 to 10^{12} cm^{-2} of generated e–h pairs. For such low In content, the quantum-confined Stark effect is verified to rule the recombination dynamics, while effects of carrier localization in potential fluctuations have a minor role. Efficient field screening is demonstrated in CL steady-state high-injection conditions and in PL time-resolved experiments at the maximum excitation density. Under recovered nearly flat band conditions, quantum confinement effects are revealed and a high, possibly composition-dependent, bowing parameter is extrapolated. In **Figure 18** a sketch of the effect of different excitation densities on the band bending in GaN/InGaN/GaN MQWs is reported.

Here only the CL results are summarized, leaving the reader to refer to the original papers for the experimental details, for a deeper insight of the comparison between PL and CL experimental results and for radiative and nonradiative rates for carrier recombination in the wells as obtained by modeling the carrier dynamics in the framework of a theoretical rate equation model.

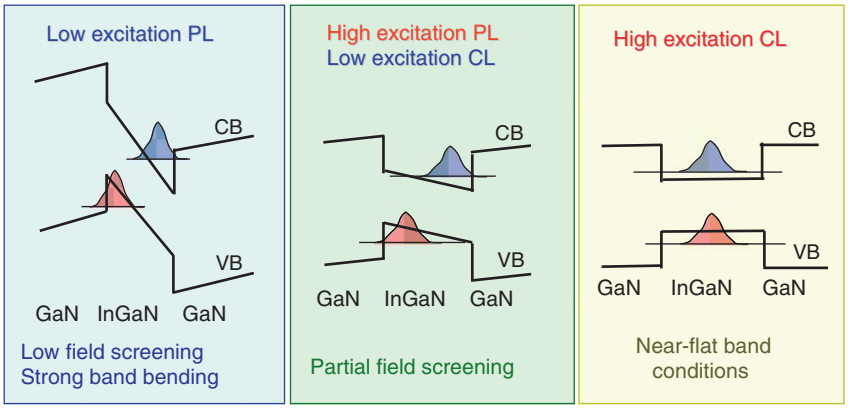

Figure 18 Sketch of the influence of the injection power on the band bending in the GaN/InGaN/GaN MQWs studied. From Rossi F, PhD Thesis (2004).

The dependence of the QW-related optical transition energy on the excitation conditions in PL and CL studies is determined by following its evolution under increasing power density. An almost rigid blue shift of the QW emission is obtained (see the representative spectra in **Figure 19**, mainly as a result of the internal field screening by the carriers generated over the wide range investigated (10^8–10^{12} carriers cm^{-2}).

The blue shift is accompanied by a continuous increase of the QW emission intensity due to the gradual recovering of the oscillator strength. It must be stressed that the position of the CL emission at the lowest injection, fixed at 3.07 eV as shown in the figure, presents its peak between the PL curves (solid lines) centered at 3.064 eV for the low-injection condition and 3.08 eV for the high excitation limit. This underlines that the two techniques identify two complementary power regimes and can be joined in the intermediate excitation region. We point out that, due to the effect of the screening, huge variations of the optical matrix element are found (Della Sala *et al.*, 1999). Consequently, for a fair comparison of the energy shifts, the spectra have been normalized. The systematic power-dependent analysis gives the complete energy evolution, as reported for instance in **Figure 20** for the 3.5-nm QW sample, where the values obtained from PL studies (blue symbols) are combined with the CL ones (red symbols). An overall blue shift of about 16 meV across the PL excitation range and 58 meV in the CL range is found in this structure at $T = 6$ K. CL is thus demonstrated to be effective in reaching the most efficient field screening.

A QW width dependence of the amount of blue shift at fixed composition has also been found by the authors. The shift decreases, as expected, from about 50 to 17 meV on decreasing the well thickness from 3.5 to 2 nm. Moreover, the increase of the QW emission energy for decreasing well width, as obtained from the CL results in the high-injection limit, has to be noted. In such conditions, any effect arising from possibly different internal fields is minimized. This confirms the existence of two-dimensional quantum carrier confinement in these InGaN nanostructures.

The authors have then well reproduced the experimental results in the framework of a theoretical model where a self-consistent solution of the Schrödinger–Poisson equations is coupled to a rate equation model to account for time-dependent effects of charge rearrangement to determine the electronic states in the nanostructure. Considering the correct material parameters of the InGaN/GaN alloys, including the bowing of the polarization fields and gap, the theoretical model is demonstrated to describe, in an unified scenario, either time-integrated PL or time-resolved PL and finally, CL, for samples having different well widths, that is, different internal polarization fields.

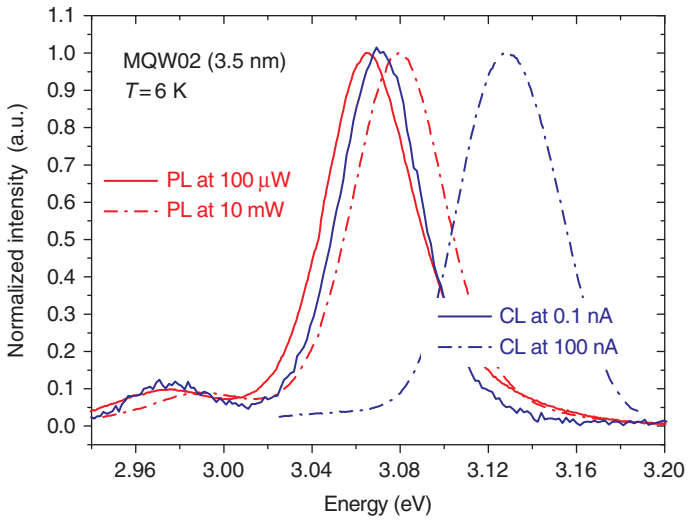

Figure 19 PL (solid lines) and CL (dotted lines) spectra obtained in the limit of minimum and maximum injection power (PL: 0.1 and 10 mW respectively; CL: $I_B = 0.1$ and 100 nA, respectively) for sample MQW02 at $T = 6$ K. The peak intensity has been normalized to unity. The period of the MQW02 was of 44 nm, the QW thickness of 3.5 nm, and the In composition $x = 0.060 \pm 0.004$. From Armani N, Rossi F, Ferrari C, *et al*. (2004) Polarization field effects on the recombination dynamics in low-In-content InGaN multi-quantum wells. *Superlattices and Microstructures* 36/4-6: 615–624.

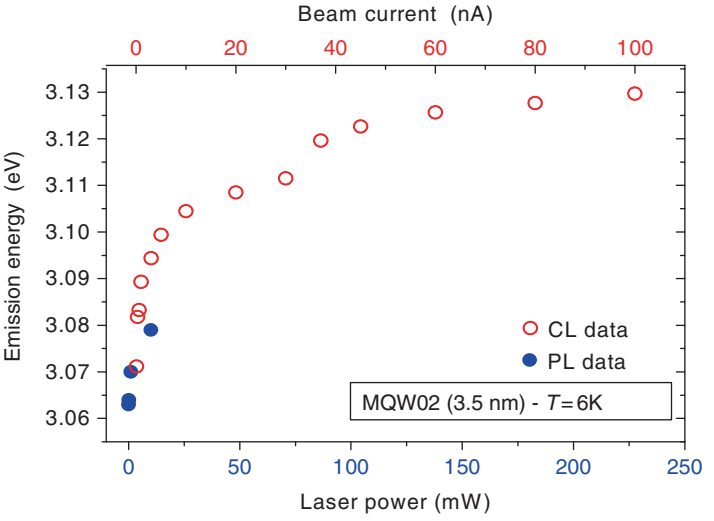

Figure 20 The dependence of the QW peak position on the excitation for sample MQW 02 at $T = 6$ K. Closed circle: PL data at 0.050, 0.100, 1 and 10 mW respectively. Open circles: the CL peak position in a current range 0.1–100 nA at EB = 10 keV. The measured total blue shift is about 58 meV in CL and 16 meV in PL, while the total value is of 67 meV. From Armani N, Rossi F, Ferrari C, *et al*. (2004) Polarization field effects on the recombination dynamics in low-In-content InGaN multi-quantum wells. *Superlattices and Microstructures* 36/4-6: 615–624.

4.10.5.4.2 Depth-resolved CL study of interface chemical interactions at metal–ZnO interfaces

The work reviewed by Mosbacker *et al.* (2007) reports on the use of depth-resolved cathodoluminescence spectroscopy (DRCLS) and current–voltage measurements to probe the influence of thermally induced interface chemical interactions in forming blocking layers and defects. Purpose of the work was to optimize the fabrication of thermally stable rectifying and ohmic contacts. It is shown how these interactions depend on the metal–ZnO bonding, the annealing temperature, and the initial bulk native defect concentration.

The fabrication of reliable rectifying and ohmic contacts is one of the most important tasks in the production of ZnO-based devices. In previous works, the authors showed how oxygen plasma processing removes adsorbates, subsurface hydrogen, and deep levels to improve Schottky barriers on ZnO crystals. In this work, they show that interface chemistry interactions induced by thermal treatments affect the formation of blocking layers and defects. Depth-resolved CL spectroscopy measurements reveal two classes of metal–ZnO reactions that determine the contacts' current–voltage (*I–V*) properties and thermal stability.

Brillson *et al.* (2007) showed that metals induce native point defects at ZnO interfaces. The corresponding CL emission bands were peaked at 2.1, 2.5, and ~3 eV. Similar results were found for Zn-rich or poor crystal growth. Among possible native defects, Zn and O vacancies are predicted to be the most energetically favorable (Kohan *et al.*, 2000), being the 2.1 and 2.5 eV optical transitions associated with Zn and O vacancies, respectively, by means of positron annihilation and electron paramagnetic resonance spectroscopies.

To probe the influence of thermally induced interface chemical interactions on the fabrication of thermally stable rectifying and ohmic contacts, DRCL has been first carried out on different contact typologies.

Figure 21 presents DRCL spectra for (a) Au and (b) Ta on low-defect ZnO(000–1). Annealing up to $T = 550\,^{\circ}$C leaves the Au/ZnO I(2.5 eV)/*I*(NBE) ratio nearly unchanged and introduces no new spectra features. However, at 650 °C, new emission appears at about 2 eV that dominates the deep-level spectra. Since Au forms a eutectic with Zn at 625 °C resulting in a CL emission at ~2.1 eV, Au–Zn alloying that extracts Zn from the substrate is believed to occur. In contrast, *I*(2.5 eV)/*I*(NBE) increases by more than 3 times with initial Ta deposition but adds no emission at ~2 or 2.5 eV up to 650 °C.

I–V curves on low-defect Au–Zn (000–1) interface display electrical features that correlate with these

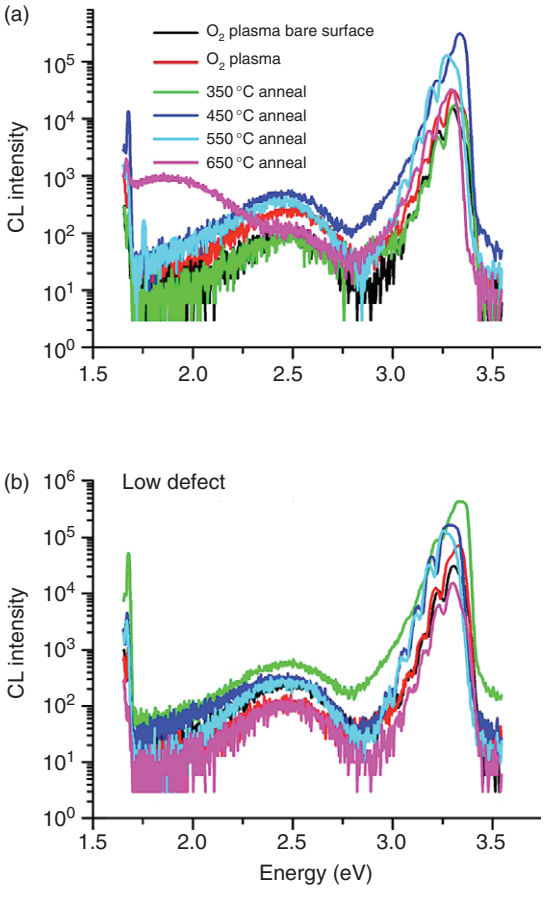

Figure 21 5 keV DRCLS of 30 nm (a) Au and (b) Ta deposited on low-defect (000–1) ZnO. For Au, annealing induces only slight changes for $T < 650\,^{\circ}C$ but a large ~2 eV peak at 650 °C. Initial Ta deposition triples 2.5 eV emission, but annealing induces no ~2 eV emission or further 2.5 growth. From Mosbacker HL, Zgrabik C, Hetzer MJ, *et al*. (2007) Thermally driven defect formation and blocking layers at metal–ZnO interfaces. *Applied Physics Letters* 91(7): 072102.

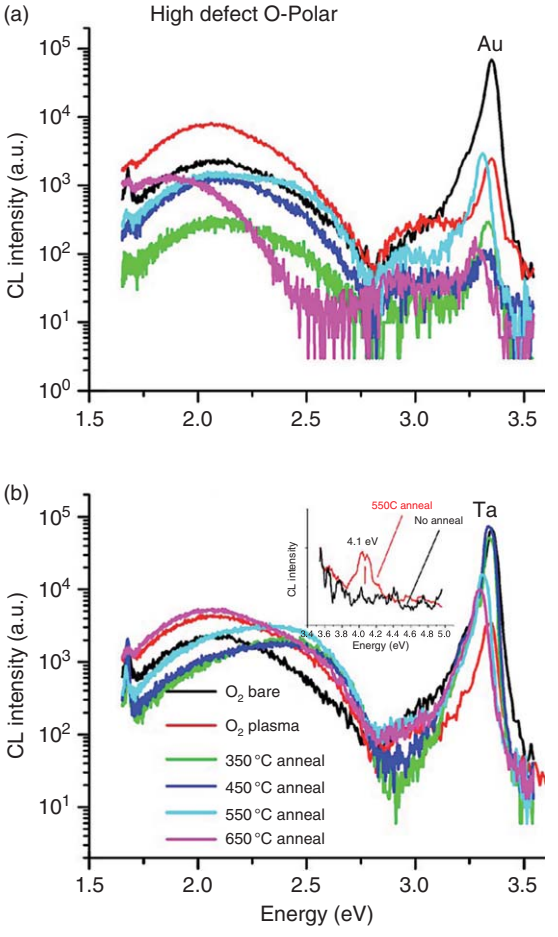

Figure 22 5 keV DRCLS of 30 nm (a) Au and (b) Ta on high-defect (000–1)ZnO. Intense 2.1, 2.5, and 3.0 eV emissions are dominated by ~2.1 eV emission for Au diodes at 650 °C. For Ta contacts, the 2.5 eV intensity increases with Ta deposition and subsequent annealing up to 550 °C. The inset shows ~4.1 eV peak associated with Ta oxide that appears only at 550 °C. From Mosbacker HL, Zgrabik C, Hetzer MJ, *et al*. (2007) Thermally driven defect formation and blocking layers at metal–ZnO interfaces. *Applied Physics Letters* 91(7): 072102.

DRCL spectra and reflect thermal stability up to 550 °C for low defect ZnO.

In extreme synthesis, after 450 °C annealing, the Au diodes remain strongly rectifying and after a 350 °C annealing, initially ohmic, blocking Ta–ZnO contacts form and an insulating oxide layer is formed by extracting O from the substrate.

Figure 22 shows a similar qualitative difference in CL spectral features between Au and Ta contacts on high-defect ZnO. Au deposition increases the 2.1 and 3 eV emissions, which increase proportionally with annealing. At 650 °C, the 2.1 eV defect emission again dominates. In contrast, both 2.1 and 2.5 eV emissions are evident for Ta diodes, with spectra dominated by 2.5 eV emission for intermediate temperatures, as in **Figure 21(b)**.

These defect changes are reflected in corresponding *I–V* spectra, showing the initially rectifying characteristics of Au Schottky barrier, corresponding to a 0.43 eV barrier that degrades steadily with elevated temperatures starting with 350 °C. Similarly, Ta contacts display initially ohmic features that become blocking only at 450 °C. The oxide layer responsible for this blocking is evident from the 5 keV DRCL spectra (inset of **Figure 22(b)**), displaying a new emission at ~4.1 eV (Ta_2O_5 band gap

~4.2 eV) that appears only after the 550 °C annealing. Significantly, this blocking feature degrades with 650 °C annealing (leakage current increases by (~105) and this 4.1 eV emission disappears.

Coupled with the increased defect emissions in Figure 22(**b**), these changes suggest that the oxide layer becomes less insulating as additional near-interface defects form.

For both high- and low-defect ZnO, Au and Ta contacts produce qualitatively different DRCLS and *I–V* features. Similar differences are evident for Pd and Pt (which, as with Au, alloy with Zn at elevated temperature) versus Al and Ir (which, as with Ta, form oxides). Thus, the increased 2.1 (2.5) eV emissions for Au (Ta) can be associated with Zn (O)-deficient defects near the metal interface.

Furthermore, comparing DRCLS and *I–V* characteristics, it becomes clear that highly defected ZnO has lower thermal stability for both Au and Ta contacts. Taken together, these results demonstrate that metals on ZnO form thin interfacial alloy or oxide layers whose nature depends on thermodynamic driving forces. These interfacial layers require either Zn or O atoms from the ZnO, resulting in nanometer-thick Zn- or O-deficient layers near the interface.

For Au on low-defect ZnO, the Schottky barrier remains stable and alloying begins only at temperatures above the known eutectic, while for highly defected material, the Schottky barrier degrades steadily as resident defects redistribute. The Zn-deficient emission dominates only above the eutectic temperature.

For Ta on low-defect-density ZnO, a blocking layer associated with O-deficient defects forms at low temperatures and remains stable with increasing temperature, while for high-defect-density ZnO, the contact is ohmic up to intermediate temperatures and its 550 °C blocking layer becomes leaky at higher temperatures.

This contrast between low- and high-defect ZnO contacts and their defect emission demonstrates that the presence of high-defect concentrations promotes interface alloying and reactions that produce additional defects that, in turn, degrade Schottky barriers and blocking layers. In order to achieve high Schottky barriers or blocking layers, defects at the intimate metal–ZnO interface must be minimized. For alloying metals such as Au, sub-eutectic temperatures are required to preserve Schottky barriers. For easily oxidizing metals such as Ta, temperatures must be high enough to promote oxide thicknesses sufficient to block current without concomitant defect concentrations high enough to disrupt this layer.

4.10.5.5 Time-Resolved CL

Time-resolved luminescence spectroscopy (TRLS) is an extremely powerful technique to get information on the intrinsic time constant ruling the carrier dynamics. This is done by studying the different relaxation processes of the photoexcited carriers in a semiconductor (hetero)-structure after ultrafast (picosecond or femtosecond) excitation pulses. For a general review of time-resolved spectroscopy, the reader is referred to, for example, Shah, 1996). Usually, TRLS is performed by using laser sources with a large range of wavelength tunability and pulse duration and energy.

As for TRCL spectroscopy and imaging, at least two experimental approaches have been developed. After the pioneering work by Bimberg *et al.* (1985), several groups used a beam blanker system on the SEM column, with time resolutions ranging from 10 ns to 100 ps (see, e.g., Khatsevich *et al.* (2007) and references therein enclosed). More recently, Merano *et al.* (2005) have replaced the classical hairpin tungsten electron gun of a commercial SEM with a 20-nm-thick gold photocathode deposited on a quartz plate. By illuminating the photocathode by a ultraviolet mode-locked laser (266 nm, 200 fs, 80.7 MHz of repetition rate), they generated an ultrafast pulsed electron beam. A streak camera mounted behind a monochromator was then used as a time-resolved detector. It is worth noting that, contrary to the beam blanker-based systems, this solution is not yet commercially available.

In the following, an example of the application of the method proposed by Merano *et al.* (2005) on group-III nitrides will be reviewed.

WZ group-III nitrides are nowadays the materials of choice for optoelectronic devices emitting visible–UV light. However, as already mentioned, the presence of the quantum-confined Stark effect, that is, the decreasing of the overlap between the electron and hole wave functions due to the onset of huge built-in electric fields, affects the ratio between radiative and nonradiative processes in heterostructures grown along the *c*-axis. One of the ways to overcome this problem is to grow heterostructures oriented along the *a*-axis, a nonpolar direction perpendicular to the *c*-axis. This solution increases the radiative efficiency of the devices. However, the growth of high-quality

a-plane GaN is still far to be achieved, and large densities of extended defects such as different kinds of basal stacking faults (BSFs) are found.

The paper reviewed by Corfdir *et al.* (2009) deals with the use of low-temperature picosecond TRCL technique to investigate in detail the mechanisms of exciton relaxation and recombination involving BSFs in an *a*-plane GaN epilayer grown by the epitaxial lateral overgrowth (ELO) method. Briefly, the ELO technique is a local epitaxial growth which initially occurs in the direction normal to the surface of the substrate but then proceeds preferentially in the direction parallel to the surface of the substrate. With this technique, regions presenting reduced densities of extended defects can be obtained in the epilayer.

The authors show that the BSFs exhibit two types of spatial distributions. In the regions where they are diluted, the relaxation of excitons toward them, for $T = 27$ K, involves the donors via a kind of hopping process. In the regions where they are concentrated into bundles, the exciton relaxation is much faster, although not instantaneous, which they tentatively ascribe to intra-BSF localization processes. The decay dynamics of the BSF CL was also found to be different, depending on whether the excitation region has a small or high density of BSFs, which may indirectly confirm the type-II band alignment expected for I_1-BSFs in GaN.

CL investigations from the literature on ELO *a*-plane GaN showed that I_1-type BSFs tend to gather into dense bundles, evidencing position-dependent morphologies. In a previous paper the authors have shown that I_1-type BSFs evidence intense CL stripes with a characteristic photon energy of 3.417 eV (see **Figure 23(b)**). The stripes are typically several tens of micrometers long, and correspond to the emergence of high densities of BSF planes (some $10^6\,\mathrm{cm}^{-1}$) which propagate vertically from the interface. Moving the e-beam away from those bundles, the CL signal intensity peaked at 3.417 eV decreased and that was ascribed to a local much lower density of BSFs, rather than to an efficient exciton transfer from the excitation spot toward the bundles.

To verify this observation, in this work, dynamical measurements performed by picosecond-time-resolved CL (pTRCL) have been carried out. pTRCL allowed to benefit from both strong spatial and temporal resolutions not achievable by time-resolved PL.

Figure 23(a) shows time-integrated CL spectra of the sample investigated. The emission lines at 3.471 and 3.417 eV are assigned to donor-bound exciton A (D°X) and to BSF-bound exciton, respectively. **Figure 23(b)** shows top-view time-integrated CL map of our ELO GaN epilayer at $T = 27$ K, taken at the luminescence energy of I_1-BSFs. On this image, bright bundles and diluted zones are distinct in the $+c$ wings. In the diluted zones, the CL

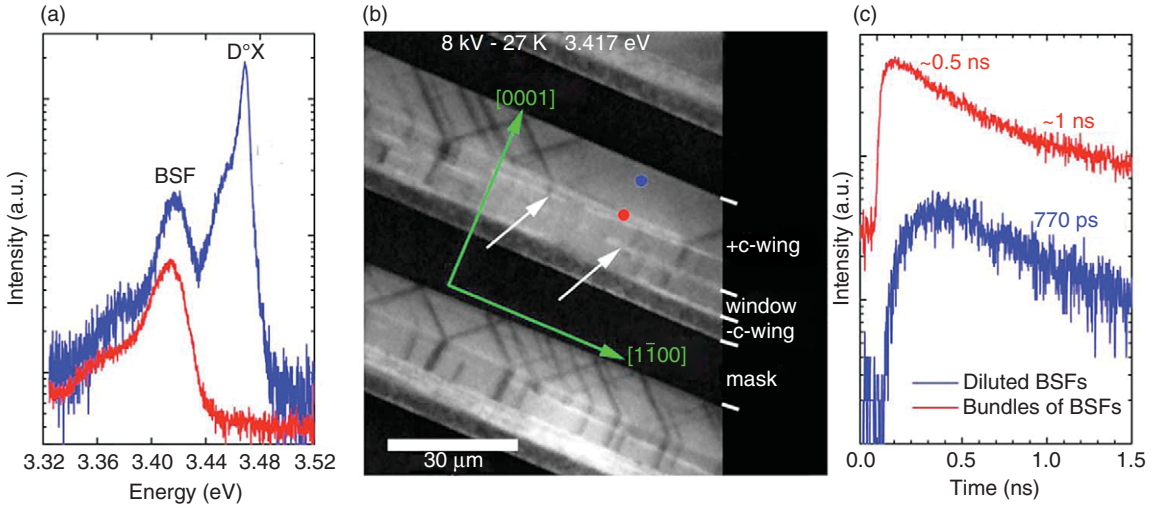

Figure 23 Blue (respectively red) curves correspond to excitation away from (respectively on) bundles of BSFs, as shown in (b) by a blue (respectively red) dot. (a) Time-integrated CL spectra (upper curve is blue). (b) top-view CL map taken at 3.417 eV. White arrows point out the emergence of bundles of BSFs. (c) Time decays of the 3.417 eV CL signal (upper curve is red). From Merano M, Sonderegger S, Crottini A, *et al*. (2005) Probing carrier dynamics in nanostructures by picosecond cathodoluminescence. *Nature* 438(7076): 479–482.

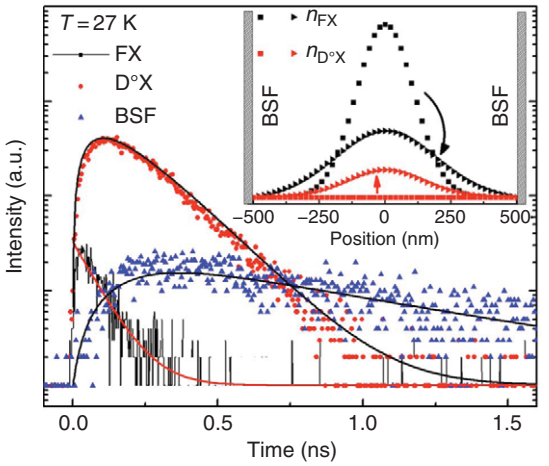

Figure 24 Luminescence decays of FX, D°X, and BSF excitons when excitation is on diluted regions. Solid lines are the result of the diffusion model. The latter is sketched in the inset showing the calculated spatial distributions of FX and D°X (black and red symbols, respectively) at $t = 0$ and $t = 50$ ps (squares and triangles). From Merano M, Sonderegger S, Crottini A, *et al*. (2005) Probing carrier dynamics in nanostructures by picosecond cathodoluminescence. *Nature* 438(7076): 479–482.

spectrum and dynamics (**Figures 23(a) and 23(c)**) remain absolutely unchanged when the distance between the excitation spot and the nearest bundle changes from a few hundred nanometers to several micrometers.

In those regions (**Figure 24**), the FX line decays exponentially with a time constant of 85 ps, which corresponds to the rise time of the D°X luminescence. The mechanism that limits the FX lifetime therefore involves their capture by donors. Further, the D°X line decays exponentially with a time constant of 135 ps. More surprising, the BSF CL, which decays exponentially with a time constant of 770 ps, exhibits a very slow rising (the maximum intensity is reached ~300 ps after the excitation). *A priori*, one would expect the BSFs either to be directly populated by the excitation pulse or to capture free excitons by a scattering process. In both cases, given the measured decay time for free excitons, the BSF rise time should not exceed a few tens of picoseconds, in contrast with observation. The mechanism by which the BSFs trap excitons is therefore more complex, although it necessarily involves the diffusion of excitons.

To explain the mechanisms on the basis of the experimental TRCL results, the authors have developed a one-dimensional diffusion model for excitons along the c-axis, that is, perpendicular to the BSF planes, sketched in the inset of **Figure 24**. The description of the model is beyond the scope of this chapter and the reader is referred to the original paper for a complete discussion.

In synthesis, the following assumptions were made:

1. the distance between two adiacent BSFs was 1 μm;
2. a Gaussian distribution of FX following the pulsed electron beam excitation at $t = 0$ along the c-axis is supposed;
3. BSFs instantaneously trap FX in their vicinity; and
4. BSF-bound excitons recombine radiatively.

The inset in **Figure 24** illustrates the modeled time dependence of the FX and D°X density profiles. Note that the D°X distribution after a few tens of picoseconds is quite similar to the initial distribution of FX.

Since the BSFs would receive a very small amount of excitons with a short time constant, in order to fit the observed long rise time for the BSF signal, the thermally assisted reemission of excitons from the donors, τ_{ESC}, must be introduced. As a result, the best fit to the experimental results yields $\tau_{ESC} = 600$ ps, $\tau_{D°X} = 140$ ps, and $\tau_{BSF} = 770$ ps and capture time of FXs onto neutral donors $\tau_C = 150$ ps. The $\tau_{D°X}$ and τ_{BSF} values are close to the measured CL decay times and they are therefore determined with an excellent accuracy.

The same comment holds for τ_C which controls both the decay rate of FX and the rise rate of the D°X transition. Concerning the role played by donors in the diffusion process, it is necessary that the escape time τ_{ESC} is neither independent of the inter-BSF distance, nor of the fixed diffusion coefficient (D_{FX}). Nevertheless, whatever the values set for D_{FX} or for the inter-BSF distance, it is absolutely necessary to include the thermally assisted escape of excitons from donors in order to fit the fast decay of FX, and both the fast and slow CL rise times of D°X and BSFs. This demonstrates that, for $T = 27$ K, the excitons that are created in the diluted regions diffuse toward the BSFs via the donors, by a kind of hopping process.

The lifetimes of free- and donor-bound excitons should be dramatically short when several BSFs are simultaneously excited, that is, they are ~10 nm away from each other, only three times the donor (or exciton) Bohr radius, and smaller by a factor of 1.4 than the characteristic diameter of the D°X complex.

This is confirmed by the experimental results shown in **Figure 23(a)**. Only the BSF-related line at 3.417 eV is observed with a rise time much shorter

than the one observed in the diluted regions (Figure 23(c)). However, since the maximum intensity is reached after ~110 ps, it means that the maximum population of BSF excitons is not established instantaneously. The authors tentatively relate this observation to slow relaxation mechanisms of BSF-bound excitons toward deep potential fluctuations inside BSFs themselves.

The decay dynamics of the BSF-related CL are clearly different when excitons are created on or away from the bundles (Figure 23(c)). This suggests that, in the bundles, the different overlap of electron and hole wave functions is correlated to the distribution of inter-BSF distances. This variety may be an indirect proof of the type-II band alignment for the BSFs, the large presence probability of the hole in the WZ GaN barriers yielding a diversity of inter-BSF coupling schemes.

4.10.6 EBIC Characterization of Extended Defects

Extended defects, such as dislocations, stacking faults (SFs), and grain boundaries (GBs), are commonly known as recombination centers, and may reduce the carrier lifetime and degrade the semiconductor devices. EBIC is an important method and has extensively been applied to study the defect behavior in the last decades.

Figure 25 shows the schematic of EBIC characterization of extended defects. This is an example of planar EBIC with the Schottky contact. The collected EBIC current at a defect I_D is generally lower than that at the background I_B. Therefore, the defects can be found as dark features in EBIC images. For quantitative investigation, the electrical activity (recombination strength) of a defect is estimated from its EBIC contrast, which is defined by

$$C = \frac{I_B - I_D}{I_B} \times 100\,(\%) \tag{6}$$

In Equation (6), if a defect has high EBIC contrast, it means that the defect is electrically active or its recombination strength is high. As typical examples of this technique, characterization of extended defects in Si, SiC, GaN, and ZnO will be demonstrated.

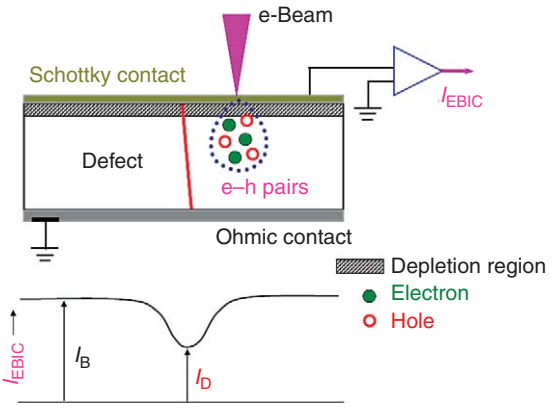

Figure 25 Schematic of EBIC characterization of extended defects in semiconductors.

4.10.6.1 Extended Defects in Si

Some typical examples for dislocations and GBs in silicon are given in the following.

In as-grown (regarded as clean) sample, no obvious contrasts of dislocations could be observed by EBIC at RT. After low Cu contamination (ppb range), the EBIC micrographs (Kittler *et al.*, 1995) taken in the same area are shown in Figure 26. At 300 K, two dark lines are seen, with the numbers indicating their contrast values. Those dark lines are related to misfit dislocations (MDs). At 80 K, additional dark lines are visible. For example, the dislocation with no contrast at 300 K is seen with a contrast of 2.5% at 80 K. It indicates that this dislocation is only electrically active at low temperatures and is accompanied by shallow levels according to the SRH statistics.

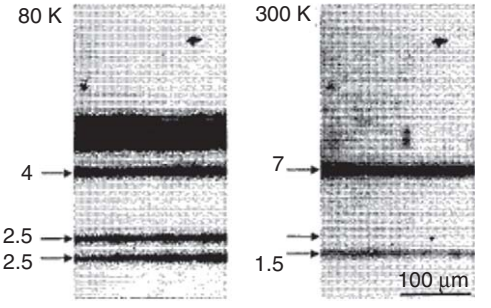

Figure 26 EBIC images of misfit dislocations taken at 80 and 300 K. The numbers indicate the EBIC contrast values. From Kittler M, Ulhaq-Bouillet C, and Higgs V (1995) Influence of copper contamination on recombination activity of misfit dislocations in SiGe/Si epilayers: Temperature dependence of activity as a marker characterizing the contamination level. *Journal of Applied Physics* 78: 4573–4583.

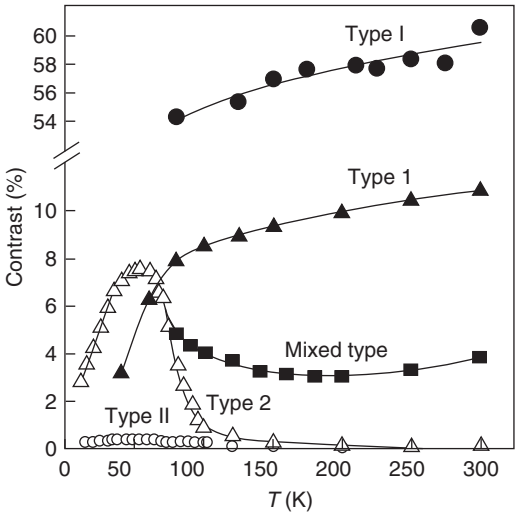

Figure 27 Temperature-dependent EBIC contrasts of dislocations with different amounts of contamination. Change of contrast type follows the sequence with an increase in contamination: II (clean) → 2 → mixed → 1 → I. From Knobloch K, Kittler M, and Seifert W (2003) Influence of contamination on the dislocation-related deep level C1 line observed in deep-level-transient spectroscopy of n-type silicon: A comparison with the technique of electron-beam-induced current. *Journal of Applied Physics* 93: 1069–1074.

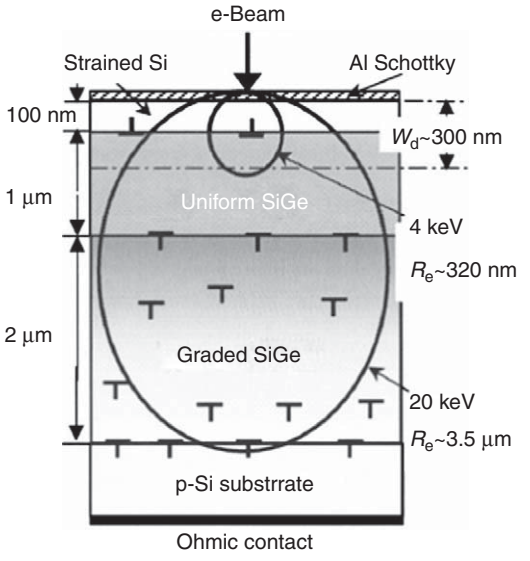

Figure 28 Schematic diagram of sample structure used for EBIC characterization. From Yuan XL, Sekiguchi T, Ri SG, and Ito S (2004) Detection of misfit dislocations at interface of strained $Si/Si_{0.8}Ge_{0.2}$ by electron-beam-induced current technique. *Applied Physics Letters* 84: 3316–3318.

The temperature behavior of EBIC contrast *C(T)* in dislocations has been systematically studied by Knobloch *et al.* (2003) and Kittler *et al.* (2003), as shown in **Figure 27**. The *C(T)* behavior represents a fingerprint characterizing the degree of contamination of the dislocations. Clean dislocations exhibit very weak activity (type II), with a maximum at ~50 K, and untraceable activity at RT. Low contamination (10^4–10^5 impurities per cm) results in an increase of the low-temperature activity, still leaving the RT activity below the detection limit (type 2). Upon a further increase in contamination (10^6 impurities per cm or more), the EBIC contrasts of the dislocations increase with the increase in temperature (type 1). For mixed-type behavior, the number of impurities is between those of type 1 and 2. When the dislocations are decorated with metal silicide precipitates, they show very strong activity throughout the whole temperature range (type I). Roughly, clean or low contaminated dislocations are accompanied by shallow levels, whereas in medium or high contamination case, they are decorated by deep levels.

Strained Si/SiGe heterostructures offer the opportunity to overcome the limit of Si metal-oxide-semiconductor field-effect transistor (MOSFET) devices due to enhanced carrier mobility. Controlling the extended defects existing in the strained Si layer is a key issue for the practical application. The MDs at the interface of strained Si/SiGe are significant scattering source to limit the carrier mobility (Ismail *et al.*, 1994). Threading dislocations (TDs) terminated to the surface of strained Si may cause high leakage current (Giovane *et al.*, 2001). Thus, investigation of defects in upper strained Si and deep interface is important from both technological and scientific point of view.

Figure 28 shows the schematic illustration of the sample structure and geometry of the EBIC method (Yuan *et al.*, 2004). The specimen consists of three layers: a 2-μm step-graded $Si_{1-x}Ge_x$ layer was grown on the Si substrate, reaching a 20% Ge composition; a 1-μm relaxed uniform $Si_{0.8}Ge_{0.2}$ buffer layer was grown on the graded SiGe layer; a strained 100-nm Si layer was grown on the uniform SiGe layer. All the layers were doped by B with a concentration of $1 \times 10^{16}\,cm^{-3}$. Depth-dependent EBIC was then performed to investigate the dislocations in this specimen.

The EBIC micrographs (Yuan *et al.*, 2004) taken at 65 K are shown in **Figure 29**. To detect the dislocations in the upper region, a low-energy e-beam of 4 kV was used. The electron range R_e at

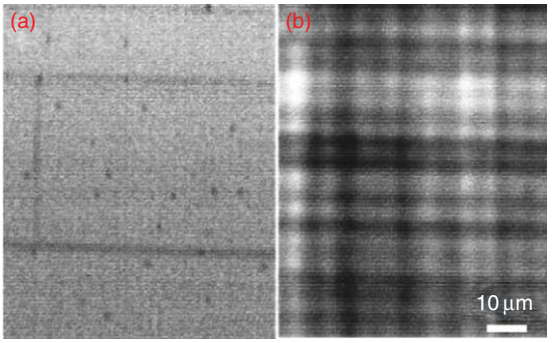

Figure 29 EBIC images taken at 4 (a) and 20 kV (b) at a temperature of 65 K. From Yuan XL, Sekiguchi T, Ri SG, and Ito S (2004) Detection of misfit dislocations at interface of strained Si/$Si_{0.8}Ge_{0.2}$ by electron-beam-induced current technique. *Applied Physics Letters* 84: 3316–3318.

4 kV is calculated to be only ~320 nm. It means that the volume of generated carriers contains the upper interface but not the deeper SiGe graded region. In **Figure 29(a)**, two orthogonal sets of dark lines and some dark dots were observed. The dark lines are oriented along <110> directions, corresponding to MDs in the interface. The dark dots are related to the TDs. The average EBIC contrast of those dislocations is about 0.8%. With an e-beam of 20 kV ($R_e \sim 3.5$ μm), a pattern of dense orthogonal dark lines (EBIC contrast ~10%) was observed in **Figure 29(b)**. They are attributed to the cross-hatch pattern of the MDs network in the graded SiGe layer. In this condition, however, no TDs were clearly seen, since the weak contrasts of TDs are masked by the strong contrasts of dense MDs in the graded region. The detection of the dislocations within the depletion region (**Figure 29(a)**) is an important experimental accomplishment: even the drift motion is dominant, a small fraction of carriers may be recombined at the localized states of dislocations, which results in a weak EBIC contrast.

Multi-crystalline Si (mc-Si) is the most widely used material for solar cell production. The disadvantage of mc-Si is the existence of electrically active GBs. Impurities (e.g., Fe) gettered by the GBs act as recombination centers and thus reduce the conversion efficiency of solar cells. Chen *et al.* (2004, 2005a, 2005b, 2007) have systematically investigated the electrical activities of various GBs in mc-Si. Typical examples are shown here.

Figure 30 presents SE, EBSD, and EBIC images of GBs in different areas of clean mc-Si samples (Chen *et al.*, 2007). The large-angle (LA) GBs are seen as bumps or grooves in the SE, owing to the etching. The types of GBs are distinguished by the EBSD patterns, where Σ3, Σ9, Σ27, random (R), and small-angle (SA) GBs are illustrated. In the EBIC images at 300 K, no obvious GB contrast was observed except R- and SA-GBs. The EBIC images at 100 K show faint contrast of GBs except SA-GBs (denoted as SA1 and SA2). Additional dark patterns are also seen inside the grains, which are related to dislocations or other defects. Statistical EBIC contrasts of GBs have shown that, in the clean mc-Si, the EBIC contrasts of Σ3, Σ9, Σ27, and R at 300 K are less than 1.5%, while those at 100 K vary from 1.5% to 3.8%. On the other hand, the EBIC contrasts of SA-GBs at 300 K vary from 1% to 8%. At 100 K, the EBIC contrasts of SA-GBs significantly increase in the range from 16% to 45%. All the GBs exhibit weak EBIC contrasts at 300 K, suggesting that they incorporate shallow levels.

To check impurity gettering effect of GBs, intentional Fe contamination was conducted in mc-Si. **Figure 31** shows the SE, EBSD, and EBIC images of Fe contaminated samples with three different contamination levels (Chen *et al.*, 2007). The left, center, and right columns correspond to the low, medium, and heavy contaminated mc-Si. In the EBIC images, the GBs are clearly distinguished as dark lines. Even in the low contaminated mc-Si, some of the GBs can also be seen at 300 K. R, Σ27, and Σ9 are easily distinguished rather than Σ3. At 100 K, all GBs are clearly seen in EBIC image due to the increase of contrasts. The medium contaminated mc-Si shows similar EBIC behavior as the low contaminated one but higher EBIC contrast. However, when the contamination level becomes high, the EBIC behavior is different from the former two cases. All the GBs are clearly seen at 300 K (dark dots also appear inside the grains), while their EBIC contrasts become lower at 100 K. This indicates that deep levels are dominant for heavy contaminated GBs. It should be noted that denuded zones along GBs are now visible at 100 K.

A classification table (Chen *et al.*, 2007) of the EBIC contrasts of GBs (300 K) with respect to GB character and contamination level is shown in **Figure 32**. The amount of contamination is categorized into four levels: clean, light (annealing at 800 °C), medium (900–1000 °C), and heavy (1100 °C). In the clean mc-Si, the EBIC contrasts of SA-GBs vary from 0% to 30%, while those of LA-GBs are less than 2%. In the Fe-contaminated mc-Si, the EBIC contrasts of both SA- and LA-GBs increase. At each contamination level, SA-GBs (except SA < 1°) always present

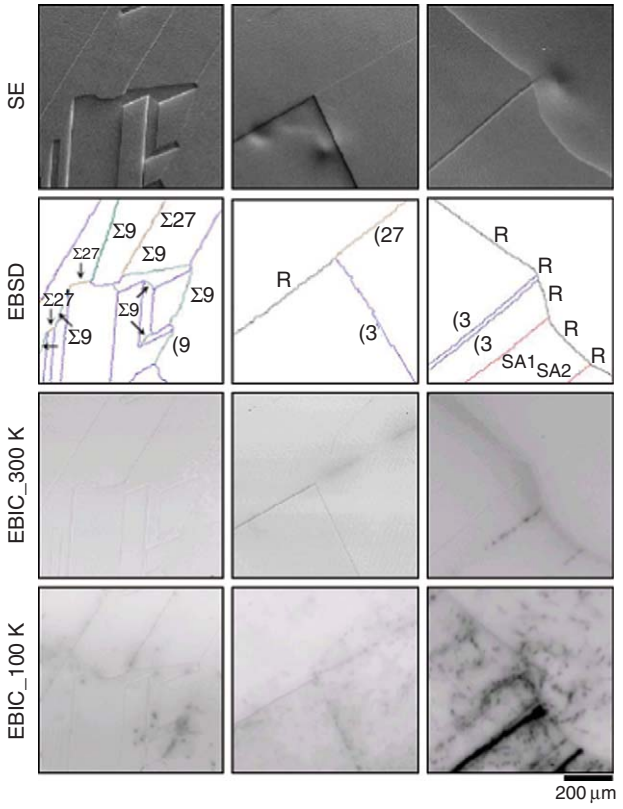

Figure 30 SE, EBSD, and EBIC images of GBs in clean mc-Si. Unmarked GBs in EBSD are Σ3. From Chen J, Sekiguchi T, and Yang D (2007) Electron-beam-induced current study of grain boundaries in multicrystalline Si. *Physica Status Solidi (c)* 4: 2908–2917.

higher EBIC contrasts than LA-GBs, indicating that the SA-GBs are more effective gettering sites for Fe atoms. The high-density dislocations at SA-GBs may act as gettering sites. As for the LA-GBs, it evidently shows the high-Σ GBs are easily contaminated with Fe so that they give stronger EBIC contrast. Thus, the impurity gettering abilities of GBs in mc-Si follow in the order of SA > R > high-Σ > low-Σ.

4.10.6.2 Extended Defects in SiC

SiC is a good wide-band-gap semiconductor suitable for fabricating high-power, high-temperature, and high-frequency devices. Among various polytypes, 4H-SiC ($E_g \sim 3.2$ eV) has great potential for manufacturing high-voltage devices, owing to its high bulk mobility and small anisotropy. Recent advances in 4H-SiC homoepitaxy make it possible to eliminate large crystalline defects. However, dislocations or SFs still exist in current devices. Characterization of those defects may provide hints for further improvement of devices.

Figure 33 presents an EBIC image at 300 K (a) of the 4H-SiC epilayer and an optical micrograph (b) of the same region after KOH etching (Chen et al., 2008a). Some dark lines and dots distribute randomly in **Figure 33(a)**. The dark lines (marked D) are aligned along $< 11\bar{2}0 >$ direction, and their EBIC contrast is ~18%. The dark dots marked A, B, and C show different EBIC contrasts, which are about 12%, 10%, and 8%, respectively. This indicates that their types may differ. In **Figure 33(b)**, etch pits show different shapes and sizes, and they locate exactly at the same positions as dark lines and dots observed in the EBIC image. Four types of dislocations are identified according to the morphology of etch pits proposed by Takahashi *et al.* (1994). The oval etch pits are related to basal plane dislocations (BPDs), corresponding to the dark lines in the EBIC image. Large and dark etch pits with a bright spot in the center are related to screw dislocations (marked A). Two kinds of edge dislocations are distinguished, namely, edge-I (small dark etch pits, marked B) and edge-II (small

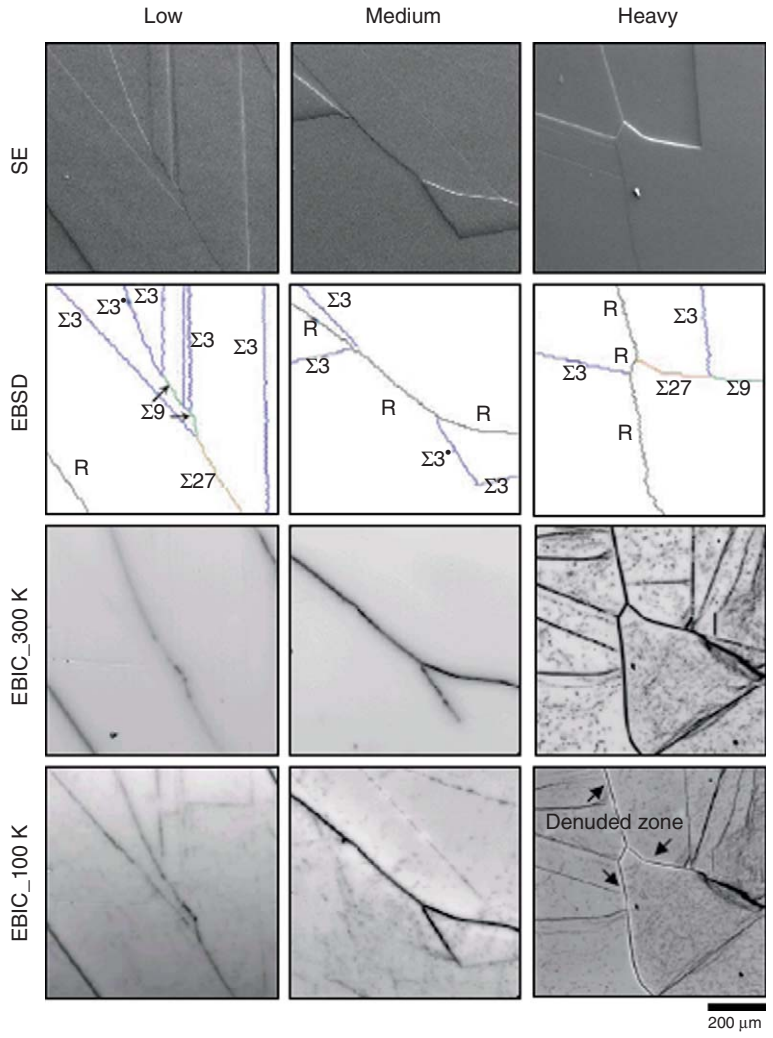

Figure 31 SE, EBSD, and EBIC images of GBs in mc-Si with low, medium, and heavy contamination of Fe. From Chen J, Sekiguchi T, and Yang D (2007) Electron-beam-induced current study of grain boundaries in multicrystalline Si. *Physica Status Solidi (c)* 4: 2908–2917.

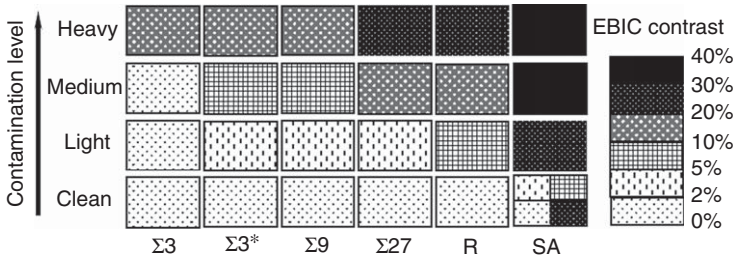

Figure 32 EBIC contrasts of various GBs at 300 K with respect to GB type and contamination level (Σ3−Σ3{111},Σ3*−Σ3 with other planes). From Chen J, Sekiguchi T, and Yang D (2007) Electron-beam-induced current study of grain boundaries in multicrystalline Si. *Physica Status Solidi (c)* 4: 2908–2917.

bright etch pits, marked C). The screw and edge dislocations appear as dark dots in the EBIC image, indicating that they are TDs.

Temperature-dependent electrical activities of those dislocations (Chen *et al.*, 2008a) are shown in **Figure 34**. The EBIC contrasts of BPDs increase

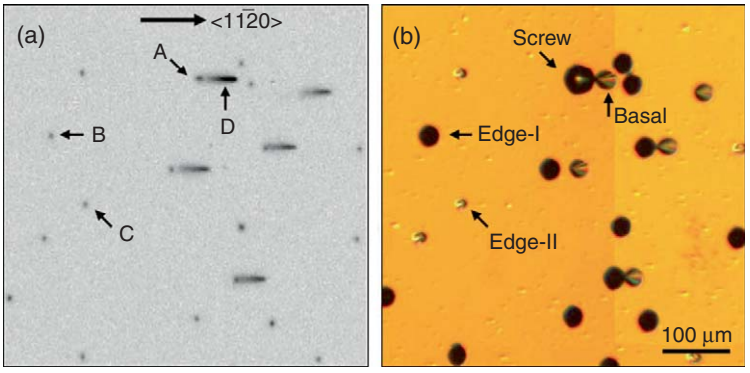

Figure 33 Dislocations revealed by EBIC and KOH etching: (a) EBIC imaging of dislocations and (b) optical micrograph of etch pits after KOH etching. From Chen B, Chen J, Sekiguchi T, *et al*. (2008a) Electron-beam-induced current study of electrical activity of dislocations in 4H-SiC homoepitaxial film. *Journal of Materials Science: Materials in Electronics* 19: 5219–5223.

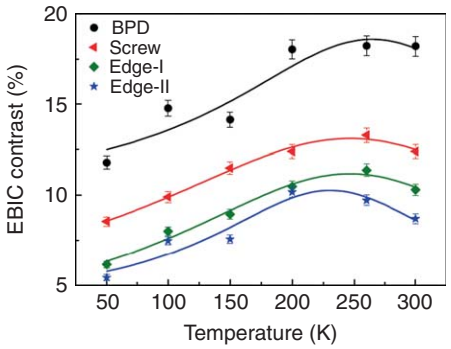

Figure 34 Temperature dependence of EBIC contrasts of dislocations in 4H-SiC. From Chen B, Chen J, Sekiguchi T, *et al*. (2008a) Electron-beam-induced current study of electrical activity of dislocations in 4H-SiC homoepitaxial film. *Journal of Materials Science: Materials in Electronics* 19: 5219–5223.

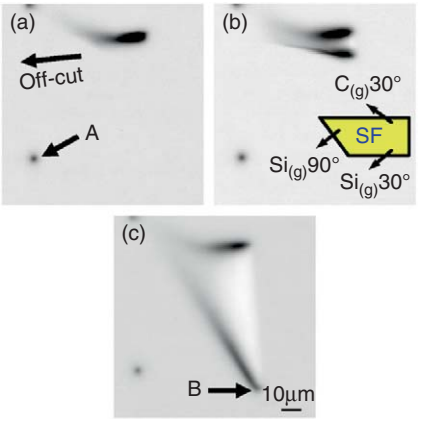

Figure 35 EBIC imaging of the dissociation of a BPD in 4H-SiC under e-beam irradiation: (a) initial BPD; (b) 20 min irradiation; and (c) 100 min irradiation. From Chen B, Chen J, Sekiguchi T, *et al*. (2008b) Electron-beam-induced current study of stacking faults and partial dislocations in 4H-SiC Schottky diode. *Applied Physics Letters* 93: 033514.

from ~12% to ~18% by increasing temperature, reach the maximum at around 250 K, and then decrease slightly to RT. The EBIC contrasts of TDs are 8–12% for screw dislocation, 6 to 10% for edge-I, and 6–8% for edge-II dislocations, which show a similar behavior as the temperature increases. The EBIC contrasts increasing with temperature suggest that the dislocations are accompanied by deep levels. This behavior is different from that of clean dislocations and GBs (shallow levels) in Si described in the preceeding section. Furthermore, at each temperature, the EBIC contrast of dislocations is higher in the sequence of BPD > screw > edge-I > edge-II. From the recombination point of view, the EBIC results suggest that BPD is the most harmful dislocations in 4H-SiC.

EBIC is also a useful technique for the *in situ* study of the dislocation motion or reaction (Chen *et al*., 2008b, 2009). **Figure 35** shows the EBIC images depicting the dissociation of a BPD in 4H-SiC under e-beam irradiation (Chen *et al*. 2008b). In the initial state, there is a dark line and a dark dot (marked A) in **Figure 35(a)**. The dark line corresponds to a BPD with dislocation line toward the $< 11\bar{2}0 >$ direction in the (0001) plane, while the dark dot is related to a TD with dislocation line nearly perpendicular to the surface. The BPD intersects the surface at the right end. The EBIC contrasts of the BPD and TD are $33 \pm 3\%$ and $13 \pm 2\%$, respectively. After e-beam irradiation for 20 min

(Figure 35(b)), the BPD was dissociated into partial dislocations. The Burgers vector reaction for the dissociation is given by

$$1/3[11\bar{2}0] = 1/3[10\bar{1}0] + 1/3[01\bar{1}0] \quad (7)$$

and an SF is formed inside the partial dislocation loop (PDL).

It has to be noticed that one partial dislocation nearly stays at the same position as the initial BPD, whereas the other moves during the irradiation, resulting in the expansion of the SF. The leading partial has a $Si_{(g)}$ core, while the trailing one has a $C_{(g)}$ core (Pirouz *et al.*, 2001; Ha *et al.*, 2003). The schematic diagram of the dissociation of BPD is shown in Figure 35(b). The EBIC contrasts of $Si_{(g)}$ 30° and $C_{(g)}$ 30° partials are $19 \pm 2\%$ and $23 \pm 2\%$, which are much lower than that of the BPD. Figure 35(c) presents the final state of the dissociation of BPD under a 100 min e-beam irradiation. The $Si_{(g)}$ 30° partial continues to move and finally appears as a very short segment (marked B). It is interesting to note that the SF shows peculiar bright contrast in the EBIC images. Such behavior is highlighted in a three-dimensional EBIC contrast profile (Chen *et al.*, 2008b), as shown in Figure 36. The SF presents negative EBIC contrast (~-4%), corresponding to the bright region in the EBIC images.

According to the CL results of Chen *et al.* (2008b) and the theoretical study of Iwata *et al.* (2003), it is suggested that the SF introduces a quantum well, whose energy is 0.25 eV lower than the conduction band minimum of 4H-SiC. A model was proposed by Chen *et al.* (2008b) to explain the bright SF in the EBIC images, as shown in Figure 37. The figure is a cross-sectional view of the sample structure for EBIC

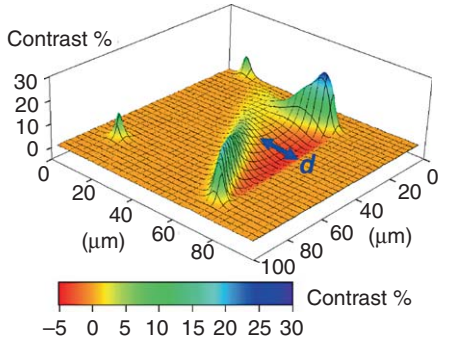

Figure 36 A three-dimensional EBIC contrast output of Figure 35(c). From Chen B, Chen J, Sekiguchi T, *et al*. (2008b) Electron-beam-induced current study of stacking faults and partial dislocations in 4H-SiC Schottky diode. *Applied Physics Letters* 93: 033514.

measurement. The SF lies in the basal plane, which is 8°off the surface. Since this is an n-type 4H-SiC, minority carriers (holes) generated by an electron beam are collected as the EBIC signals. In the equilibrium state, the electron density in the specimen is represented as n_0. During e-beam irradiation, the densities of generated electrons and holes in the excitation volume are Δn and Δp, with $\Delta n = \Delta p$. When the e-beam scans the background, the total electron density in the volume becomes $n_0 + \Delta n$. At the SF, however, considerable fraction of generated electrons is captured by the SF due to its QW state. Those electrons diffuse away along the SF. Thus, the electron density in the generation volume decreases to $n_0 + \Delta n - \delta_n$, where $\delta_n$is the electron density that diffuses away. Due to this reduction, the lifetime of holes in the volume may increase. As a result, the collected EBIC current at SF is higher than that at the background, leading to the bright SF.

4.10.6.3 Extended Defects in Other Semicondutors

GaN (III–V group, $E_g \sim 3.3$ eV) is an important wide-band-gap semiconductor for blue LEDs and lasers, etc. Due to lack of lattice-matched substrates, high density of defects are usually present in GaN films. The wide application of GaN devices has attracted an increasing interest in the study of recombination properties of the existing defects.

Figure 38 shows the EBIC investigation of extended defects in epitaxial lateral overgrown (ELOG) GaN film by metal-organic chemical vapor deposition (MOCVD) (Yakimov *et al.*, 2007). The initial GaN template was 2 μm thick, with the width of SiO_2 stripes 12 μm and the width of mask windows 4 μm. A 12-μm-thick ELOG film was grown over this mask. In the EBIC image (Figure 38(a)), the dark spots with submicron diameter are related to TDs. Three well-defined regions are observed: (1) a region with a high density of $\sim 10^8$ cm^{-2} defects corresponding to the windows in SiO_2 mask; (2) a laterally overgrown region (wing region) with a density of $\sim 5 \times 10^6$ cm^{-2}; and (3) a region in the middle of the laterally overgrown area (wing merger region) where the defect density is $\sim 10^8$ cm^{-2}. This confirms that the defect density in GaN films can be decreased by using ELOG technique.

An EBIC line scan was performed across the stripes, as shown in Figure 38(b). At 10 kV, the EBIC signal is low in the windows, high in the wings, and again low in the wing merger regions. By

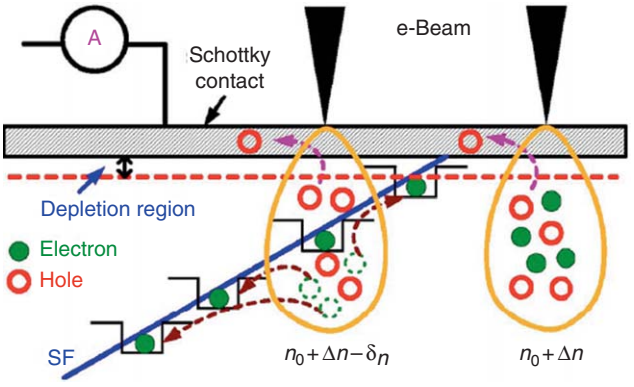

Figure 37 A model to explain the bright contrast of SFs in the EBIC images. From Chen B, Chen J, Sekiguchi T, *et al*. (2008b) Electron-beam-induced current study of stacking faults and partial dislocations in 4H-SiC Schottky diode. *Applied Physics Letters* 93: 033514.

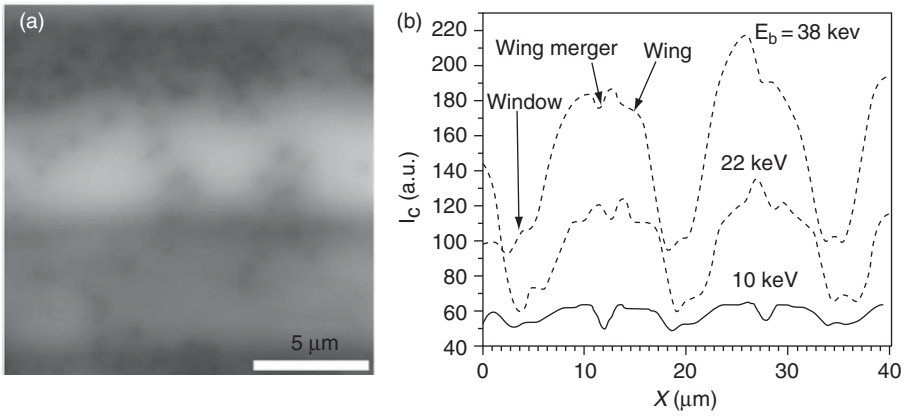

Figure 38 (a) EBIC imaging of the GaN ELOG specimen, (b) EBIC signal profile obtained by scanning across the ELOG stripes. From Yakimov EB, Vergeles PS, Polyakov AY, *et al*. (2007) Spatial variations of doping and lifetime in epitaxial laterally overgrown GaN. *Applied Physics Letters* 90: 152114.

increasing the accelerating voltage, depth-resolved information revealed that a fine structure appears in the wing merger region. This is probably due to the band bending caused by dislocations in that region. Furthermore, as the accelerating voltage increases, the EBIC signal in the window region does not change so much, while that in the wing region significantly increases. This indicates that the donor concentration is higher in the window compared to the wing region, resulting in the shorter diffusion length in the window region.

Remote EBIC (REBIC) is applicable to study the extended defects in semiconductors with high resistivity. In REBIC, the samples do not necessarily contain p–n junctions or Schottky barriers, but two ohmic contacts are needed on either side the area being investigated. The generated e–h pairs by e-beam irradiation are divided by the space-charge region of charged boundaries (due to local band bending), and then are collected as the EBIC signals for the imaging.

Figure 39 shows an REBIC study (Zaldivar *et al*., 2001) of growth hillocks on GaN epitaxial films. A bright-dark contrast is seen in the border of hillock (Figure 39b). Such contrast is commonly known as peak and trough (PAT) and has been observed in REBIC studies of GBs in semiconductors (Holt *et al*., 1996; Russell *et al*., 1996). In addition to the bright region in the border, a bright spot and a star-shaped pattern with light contrast was also observed in the center of hillock. It suggests that the dopant impurities or point defects are not homogeneously distributed at the hillocks, which is responsible for the charge effects detected by the REBIC imaging.

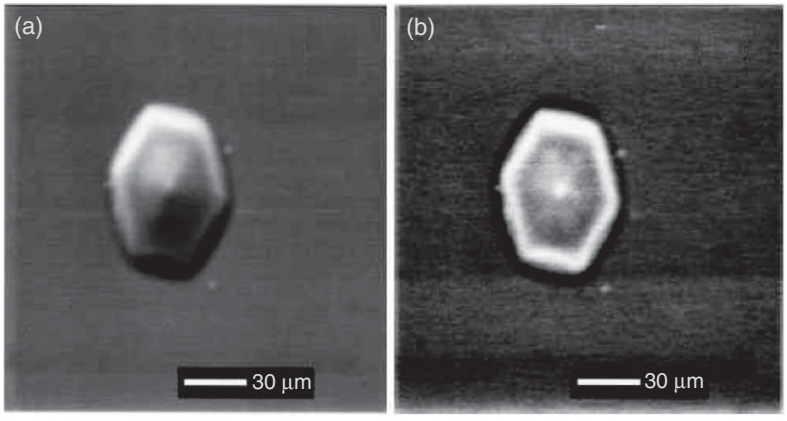

Figure 39 Emissive mode (a) and REBIC image (b) of a pyramidal hillock at RT. From Herrera Zaldivar M, Fernández P, and Piqueras J (2001) Study of growth hillocks in GaN:Si films by electron beam induced current imaging. *Journal of Applied Physics* 90: 1058–1060.

ZnO (II–VI group, $E_g \sim 3.3\,\text{eV}$) has attracted much attention for optoelectronic device applications. REBIC characterization of GBs in ZnO is described. The examples shown here also demonstrate the application of bias-dependent REBIC study to extended defects.

Figure 40 shows REBIC imaging of bright and dark GBs in ZnO with and without bias (Leach, 2001). Generally, bright–dark contrast (also termed as PAT) appears at GBs in cubic materials (Holt *et al.*, 1996; Russell *et al.*, 1980), since the opposed fields on either side of a symmetrical charged GB generate EBIC currents in opposite directions. However, it is frequently the case for ZnO (hexagonal) that the EBIC signal is suppressed on one side of the GB leaving only a single bright

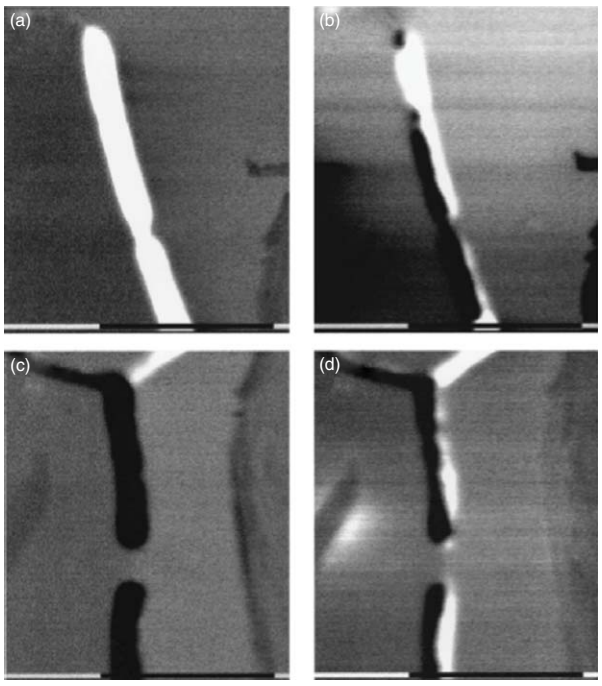

Figure 40 (a, b) REBIC images of bright GBs in ZnO with (a) zero and (b) −90 mV bias applied; (c, d) REBIC images of dark GBs in ZnO with (c) zero and (d) +50 mV bias applied (scale bars = 10 μm). From Leach C (2001) Crystal plane influence of the EBIC contrast in zinc oxide varistors. *Journal of the European Ceramic Society* 21: 2127–2130.

(**Figure 40(a)**) or dark (**Figure 40(c)**) line. Whether the REBIC appears solely bright or dark in the image depends on the charged type of a GB (positive or negative). After applying the negative/positive bias, the bright or dark contrast of the GBs changes to the common bright–dark contrast, as seen in **Figures 40(b)** and **40(d)**. It suggests that the asymmetrical field of charged GBs in ZnO modifies into the symmetrical field that is common in cubic systems.

Also, a small portion of GBs in ZnO exhibits initially bright–dark contrast (Leach, 2001), as illustrated in **Figure 41**. In a zero bias (**Figure 41(a)**), the GB shows characteristic bright–dark contrast. Upon applying a positive bias to the right-hand electrode, the electrostatic barrier height on the right-hand, reverse-biased, side of the GB is increased, and on the left-hand, forward-biased, side of the GB is decreased. When a voltage of +40 mV was applied (**Figure 41(b)**), the bands on the left-hand side of the GB become flatter. Therefore, the left dark EBIC contrast is lost due to the suppression of the charge separating field, giving rise to the bright contrast of GB. Similarly, the flat band condition is achieved on the right-hand side of the GB by applying –40 mV bias. In this way, a dark GB was observed (**Figure 41(c)**).

Both solely bright/dark GBs and dark/bright GBs are present in the same ZnO sample, which suggests that the locally charged types of GBs differ. This is probably due to the orientation of boundary plane on either side of the GB. The GB with similarly oriented boundary plane shows typical bright contrast, while that with differently oriented planes gives bright or dark contrast (Leach, 2001, 2005).

4.10.6.4 EBIC Characterization of Devices

In addition to characterize extended defects in semiconductors, EBIC is also useful for the diagnosis of devices. For instance, it can determine the location of p–n junctions, measure the minority carrier diffusion length, detect the leakage sites, etc. Typical examples will be illustrated in the following.

4.10.6.4.1 p–n junctions

Figure 42 shows an EBIC study of a diamond p–n junction by Sekiguchi and Koizumi (2002). The dopants were B and P with concentrations of $(1–2) \times 10^{17}$ and $(7–8) \times 10^{18}\,\mathrm{cm}^{-3}$, respectively. The thicknesses of the B- and P-doped layer were ~2.0 and ~1.5 μm, respectively. The SE image in **Figure 42(a)** presents a cross-sectional view of the fabricated p–n junction. **Figures 42(b)** and **42(c)** show the EBIC images at 0 and reverse 40 V bias in pseudo-color overlaid with the SE image. It is evident that internal electric field exists at the boundary between B- and P-doped layers, which indicates that the p–n junction corresponds to this interface. On the other hand, no EBIC signal was detected at the interface between the P-doped layer and the metal electrode. These results suggest that a UV luminescence at ~235 nm (Koizumi *et al.*, 2001) of this type of LED originates in the p–n junction.

Line-scan EBIC profiles under various reverse bias, taken along the line in **Figure 42(b)**, are shown in **Figure 42(d)**. The *x*-axis represents the distance from the metal contact. The p–n junction is recognized by the change of slope on the right-hand side of the profile, marked with an arrow in **Figure 42(d)**. The EBIC signals were mostly detected from the B-doped region. Since the dopant concentration of P-doped layer is ~40 times higher than that of B-doped layer, the depletion region is mostly extended into the B-doped region. As a result, most of EBIC signals were observed in the B-doped layer. The small change of slope on the left-hand side of the profile is the interface between

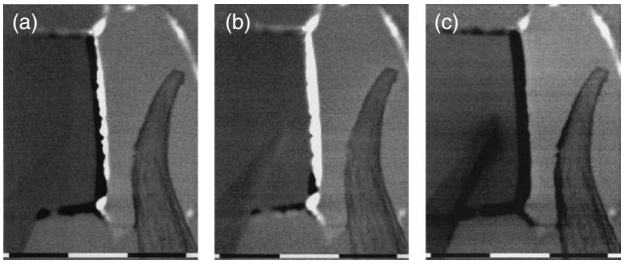

Figure 41 REBIC images of GBs in ZnO with (a) zero, (b) +40 mV, and (c) −40 mV bias applied (scale bars = 10 μm). From Leach C (2001) Crystal plane influence of the EBIC contrast in zinc oxide varistors. *Journal of the European Ceramic Society* 21: 2127–2130.

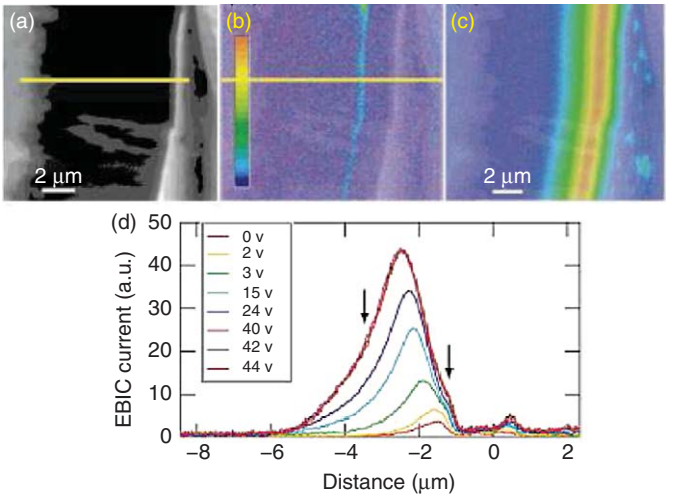

Figure 42 (a) SE image of cross-sectional diamond p–n junction, (b, c) EBIC images with 0 and 40 V reverse bias in pseudo-color overlaid with the SE image, (d) EBIC profiles across the line indicated in **Figure 42(b)** under various reverse bias. From Sekiguchi T and Koizumi S (2002) Characterization of a diamond p–n junction using electron-beam-induced current and cathodoluminescence. *Applied Physics Letters* 81: 1987–1989.

the B-doped layer and the substrate, denoted by the left arrow in **Figure 42(d)**. The EBIC profile in the substrate is gentler than that in B-doped layer, suggesting that the ionized acceptor concentration in the former is smaller than that in the latter. The EBIC current increases when the applied bias increases. This suggests that the impact ionization of electron occurs at the depletion region in the B-doped layer. Due to this effect, the EBIC maximum does not coincide with the p–n junction but falls in the B-doped layer.

Figure 43 presents an EBIC mapping of cross-sectional InGaN/GaN QW structure (Progl *et al.*, 2008). The multiple QWs (from 1 to 8) were clearly resolved between n and p layer. In addition, a *V* defect was observed inside the QW region. Such *V* defects are believed to be induced by the TDs during growth of multiple QWs (Chen *et al.*, 1998). To know the effect of this *V* defect, EBIC line scans from (a) to (d) were performed. EBIC signal suppression was observed when the line scans the defect center. The defect contrast, defined as the percent reduction in signal at the defect compared to the signal far from the defect, was measured to be 84% from the change in peak to trough spread between line scans outside (a) and the center (d) of the *V* defect. The peak current and hence p–n

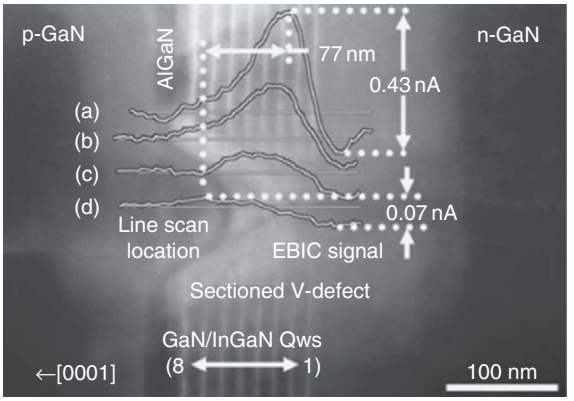

Figure 43 EBIC line profiles taken at different distances from the middle of a sectional *V* defect. From Progl CL, Parish CM, Vitarelli JP, and Russell PE (2008) Analysis of V defects in GaN-base light emitting diodes by scanning transmission electron microscopy and electron beam induced current. *Applied Physics Letters* 92: 242103.

junction was initially located in line scan (a) at 22 ± 2 nm from QW-1. When the line scan intersected more of the defect, the p–n junction was displaced 77 nm toward the p-GaN layer and the EBIC profile became broader. In the center of the defect, the resulting EBIC profile (d) barely indicates the presence of a p–n junction. Furthermore, the V defect disrupts the AlGaN confinement layer and the current drop observed in profile (a) is no longer present in profile (d). Thus, by using EBIC, the change of the p–n junction location was identified and the effect of device defects on the EBIC signal was directly observed.

4.10.6.4.2 Diffusion length

EBIC is a quick and powerful method to measure the minority carrier diffusion length (Chan *et al.*, 1995). If the incident e-beam is perpendicular to a planar Schottky barrier, fabricated on the material's top surface, the EBIC signal I decays with the beam-to-barrier distance d, according to the equation

$$I = Ad^{\alpha}\exp(-d/L) \tag{8}$$

where A is a constant, α a coefficient that depends on the surface recombination velocity ν_s, L the diffusion length. The coefficient α varies from $\alpha = -1/2$ for $\nu_s = 0$ to $\alpha = -3/2$ for infinite ν_s.

Figure 44 shows a temperature dependence of minority carrier diffusion length in n-GaN quasi-bulk epitaxial layer (Lin *et al.*, 2009). The coefficient $\alpha = -1/2$ was used here. At RT, the hole diffusion length L is about 1.3 μm. As the temperature increases, it gradually increases and reaches ~2.2 μm at 400 K. The activation energy was achieved by fitting the data using the following equation:

$$L = L_0 \exp\left(-\frac{\Delta E_a}{2kT}\right) \tag{9}$$

where L_0 is a scaling factor, ΔE_a the thermal activation energy, k the Boltzmann constant, and T the absolute temperature. An Arrhenius plot is shown in the inset of **Figure 44**. The activation energy ΔE_a, obtained from the slope, is about 100 meV.

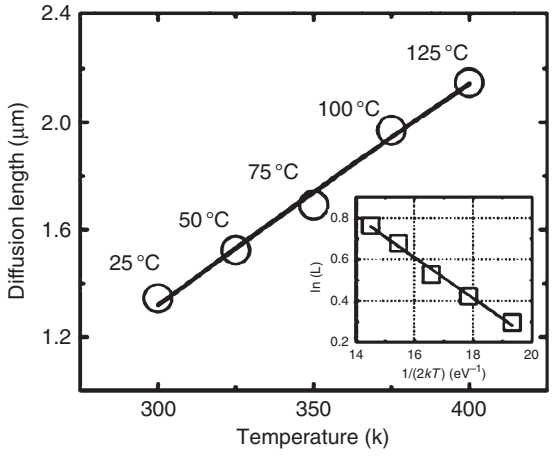

Figure 44 Temperature dependence of diffusion length obtained from EBIC measurement on GaN epitaxial layer. An Arrhenius plot of the same data is shown in the inset. From Lin Y, Flitsyian E, Chernyak L, *et al*. (2009) Optical and electron beam studies of carrier transport in quasibulk GaN. *Applied Physics Letters* 95: 092101.

4.10.6.4.3 Leakage detection in MOSFETs

High-k dielectrics are expected to replace SiO_2 in the future MOSFETs since they allow the use of the thinner gate electrode while preventing gate leakage. We report here on some current EBIC investigations of leakage sites in MOSFET with HfSiON dielectrics (Sekiguchi *et al.*, 2008; Chen *et al.*, 2006, 2008). **Figure 45** shows (a) the SE image of plan view and (b) the schematic of cross-sectional view of a p-channel MOSFET (Sekiguchi *et al.*, 2008). The thickness of each layer is illustrated in **Figure 45(b)**. For EBIC measurement, the gate electrode and the substrate were connected to the current amplifier with the bias circuit. The source and drain were isolated and not connected with any electrodes. EBIC observations were done by varying the e-beam irradiation condition and the bias voltage on gate electrode to check the leakage behavior.

Figure 46 shows the typical EBIC images of good and failed MOSFETs (Sekiguchi *et al.*, 2008). In the good MOSFET (**Figure 46(a)**), the gate region was seen as a uniform bright square under the reverse bias condition. When the gate bias changes, the brightness, namely the EBIC current, uniformly changes and no particular spots are observed in this gate area. On the other hand, the bright spots are found in the failed MOSFET as shown in **Figure 46(b)**. The number of bright spots and their distribution differ from FET to FET.

The bright spots may act as the leakage sites of HfSiON film. To confirm this fact, EBIC imaging of the gate area was performed by changing the e-beam energy. **Figure 47** shows EBIC images (Sekiguchi *et al.*, 2008) taken at the e-beam of 6, 7, and 9 kV. The electron range in each accelerating voltage roughly corresponds to 400, 500, and 800 nm (see **Figure 47(d)**). These images were recorded under the negative gate bias of $V_G = -1.0$ V. At 6 kV, the

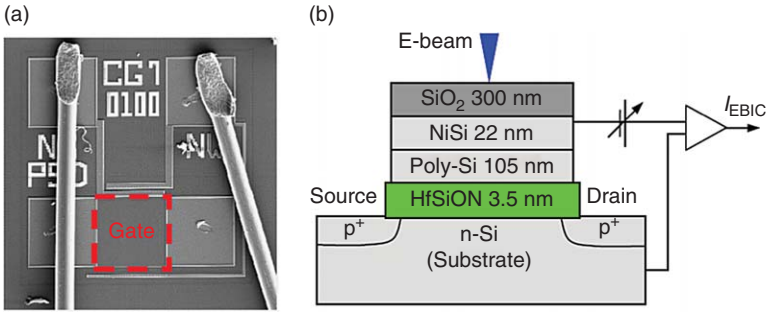

Figure 45 (a) Planar SE image and (b) schematic of cross-sectional structure of the high-*k* MOSFET. From Sekiguchi T, Chen J, Takase M, *et al*. (2008) Observation of leakage sites in high-*k* gate dielectrics in MOSFET devices by electron-beam-induced current technique. *Solid State Phenomena* 131–133: 449–454.

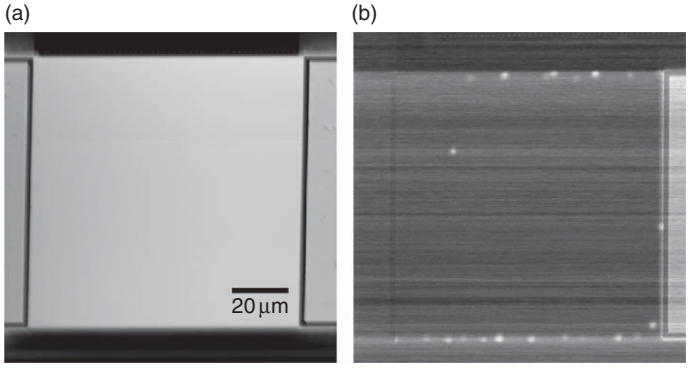

Figure 46 EBIC images of (a) good and (b) failed high-*k* MOSFETs. From Sekiguchi T, Chen J, Takase M, *et al*. (2008) Observation of leakage sites in high-*k* gate dielectrics in MOSFET devices by electron-beam-induced current technique. *Solid State Phenomena* 131–133: 449–454.

EBIC current is very weak so that EBIC image becomes rather noisy. However, no bright spots were observed in the gate area. At 7 kV, on the other hand, the bright spots appeared at the peripheral region of the gate dielectric. The bright spots became much brighter in the EBIC image taken at 9 kV. The number of bright spots did not change under different e-beam energies. It indicates that the bright spots can be observed when the carriers generated in the substrate region may flow through the HfSiON film, thus confirming that the bright spots are leakage sites of HfSiON film.

Figure 48 presents bias dependence of a failed MOSFET taken with an e-beam of 10 kV (Sekiguchi *et al*., 2008). At zero bias, two weak dark halos were observed at the central region of the gate. The dark halos (denoted as DH1 and DH2) are probably defects in the Si substrate. When the reverse bias was −0.6 V, bright spots were seen, most of them localized at the peripheral region, but some also in the inner region like BS1 as denoted in **Figure 48(b)**. When the reverse bias increased up to −1.4 V, both bright spots and dark halos gradually disappear and the EBIC image at the gate region becomes uniformly bright. This is due to the increase of the background current, which may mask the leakage at the bright spot region. This means that a suitable bias is necessary in order to observe the leakage sites in MOSFETs.

4.10.7 Future Advancement of CL and EBIC

The literature and the examples reviewed in this chapter indicate that the SEM-CL technique is approaching the ultimate analytical and lateral resolution limit. On the contrary, new perspectives have recently been addressed by the TEM-CL technique.

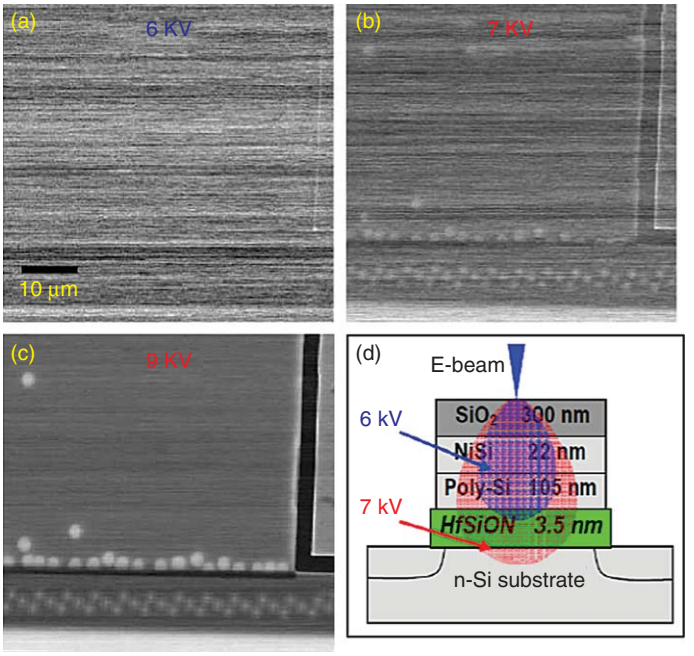

Figure 47 EBIC images of leakage sites in a failed MOSFET taken under different e-beam energies of (a) 6 kV, (b) 7 kV, and (c) 9 kV; (d) an illustration of the electron range in the high-*k* stack. From Sekiguchi T, Chen J, Takase M, *et al*. (2008) Observation of leakage sites in high-*k* gate dielectrics in MOSFET devices by electron-beam-induced current technique. *Solid State Phenomena* 131–133: 449–454.

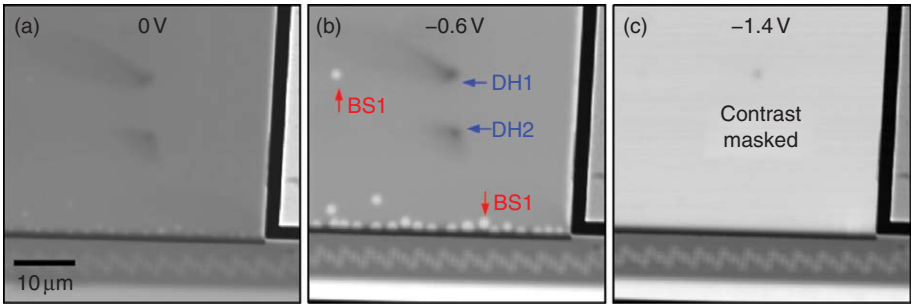

Figure 48 EBIC images of a failed MOSFET taken at different bias condition. From Sekiguchi T, Chen J, Takase M, *et al*. (2008) Observation of leakage sites in high-*k* gate dielectrics in MOSFET devices by electron-beam-induced current technique. *Solid State Phenomena* 131–133: 449–454.

The TEM-CL approach is quite intriguing, in particular for a peculiarity not achievable by any SEM, that is, the possibility of studying optical, structural, and chemical properties of semiconductor nanostructures in a single experiment down to the atomic scale. A commercial analytical field emission TEM can operate in parallel beam or convergent beam illumination modes. In the last case the convergent beam is focused onto the sample and is scanned across it and different signals are recorded as a function of probe position. This operation mode is called scanning transmission electron microscopy (STEM). Typical STEMs, without aberration correctors, allow chemical imaging, the so-called Z-contrast, roughly proportional to the atomic number squared, with a chemical sensitivity $\Delta Z \sim 2$ and a lateral resolution $\Phi < 0.14$ nm, energy filtered imaging, electron energy loss spectroscopy, X-ray microanalysis, and, obviously, atomic resolution imaging with $\Phi < 0.2$ nm when operating in the conventional TEM mode.

Seminal work in the field of (S)TEM-CL has been done by Steeds (1989) and, more recently, by

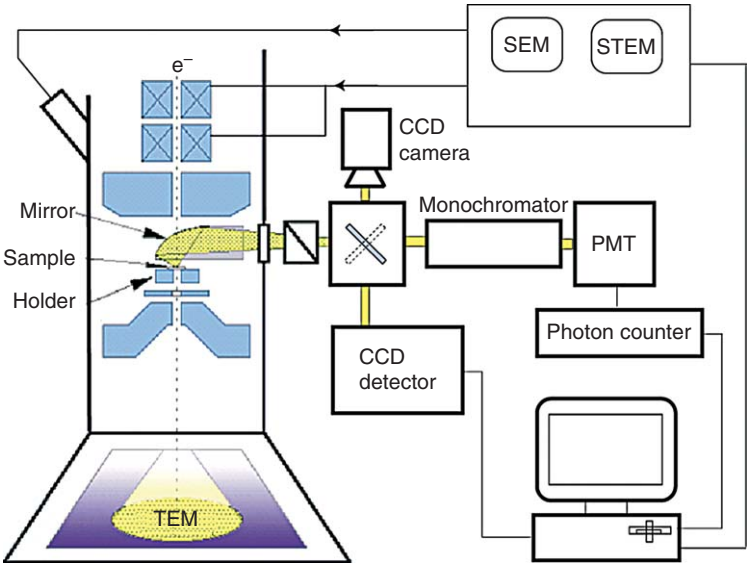

Figure 49 Sketch of a typical CL setup attached to a conventional (S)TEM. Courtesy of N. Yamamoto.

Yamamoto *et al.* (2006), concerning in particular the application of polarized TEM-CL to the characterization of semiconductor nanostructures.

A typical experimental set up is reported in Figure 49.

As for EBIC, in conjunction with the imaging capabilities of an SEM, EBIC has been demonstrated to be a powerful technique for nondestructive study of extended defects in semiconductor materials and failures in semiconductor devices. As the material or device size go down to the nanoscale, conventional EBIC imaging may be hindered owing to its micrometric resolution.

Figure 50 illustrates a development of EBIC, namely nano-EBIC, for characterizing nanostructured semiconductors (Smaali *et al.*, 2008). This EBIC system is connected with the conductive probe of an AFM combined with an SEM. By using the AFM tip for probing, a resolution of the order of 20 nm has been achieved. Some examples about this technique can be found in recent papers by Smaali *et al.* (2006, 2008) and Troyon *et al.* (2007). The nano-EBIC may provide strong potential to study increasingly small semiconductor devices.

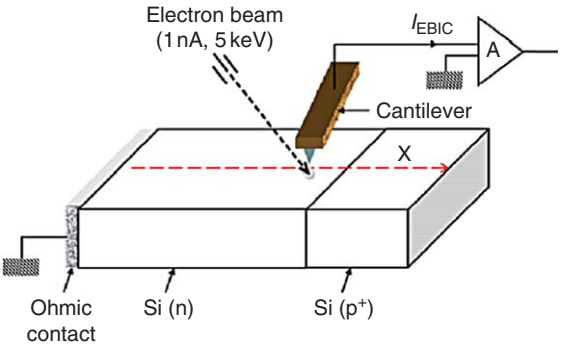

Figure 50 Schematic of a p–n junction studied in cross section by nano-EBIC. From Smaali K, Fauré J, El Hdiy A, and Troyon M (2008) High-resolution scanning near-field EBIC microscopy: Application to the characterization of a shallow ion implanted p^+–n silicon junction. *Ultramicroscopy* 108: 605–612.

4.10.8 Conclusions

In this chapter the potentiality and flexibility of both SEM-CL and SEM-EBIC in the optical and electro-optical assessment of semiconductor nanostructures and devices have been briefly described. Some selected examples among the most recent and advanced experiments from the literature have been reviewed. These examples demonstrate how important the contribution of CL and EBIC has been for the development of materials and devices and how many impulses to the applied research they provided during the last three decades.

The key role they have already achieved together with the development of new generations of SEMs and (S)TEMs will make these techniques once again an essential tool for the assessment of modern semiconductor nanostructures. (See Chapters 2.05, 3.05, 3.13 and 6.03).

References

Abbe E (1873) Beiträge zur Theorie des Mikroskops und der Mikroskopischen wahrnehmung. *Archiv für Mikroskopische Anatomie* 9(1): 413–418.

Armani N, Rossi F, Ferrari C, *et al.* (2004) Polarization field effects on the recombination dynamics in low-In-content InGaN multi-quantum wells. *Superlattices and Microstructures* 36/4-6: 615–624.

Balk LJ (1988) Scanning electron acoustic microscopy. *Advances in Electronics and Electron Physics* 71: 1–73.

Balk LJ, Heiderhoff R, Phang JCH, and Thomas CH (2007) Characterization of electronic materials and devices by scanning near field microscopy. *Applied Physics A* 87: 443–449.

Balk LJ and Kultsher N (1987) Application of the SEAM to the characterization of semiconducting materials and devices. *Institute of Physics Conference Series* 87: 675–684.

Bimberg D, Munzel H, Steckenborn A, and Christen J (1985) Kinetics of relaxation and recombination of nonequilibrium carriers in GaAs – carrier capture by impurities. *Physical Review B* 31(12): 7788–7799.

Brandis E and Rosencwaig A (1980) Thermal-wave microscopy with electron beams. *Applied Physics Letters* 37(1): 98–100.

Breitenstein O (1989) Scanning DLTS. *Review de Physique Appliquee* 24(6): 101–110.

Breitenstein O and Heydenreich J (1985) Scanning deep level transient spectroscopy. *Scanning* 7: 273–289.

Breton BC (2009) *The Early History and Development of the Scanning Electron Microscope*. http://www2.eng.cam.ac.uk/~bcb/history.html (accessed March 2010)).

Brillson LJ, Mosbacker HL, Hetzer MJ, *et al.* (2007) Dominant effect of near-interface native point defects on ZnO Schottky barriers. *Applied Physics Letters* 90(10): 102116.

Cargill GS (1980) Ultrasonic imaging in scanning electron microscopy. *Nature* 286(5774): 691–693.

Castaldini A, Cavallini A, Polenta L, Dıaz-Guerra C, and Piqueras J (2002) Electrical and optical characterization of GaN HVPE layers related to extended defects. *Journal of Physics: Condensed Matter* 14: 13095–13104.

Chan DSH, Ong VKS, and Phang JCH (1995) A direct method for the extraction of diffusion length and surface recombination velocity from an EBIC line scan planar junction configuration. *IEEE Transactions on Electron Devices* 42: 963–968.

Chen B, Chen J, Sekiguchi T, *et al.* (2008a) Electron-beam-induced current study of electrical activity of dislocations in 4H-SiC homoepitaxial film. *Journal of Materials Science: Materials in Electronics* 19: 5219–5223.

Chen B, Chen J, Sekiguchi T, *et al.* (2008b) Electron-beam-induced current study of stacking faults and partial dislocations in 4H-SiC Schottky diode. *Applied Physics Letters* 93: 033514.

Chen B, Sekiguchi T, Ohyanagi T, Matsuhata H, Kinoshita A, and Okumura H (2009) Electron-beam-induced current and cathodoluminescence study of dislocation arrays in 4H-SiC homoepitaxial layers. *Journal of Applied Physics* 106: 074502.

Chen J, Sekiguchi T, Fukata N, *et al.* (2006) Observation of leakage sites in hafnium silicon oxynitride gate dielectric of a metal-oxide-semiconductor field-effect transistor devices by electron-beam-induced current. *Applied Physics Letters* 89: 222104.

Chen J, Sekiguchi T, Fukata N, *et al.* (2008) Comparison of leakage behaviors in p- and n-type metal-oxide-semiconductor capacitors with hafnium silicon oxynitride gate dielectric by electron-beam-induced current. *Applied Physics Letters* 92: 262103.

Chen J, Sekiguchi T, and Yang D (2007) Electron-beam-induced current study of grain boundaries in multicrystalline Si. *Physica Status Solidi (c)* 4: 2908–2917.

Chen J, Sekiguchi T, Xie R, *et al.* (2005a) Electron-beam-induced current study of small-angle grain boundaries in multicrystalline silicon. *Scripta Materialia* 52: 1211–1215.

Chen J, Sekiguchi T, Yang D, Yin F, Kido K, and Tsurekawa S (2004) Electron-beam-induced current study of grain boundaries in multicrystalline silicon. *Journal of Applied Physics* 96: 5490–5495.

Chen J, Yang D, Xi Z, and Sekiguchi T (2005b) Recombination activity of $\Sigma 3$ boundaries in boron-doped multicrystalline silicon: influence of iron contamination. *Journal of Applied Physics* 97: 033701.

Chen Y, Takeuchi T, Amano H, *et al.* (1998) Pit formation in GaInN quantum wells. *Applied Physics Letters* 72: 710–712.

Corfdir P, Ristić J, Lefebvre P, *et al.* (2009) Low-temperature time-resolved cathodoluminescence study of exciton dynamics involving basal stacking faults in a-plane GaN. *Applied Physics Letters* 94(20): 201115.

Cramer RM, Ebinghaus V, Heiderhoff R, and Balk LJ (1998) Near-field cathodoluminescence (NF-CL) investigations on semiconducting materials. *Solid State Phenomena* 63–64: 257–260.

De Wolf P, Stephenson R, Trenkler T, Clarysse T, and Hantschel T (2000) Status and Review of Two-Dimensional Carrier and Dopant Profiling Using Scanning Probe Microscopy. *Journal of Vacuum Science and Technology B* 18(1): 361–368.

Dean PJ (1982) Photoluminescence as a diagnostic of semiconductors. *Progress in Crystal Growth and Characterization of Materials* 5: 89–174.

Della Sala F, Di Carlo A, Lugli P, Bernardini F, Fiorentini V, Scholz R, Jancu JM (1999) Free-carrier screening of polarization fields in wurtzite GaN/InGaN laser structures. *Applied Physics Letters* 74: 2002–2004.

Dierre B, Yuan XL, Inoue K, Hirosaki N, Xie R-J, and Sekiguchi T (2009) Role of Si in the luminescence of AlN:Eu,Si phosphors. *Journal of the American Ceramic Society* 92(6): 1272–1275.

Donolato C (1982) On the analysis of diffusion length measurements by SEM. *Solid-State Electronics* 25: 1077–1081.

El-Gomati MM, Wells TCR, Müllerová I, Frank L, and Jayakody H (2004) Why is it that differently doped regions in semiconductors are visible in low voltage SEM? *IEEE Transactionson Electron Devices* 51(2): 288–292.

Felici M, Polimeri A, Salviati G, *et al.* (2006) In-plane bandgap engineering by modulated hydrogenation of dilute nitride semiconductors. *Advanced Materials* 18(15): 1993–1997.

Giovane LM, Luan H-C, Agarwal AM, and Kimerling LC (2001) Correlation between leakage current density and threading dislocation density in SiGe p–i–n diodes grown on relaxed graded buffer layers. *Applied Physics Letters* 78: 541–543.

Gonzalez JC, Bunker KL, and Russell PE (2001) Minority-carrier diffusion length in a GaN-based light emitting diode. *Applied Physics Letters* 79: 1567–1569.

Grillo V, Armani N, Rossi F, Salviati G, and Yamamoto N (2003) Al.L.E.S.: A random walk simulation approach to cathodoluminescence processes in semiconductors. *Institute of Physics Conference Series* 180: 565–569.

Grillo V, Rossi F, Armani N, Yamamoto N, and Salviati G (2007) Simulation of the cathodoluminescence processes in semiconductors. In: Salviati G, Sekiguchi T, Heun S, and Gustafsson A (eds.) *Beam Injection Based Nanocharacterization of Advanced Material*, ch. 4, pp. 87–137. Kerala, India: Research Signpost.

Gustafsson A, Pistol ME, Montelius L, and Samuelson L (1998) Local probe techniques for luminescence studies of low-dimensional semiconductor structures. *Journal of Applied Physics* 84(4): 1715–1775.

Ha S, Benamara M, Skowronski M, and Lendenmann H (2003) Core structure and properties of partial dislocations in silicon carbide p–i–n diodes. *Applied Physics Letters* 83: 4957–4959.

Hara H, Hikita K, Lai CG, and Sakurai T (2004) Combustion synthesis of aluminum nitride phosphors. In: *Proceedings of the 12th International Workshop on Inorganic and Organic Electroluminescence & 2004 International Conference on the Science and Technology of Emissive Displays and Lighting,* pp. 24–27.

Hidalgo P, Liberti E, Rodriguez-Lazcano Y, Mendez B, and Piqueras J (2009) GeO_2 nanowires doped with optically active ions. *Journal of Physics and Chemistry C* 113: 17200–17205.

Hirosaki N, Xie R-J, Inoue K, Sekiguchi T, Dierre B, and Tamura K (2007) Blue-emitting AlN:Eu^{2+} nitride phosphor for field emission displays. *Applied Physics Letters* 91: 061101.

Holt DB, Raza B, and Wojcik A (1996) EBIC studies of grain boundaries. *Materials Science and Engineering B* 42: 14–23.

Ismail K, LeGoues FK, Saenger KL, *et al.* (1994) Identification of a mobility-limiting scattering mechanism in modulation doped Si/SiGe heterostructures. *Physical Review Letters* 73: 3447–3450.

Iwata H, Lindefelt U, Öberg S, and Briddon PR (2003) Cubic polytype inclusions in 4H-SiC. *Journal of Applied Physics* 93: 1577–1585.

Jahn U, Dhar S, Brandt O, Grahn HT, Ploog KH, and Watson IM (2003) Exciton localization and quantum efficiency – a comparative cathodoluminescence study of (In,Ga)N/GaN and GaN/(Al,Ga)N quantum wells. *Journal of Applied Physics* 93(2): 1048–1053.

Kanaya K and Okayama S (1972) Penetration and energy-loss theory of electrons in solid targets. *Journal of Physics D: Applied Physics* 5: 43–58.

Khatsevich S, Rich DH, Keller S, and DenBaars SP (2007) Cathodoluminescence study of carrier relaxation, transfer, collection, and filling in coupled $In_xGa_{1-x}N$/GaN multiple and single quantum wells. *Physical Review B* 75(3): 035324.

Kittler M, Seifert W, and Knobloch K (2003) Influence of contamination on the electrical activity of crystal defects in Si. *Microelectronic Engineering* 66: 281–288.

Kittler M, Ulhaq-Bouillet C, and Higgs V (1995) Influence of copper contamination on recombination activity of misfit dislocations in SiGe/Si epilayers: Temperature dependence of activity as a marker characterizing the contamination level. *Journal of Applied Physics* 78: 4573–4583.

Knobloch K, Kittler M, and Seifert W (2003) Influence of contamination on the dislocation-related deep level C1 line observed in deep-level-transient spectroscopy of n-type silicon: A comparison with the technique of electron-beam-induced current. *Journal of Applied Physics* 93: 1069–1074.

Knobloch K, Perlin P, Krueger J, Weber ER, and Kisielowski C (1998) Effect of internal absorption on cathodoluminescence from GaN. *MRS Internet Journal on Nitride Semiconductors Research* 3(4): 1–4.

Kohan AF, Ceder G, Morgan D, and Van de Walle CG (2000) First-principles study of native point defects in ZnO. *Physical Review B* 61(22): 15019–15027.

Koizumi S, Watanabe K, Hasegawa F, and Kanda H (2001) Ultraviolet emission from a diamond p–n junction. *Science* 292: 1899–1901.

Kusanagi S, Sekiguchi T, Shen B, and Sumino K (1995) Extended defects and gettering of metallic impurities in Si. *Materials Science and Technology* 11: 685–690.

Lazzarini L, Salviati G, Fabbri F, *et al.* (2009) Unpredicted nucleation of extended zinc blende phases in wurtzite ZnO nanotetrapod arms. *ACS Nano* 9: doi:10.1021/nn900558q.

Leach C (2001) Crystal plane influence of the EBIC contrast in zinc oxide varistors. *Journal of the European Ceramic Society* 21: 2127–2130.

Leach C (2005) Grain boundary structures in zinc oxide varistors. *Acta Materialia* 53: 237–245.

Leamy HJ (1982) Charge collection scanning electron microscopy. *Journal of Applied Physics* 53: R51–R80.

Li S, Jiang F, Yin Q, and Jin Y (1996) Scanning electron acoustic microscopy of semiconductor materials. *Solid State Communications* 99(11): 853–857.

Lin JC and Everhart TE (1979) Study on voltage contrast in SEM. *Journal of Vacuum Science and Technology* 16(6): 1856–1860.

Lin Y, Flitsyian E, Chernyak L, *et al.* (2009) Optical and electron beam studies of carrier transport in quasibulk GaN. *Applied Physics Letters* 95: 092101.

Merano M, Sonderegger S, Crottini A, *et al.* (2005) Probing carrier dynamics in nanostructures by picosecond cathodoluminescence. *Nature* 438(7076): 479–482.

Morandi V, Merli PG, and Ferroni M (2006) Dopant region imaging in scanning electron microscopy. *Journal of Applied Physics* 99(4): 043512.

Mosbacker HL, Zgrabik C, Hetzer MJ, *et al.* (2007) Thermally driven defect formation and blocking layers at metal–ZnO interfaces. *Applied Physics Letters* 91(7): 072102.

Myhajlenko S, Ke WK, and Hamilton B (1983) Cathodoluminescence assessment of electron beam recrystallized silicon. *Journal of Applied Physics* 54(2): 862–867.

Pankove JI (1971) Radiative transistions. In: *Optical Processes in Semiconductors*, ch. 6, pp. 107–159. Englewood Cliffs, NJ: Prentice Hall.

Pavesi L and Guzzi M (1994) Photoluminescence of $Al_xGa_{1-x}As$ alloys. *Journal of Applied Physics* 75(10): 4779–4842.

Pavesi M, Manfredi M, Salviati G, *et al.* (2004) Optical evidence of an electrothermal degradation of InGaN-based light-emitting diodes during electrical stress. *Applied Physics Letters* 84: 3403–3405.

Perovic DD, Castell MR, Howie A, Lavoie C, Tiedje T, and Cole JSW (1995) Field-emission SEM imaging of compositional and doping layer semiconductor superlattice. *Ultramicroscopy* 58(1): 104–113.

Petroff PM and Lang DV (1977) A new spectroscopic technique for imaging the spatial distribution of nonradiative defects in a scanning transmission electron microscope. *Applied Physics Letters* 31: 60–62.

Phillips MR, Telg H, Kucheyev SO, Gelhausen O, and Toth M (2003) Cathodoluminescence efficiency dependence on excitation density in n-type GaN. *Microscopy and Microanalysis* 9: 144–151.

Pirouz P, Demenet JL, and Hong MH (2001) On transition temperatures in the plasticity and fracture of semiconductors. *Philosophical Magazine A* 81: 1207–1227.

Progl CL, Parish CM, Vitarelli JP, and Russell PE (2008) Analysis of V defects in GaN-base light emitting diodes by scanning transmission electron microscopy and electron beam induced current. *Applied Physics Letters* 92: 242103.

Reimer L (1998) *Scanning Electron Microscopy: Physics of Image Formation and Microanalysis*. Berlin, Heidelberg: Springer.

Rosencwaig A (1982) Thermal wave imaging. *Science* 218(4569): 223–228.

Rosencwaig A and Gersho A (1976) Theory of photoacoustic effects with solids. *Journal of Applied Physics* 47(1): 64–69.

Rossi F (2004), Interplay between structural and optical properties in semiconducting N-based heterostructures for optoelectronic applications, PhD Thesis, University of Parma.

Russell GJ, Robertson MJ, Vincent B, and Woods J (1980) An electron-beam induced current study of grain-boundaries in zinc selenide. *Journal of Materials Science* 15: 939–944.

Russell JD, Halls DC, and Leach C (1996) Grain boundary SEM conductive mode contrast effects in additive free zinc oxide ceramics. *Acta Materialia* 44: 2431–2436.

Salviati G, Albrecht M, Zanotti-Fregonara C, *et al.* (1999) The influence of crystal defects on optical transitions in GaN. *Physica Status Solidi (a)* 171: 325–339.

Salviati G, Lazzarini L, Zha MZ, Grillo V, and Carlino E (2005) Cathodoluminescence spectroscopy of single SnO_2

nanowires and nanobelts. *Physica Status Solidi (a)* 202(15): 2963–2970.
Salviati G, Rossi F, Armani N, Grillo V, and Lazzarini L (2008) Power dependent cathodoluminescence in III-nitrides heterostructures: From internal field screening to controlled band gap modulation. In: Lamberti C (ed.) *Characterization of Semiconductor Heterostructures and Nanostructures*, ch. 7, pp. 209–248. Amsterdam: Elsevier.
Salviati G, Rossi F, Armani N, *et al.* (2004) Optical and structural characterization of self-organized stacked GaN/AlN quantum dots. *Journal of Physics: Condensed Matter* 16(2): S115–S126.
Salviati G, Rossi F, Armani N, *et al.* (2001) Depth resolved cathodoluminescence study of optical transitions in MOVPE hexagonal GaN. *Institute of Physics Conference Series* 169: 251–254.
Samuelson L and Gustafsson A (1995) Imaging and spectroscopic studies of individual impurities in quantum structures. *Physical Review Letters* 74(12): 2395–2398.
Schäfer J, Young AP, Brillson LJ, Niimi H, and Lucovsky G (1998) Depth-dependent spectroscopic defect characterization in the interface between plasma-deposited SiO_2 and silicon. *Applied Physics Letters* 73: 791–793.
Sekiguchi T, Chen J, Takase M, *et al.* (2008) Observation of leakage sites in high-*k* gate dielectrics in MOSFET devices by electron-beam-induced current technique. *Solid State Phenomena* 131–133: 449–454.
Sekiguchi T, Hu J, and Bando Y (2004) Cathodoluminescence study of one-dimensional free-standing widegap-semiconductor nanostructures: GaN nanotubes, Si_3N_4 nanobelts and ZnS/Si nanowires. *Journal of Electron Microscopy* 53: 203–208.
Sekiguchi T and Koizumi S (2002) Characterization of a diamond p–n junction using electron-beam-induced current and cathodoluminescence. *Applied Physics Letters* 81: 1987–1989.
Sekiguchi T and Sumino K (1995) Quantitative electron-beam tester for defects in semiconductors (CL/EBIC/SDLTS system). *Review of Scientific Instruments* 66: 4277–4282.
Shah J (1996) *Ultrafast Spectroscopy of Semiconductors and Semiconductor Nanostructures*. Berlin: Springer.
Shockley W and Read WT (1952) Statistics of the recombinations of holes and electrons. *Physical Review* 87: 835–842.
Smaali K, Fauré J, El Hdiy A, and Troyon M (2008) High-resolution scanning near-field EBIC microscopy: Application to the characterization of a shallow ion implanted p^+–n silicon junction. *Ultramicroscopy* 108: 605–612.
Smaali K, Troyon M, El Hdiy A, Molinari M, Saint-Girons G, and Patriarche G (2006) Imaging the electric properties of InAs/InP(001) quantum dots capped with a thin InP layer by conductive atomic force microscopy: Evidence of memory effect. *Applied Physics Letters* 89: 112115.
Steeds J (1989) Performance and applications of a STEM-cathodoluminescence system. *Journal de Physique Colloques* 50: C6-65–C6-72.
Synge EH (1928) A suggested method for extending microscopic resolution into the ultra-microscopic region. *Philosophical Magazine Series* 6(35): 356–362.
Synge EH (1932) An application of piezo-electricity to microscopy. *Philosophical Magazine Series* 13(83): 297–300.
Takahashi J, Kanaya M, and Fujiwara Y (1994) Sublimation growth of SiC single-crystalline ingots on faces perpendicular to the (0001) basal-plane. *Journal of Crystal Growth* 135: 61–70.
Thomas C, Heiderhoff R, and Balk LJ (2007) 200 femtometer sensitivity for near-field analysis of surface acoustic waves in a scanning electron/scanning probe hybrid system. *Applied Physics Letters* 90(14): 144106.
Thong JTL, Garth SCJ, Breton BC, and Nixon WC (1987) Ultra high speed electron beam testing system. *Microelectronic Engineering* 6(1–4): 683–688.
Troyon M and Smaali K (2007) Scanning near-field electron beam induced current microscopy: Application to III-V heterostructures and quantum dots. *Applied Physics Letters* 90: 212110.
Troyon M, Pastrè D, Jouart JP, and Beaudoin JL (1998) Scanning near field cathodoluminescence microscopy. *Ultramicroscopy* 75(1): 15–21.
Urchulutegui M and Piqueras J (1991) Temperature dependence of scanning electron acoustic microscopy signal in MgO and SiC. *Journal of Applied Physics* 69(6): 3589–3593.
Varga I, Pogany L, Hargitai C, and Bakonyi I (2006) Extracting domain wall patterns from SEM magnetic contrast images. *Journal of Magnetism and Magnetic Materials* 302(2): 405–412.
Vine J and Einstein PA (1964) The heating effect of an electron beam impinging on a solid surface, allowing for penetration. *Proceedings of the IEEE* 111: 921–930.
Xie R-J and Hirosaki N (2007) Silicon-based oxynitride and nitride phosphors for white LEDs – a review. *Science and Technology of Advanced Materials* 8: 588–600.
Yacobi BG and Holt DB (1990) *Cathodoluminescence Microscopy of Inorganic Solids*. New York: Plenum.
Yakimov EB, Vergeles PS, Polyakov AY, *et al.* (2007) Spatial variations of doping and lifetime in epitaxial laterally overgrown GaN. *Applied Physics Letters* 90: 152114.
Yamamoto N, Bhunia S, and Watanabe Y (2006) Polarized cathodoluminescence study of InP nanowires by transmission electron microscopy. *Applied Physics Letters* 88(15): 153106.
Yuan XL, Sekiguchi T, Ri SG, and Ito S (2004) Detection of misfit dislocations at interface of strained $Si/Si_{0.8}Ge_{0.2}$ by electron-beam-induced current technique. *Applied Physics Letters* 84: 3316–3318.
Zaldivar MH, Fernández P, and Piqueras J (2001) Study of growth hillocks in GaN:Si films by electron beam induced current imaging. *Journal of Applied Physics* 90: 1058–1060.
Zoroddu A, Bernardini F, Ruggerone P, Fiorentini V (2001) First-principles prediction of structure, energetics, formation enthalpy, elastic constants, polarization, and piezoelectric constants of AlN, GaN, and InN: Comparison of local and gradient-corrected density-functional theory. *Physical Review B* 64: 045208.

Further Reading

Chen J and Sekiguchi T (2007) Carrier recombination activity and structural properties of small-angle grain boundaries in multicrystalline Si. *Japanese Journal of Applied Physics* 46: 6489–6497.
Herrera Zaldivar M, Fernández P, and Piqueras J (2001) Study of growth hillocks in GaN:Si films by electron beam induced current imaging. *Journal of Applied Physics* 90: 1058–1060.
Smaali K and Troyon M (2008) Application of nano-EBIC to the characterization of GaAs and InP homojunctions. *Nanotechnology* 19: 155706.
Troyon M and Smaali K (2007) Scanning near-field electron beam induced current microscopy: Application to III–V heterostructures and quantum dots. *Applied Physics Letters* 90: 212110.

Relevant Websites

http://apps.isiknowledge.com
http://www.gatan.com/products/sem_products/products/digiscan.php
http://www.trnres.com/